Kinetic Analysis of Electrochemical Oxygen Reduction and Development of Ag-alloy Catalysts for Low Temperature Fuel Cells

by

Adam Paul Holewinski

A dissertation submitted in partial fulfillment
of the requirements for the degree of
Doctor of Philosophy
(Chemical Engineering)
in The University of Michigan
2013

Doctoral Committee:

Associate Professor Suljo Linic, Chair
Professor Mark Barteau
Professor John Halloran
Assistant Professor Charles Monroe
Professor Phillip E. Savage

“What I cannot create, I do not understand”

-Richard Feynman

For Julie…

Acknowledgements

This dissertation would not be possible without the help of many people along the way. I would like to first thank my advisor, Prof. Suljo Linic, for his guidance throughout my studies. His willingness to always re-evaluate assumptions has generated countless discussions that have provided insight and perspective on how to solve problems, and his emphasis on quality has helped me to propel my research to levels I never thought possible. I also thank my thesis committee, Professors Phillip E. Savage, Mark Barteau, Charles Monroe, and John Halloran for comments provided during preliminary meetings and on this document, as well as discussions throughout the past several years.

Thanks as well to the entire Linic Research Group, members both past and present: Eranda Nikolla, Siris Laursen, Neil Schweitzer, Phillip Christopher, Hongliang Xin, David Ingram, Matthew Morabito, Marimuthu Andiappan, Michelle Przybylek, Thomas Yeh, Paul Hernley, Timothy Van Cleve, Brittany Lancaster, Anh Ta, Calvin Boerigter, and Robert Campana. Numerous conversations as well as assistance tending to experiments when I could not be around were exceedingly helpful. I would like to individually acknowledge Hong for involving me in collaborative work and generally being a superb resource for theory based questions, Matt for fixing our computer cluster many times, Tim for brainstorming

on electrochemical experiments, and Phil for making long hours in the lab unique experiences. Additionally, I have had the help of a number of undergraduate assistants: Kevin Kasunic, Caitlin Cramer, Andrea Revels, and Kannah Salazar. These individuals have helped to run many more experiments than I could possible do alone and they have tolerated my poor planning and worked well beyond scheduled hours to get the job done.

Thank you to Michelle Maloney for patience and love. And thank you to all my friends in the department, in Ann Arbor, and throughout my whole life. There are far too many names to write, but you have all helped me immensely in both times of celebration and times of need.

Finally, thank you to my family. My father Paul, brother Alex, and mother Julie, who passed away during my Ph.D. studies. Dad, I thank you for inspiring me with an interest in science from a very young age, as well as love and support throughout the years. Mom, you are a continual source of inspiration and I cannot begin to express my gratitude for the years of love, support, and sacrifice that have allowed me to reach this point.

Table of Contents

List of Figures

List of Tables

Abstract

In this dissertation we have applied insights from quantum chemical calculations and heterogeneous kinetic analysis to interpret macroscopic reactivity trends in electrochemical systems and to design optimal electro-catalysts. Specifically we have explored the mechanism of the electrochemical oxygen reduction reaction (ORR), a reaction with great importance for use in fuel cells, on the surfaces of Pt (a near-optimal catalyst) and Ag electrodes. We have identified design criteria for improving the reaction rate in each case and developed cost-effective Ag-based alloy materials with activity approaching that of more costly Pt catalysts.

We have first demonstrated, using microkinetic modeling and density functional theory calculations, that deviations from ideal electrode kinetics (a linear potential vs. log current relationship) are inherent to the ORR and any multi-step heterogeneous electro-catalytic reaction. Deviations can be attributed to simultaneous changes in the rate of the rate-limiting elementary step and the number of available active sites on the electrode surface as potential is shifted. We show that the ORR kinetic variations on Pt electrodes are well-reproduced by a simple description of changes in OH and H_2O surface intermediate coverages, and that weaker binding materials will exhibit higher rates due to higher availability of

active sites. In contrast, on Ag a very weak relation is found between adsorbate coverage and changes in the apparent rate law. This points to a strong role of under-coordinated active sites, which can become poisoned at low potentials while the majority of the surface is still clean. Moving in the direction of stronger binding on Ag should lead to higher ORR activity by increasing turnover rates on the more predominant surface facets.

Using the mechanistic insights mentioned, we illustrate the design of relatively inexpensive Ag-Co surface alloy nanoparticle electro-catalysts for oxygen reduction, with equivalent area-specific activity to commercial Pt-nanoparticles at realistic fuel cell operating conditions. The Ag-Co materials were identified with quantum chemical calculations and synthesized with a novel bimetallic precursor decomposition technique that generates a surface alloy, despite the bulk immiscibility of the constituent materials. Characterization studies show that the origin of the activity improvement comes from a ligand effect, in which Co perturbs the Ag surface sites and improves their inherent activity. We also explore the use of bimetallic precursor decomposition for production of Ag-Ni and Ag-Fe alloys but find that the products exhibit substantial segregation and have ORR activities similar to monometallic Ag.

Chapter 1: Introduction

A brief overview of the field of heterogeneous catalysis and relevant challenges pertaining to the issues of energy consumption and environmental impact are given. Extra focus is given to the role of electro-catalytic technologies, and in particular opportunities for efficient energy conversion with hydrogen fuel cells. The current state of the art in fuel cell catalyst technology is surveyed, along with challenges to continued advances. Key objectives in the design of catalytic materials are then discussed in general, along with recent advances toward closing the gap between experiment and theory, with emphasis on the ultimate goal of using predictive theories to precisely target and rationally design new catalysts. The chapter concludes with a brief outline of the structure and scope of the thesis.

1.1 Heterogeneous Catalysis, Energy, and the Environment

Broadly speaking, a catalyst can be defined as any substance that increases the rate of a chemical reaction without being consumed. Heterogeneous catalysts, which exist in a distinct phase from the reacting material (most often a solid catalyst and gaseous reactant), are particularly desirable in industrial processes because they allow for easy separation of reactants and products from the catalyst. Over 60% of all industrial chemical production processes involve the participation of a

catalyst at some stage,[1] and among these processes are a number of the largest-scale, energy-intensive reactions performed by mankind. Important examples of heterogeneous catalytic processes include synthesis of ammonia (~130 million tons annually)[2] and synthesis of polyethylene (~80 million tons annually)[3], which are both roughly $100 billion/year industries. Ammonia production alone accounts for over 1% of total global energy consumption, which currently averages over 15 terawatts.[4,5] About 75% of this energy comes from fossil fuels, with roughly equal contributions from oil, coal, and natural gas.[4,5] Numerous stages of the oil refining process involve catalytic conversions, as does the combustion of residual hydrocarbons and carbon monoxide from consumed fossil fuels by catalytic converters.

Rising global demands for energy, coupled with diminishing fossil fuel reserves and growing concerns over pollution and climate change, has fostered a considerable need for clean, efficient, and renewable energy sources, as well as improved processes for the production of commodity chemicals with higher energy efficiency, higher selectivity to desired products (atomic efficiency), and utilization of non-traditional feedstocks. Because the rates of chemical reactions typically increase with temperature, improving catalysts generally serves the role of reducing the energy input required to drive reactions by lowering operating temperatures. On a more fundamental level, this corresponds to stabilization of intermediate species formed during a reaction, lowering the energetic barrier between reactants and products (discussed later and depicted in Figure 1-3). When multiple reactions can proceed simultaneously, catalytic materials can often be used to selectively

speed up the rate of one pathway relative to another and generate desired products over unwanted byproducts. In addition to optimizing current chemical processes, new discoveries in catalysis will be necessary for developing sustainable alternatives to existing technologies. Heterogeneous catalysis has, and will continue, to play a pivotal role in achieving more sustainable production of energy and commodity chemicals.

1.2 Electro-Catalysis and Fuel Cells

Many chemical reactions can be driven using electrical energy in addition to thermal energy. Likewise, high-energy chemical compounds may be electrochemically decomposed to directly produce electricity at high efficiency, much like the conversion of traditional fuels directly to heat through combustion. Electrochemical transformations are of particular interest for distributed and mobile energy-production applications (transportation, portable electronics, etc), where startup, shutdown, and rate fluctuations occur frequently and there is little opportunity to utilize waste heat that would be generated in combustion. These processes are also useful for driving energetically-uphill molecular transformations, meaning electricity from renewable sources like wind and solar power may be efficiently converted to fuels (e.g. water electrolysis to form hydrogen or reduction of CO_2 to methanol or other fuels).

Electrochemical reactions can be performed at the interface of an electronic conductor (an electrode) and an ionic conductor (an electrolyte). This is

schematically depicted in Figure 1-1, which shows a simple electron transfer reaction occurring at an electrode surface. The potential of the electrode influences the reaction rate (or vice versa, depending on the application), and in many cases the reactive species also interact chemically with the electrode surface, meaning it acts catalytically. As an electro-catalyst, an ideal electrode can perform electron transfer chemistry at potentials near the thermodynamic equilibrium potential of a reaction without sacrificing additional potential (termed "overpotential") and thus energy.

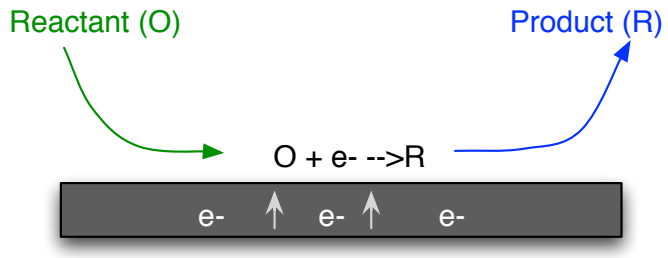

Figure 1-1: General scheme of electrochemical reaction. A reducible molecule "O" interacts with an electrode surface, gains an electron, and undergoes molecular rearrangement, forming species "R".

Electrode reactions are often paired; spatially isolated electrodes are placed in contact with an ionic conduction path (the electrolyte) and electronic conduction path (an external circuit), such that current ultimately flows between the electrodes as each independent electron transfer reaction proceeds. Each electrode reaction is often referred to as a "half reaction," and such pairing is the basis of an electrochemical cell—a battery is a common example. A related electrochemical technology with great potential for efficient energy conversion is the hydrogen fuel cell. A fuel cell is, in essence, a battery with continuously replenishable reactants.

Hydrogen is an attractive electrochemical "fuel" primarily because it is easy to activate chemically at low temperature and it allows the use of air as an oxidant. The archetypal hydrogen fuel cell design,[6] depicted in Figure 1-2 comprises two electrodes—an anode and cathode—separated by an electrolyte solution or membrane. Oxidation of hydrogen occurs at the anode while reduction of oxygen takes place at the cathode, generating an electrical potential across the cell. Current flows through an external circuit as the reactions proceed, and the reagents (O_2 and H_2) are continuously replenished in each electrode compartment. The participating majority charge carriers, which may be protons or hydroxide ions depending on pH, are shuttled across the electrolyte, completing the circuit.

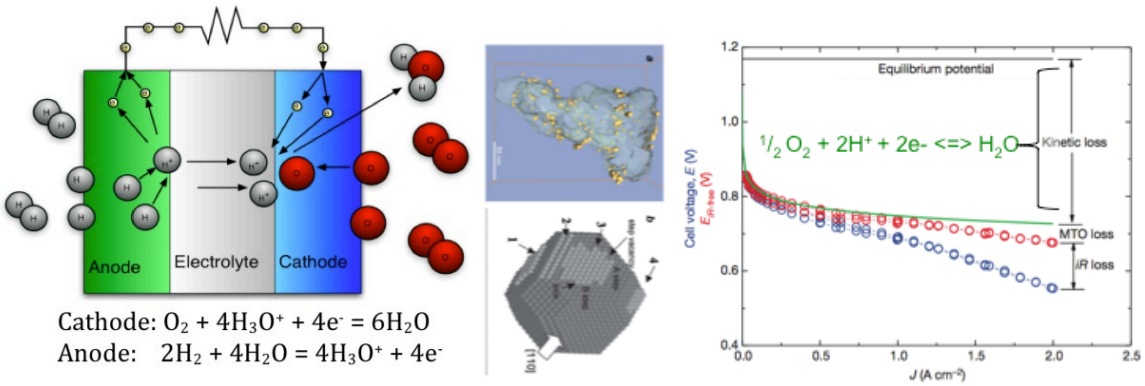

Figure 1-2: Design and typical performance of a PEM fuel cell. *Left:* Basic design and electrode reactions for a hydrogen fuel cell. *Center:* Tomographic reconstruction of supported catalyst particles from a fuel cell cathode and model of a typical Pt catalyst nanoparticle.[7,8] *Right:* Current-voltage performance of a state-of-the-art PEM cell using Pt electro-catalyst electrodes.[9]

Efficiency losses may occur in fuel cells due to a number of factors, including mass-transport limitations, kinetic barriers at each of the electrodes, and ionic resistance of the electrolyte (Ohmic loss). Additional contact resistances can appear

when cells are stacked in series. In practice, the largest source of efficiency loss is the sluggish kinetics of the oxygen reduction reaction (ORR) at the cathode,[6,9–12] which is illustrated with a typical current vs. operating voltage curve with various losses labeled in Figure 1-2. Overcoming the ORR barrier has historically required the use of platinum as a catalyst. Though platinum is the best pure-metal ORR electro-catalyst, even it exhibits an appreciable activation barrier, which is manifested as a sacrifice in operating voltage, or kinetic "overpotential" loss. For reference, the thermodynamic maximum (open circuit) voltage for an H_2/O_2 cell is 1.23 V (at room temperature), whereas a typical cell using Pt catalyst will yield only about 0.9 V when any significant current is drawn.

1.2.1 Current State-of-the-Art and Future Challenges

While hydrogen fuel cells hold promise for improving the efficiency of energy consumption, particularly in transportation, Pt is very expensive (presently ~$1600/oz)[13] and still not an optimal electro-catalyst for ORR. Typical Pt ORR catalysts, which take the form of nanometer-scale particles supported on high surface area conductive materials, represent about half the cost (projected by the US DOE and accounting for economies of scale) of an automotive proton-exchange membrane fuel cell (PEMFC) stack required to deliver ~80 KW.[14] A great body of work has been generated in the last several decades focusing on the development of cheaper electro-catalysts that outperform Pt in ORR activity, or at least achieve comparable performance at lower cost. Activity and cost improvements have primarily been made by alloying Pt with other transition metals such as Ni, Co, and

Fe,[15–18] and it has also been reported that single atomic layers of Pt can be deposited on lower cost particles, such as Pd or Au-alloys[19–23], and show improved activity compared to Pt with extremely low Pt content. While these multimetallic systems outperform Pt significantly in initial activity, they also tend to be more vulnerable to deactivation than pure Pt due to dissolution of the less noble elements or of the thin Pt overlayers into the acidic PEM electrolyte.[18,24,25] A summary of key performance metrics for current Pt-based ORR catalyst materials and economically viable targets for automotive fuel cells (by DOE standards) is given in Table 1-1.

Cathode Catalyst	Mass Activity	Area Activity*	Durability (10% loss)	System Cost**
DOE Target (Pt-based)	0.44 A/mg @0.9V	~720μA/cm$^2_{Pt}$	5000 h	$30/kW
Commercial Pt	0.12 A/mg	200μA/cm$^2_{Pt}$	4000 h	$75/kW
Best Pt-alloys ($Pt_{1-x}Co_x$)	0.24 A/mg	550μA/cm$^2_{Pt}$	2500 h	$50/kW

Table 1-1 Current performance benchmarks and targets for Pt-based oxygen reduction catalysts for hydrogen fuel cells.[6,9,12,14] Catalyst activity and stability levels are given. *Mass and area specific activities are not necessarily directly proportional due to differences in catalyst dispersion. **System costs include balance of plant expenses such as gas compressors and assembly. Advances in these areas are assumed in the DOE target cost of $30/kW for a complete system.

As is evident from Table 1-1, current state-of-the-art Pt-alloy electrocatalysts can achieve about twice the ORR activity per gram of Pt-group metal (PGM), but still contribute significantly to high fuel cell stack costs and also fall short of the DOE 5000h lifetime target (to 10% voltage loss) for most transportation applications.[9,14] Activity enhancement by at least an additional factor of two will be required, with

better long-term stability, and necessary activity levels are likely to be even higher if mass production drives Pt prices upward.[6,9,12,14] While an exhaustive review of Pt-based catalysts with individual pros and cons is beyond the scope of this work, it suffices to say that the parameter space of Pt and Pt-alloy particle size, morphology, and composition has been thoroughly explored, activity improvements have effectively plateaued, and gains in activity often induce sacrifices in stability.[9,26]

Although no known materials can perform ORR at higher rates than Pt-based catalysts, an alternative is to focus on lower-cost catalysts that do not necessarily exhibit high activity by current standards, but are inexpensive enough that the quantity required is unimportant. If a so-called "costless catalyst" can be utilized, activity targets can be decreased about an order of magnitude (on a catalyst volume basis) before reaching electrode thickness limits for effective mass transport and a break-even point in cost due to use of larger cell components.[6,9,12,27] This metric presumes a comparable volumetric density of active sites, and thus targets will be higher for many non-metallic materials. Performance metrics for current state-of-the-art materials, generally based on single-atom transition-metal centers incorporated into doped graphitic frameworks, are given alongside DOE target values and Pt-catalyst volumetric activities in Table 1-2.

Cathode Catalyst	Volumetric Activity	Durability (10% loss)*	System Cost**
DOE Target "Costless"	130 A/cm^3 @0.8V	5000h	$30/kW
Best "Costless" (nanostructured Fe-phenanthroline)	230A/cm^3	100-1000h*	$40/kW
Commercial Pt	1300 A/cm^3	4000h	$75/kW

Table 1-2 Current performance benchmarks and targets for Pt-free oxygen reduction catalysts for hydrogen fuel cells.[12,28–30] Catalyst activity and stability levels are given. *Pt-free ORR catalysts are subjected to less rigorous stability testing than Pt-based materials. The number above is estimated based on tests at 0.5 V cell voltage. **System costs include balance of plant expenses such as gas compressors and assembly. Advances in these areas are assumed in the DOE target cost of $30/kW for a complete system.

Given the present difficulties with identifying adequate catalytic materials for ORR, it may be argued that a more systematic approach must be taken to identify materials that may display sufficient catalytic performance and stability, or if any such materials even exist. In the following section the emerging area of bottom-up catalyst design based on molecular-level insight is discussed.

1.3 Rational Catalyst Design

Most heterogeneous catalytic reactions involve a complex series of elementary chemical transformations taking place on catalytically active surface sites. Due to a fairly limited understanding of the elementary mechanisms of surface reactions and the fundamental physical factors that govern these reactions, most commercial heterogeneous catalysts have been discovered through experimental trial and error.[31–33] The primary problem with this Edisonian approach is that the catalysts it

yields, even when commercially viable, are often hampered by low energy efficiencies due to high activation barriers, and large environmental footprints, caused by either poor product selectivity or environmentally harmful reagents. This lack of complete control over catalytic chemical conversions necessitates that commercial catalytic processes be integrated into more complex systems that can efficiently harvest the waste energy and undesired byproducts.

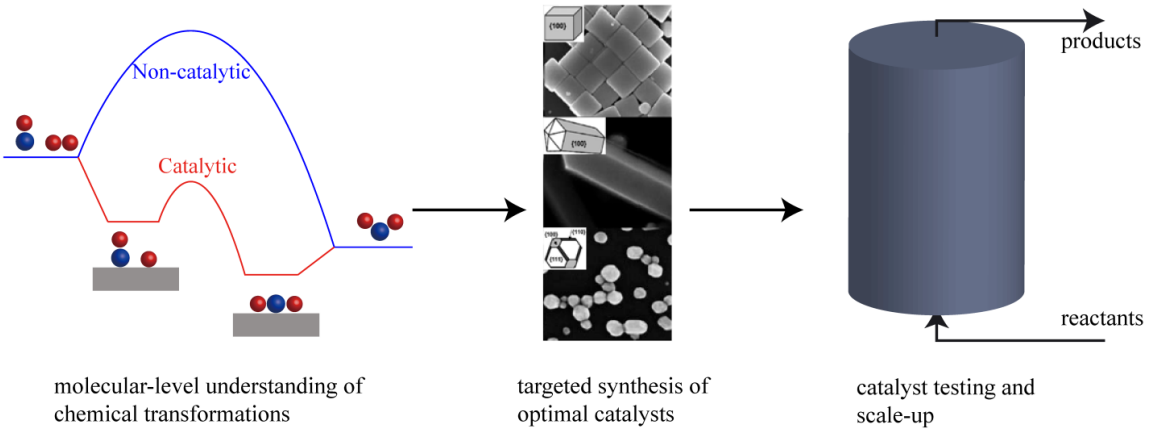

Figure 1-3: Bottom-up approach to catalyst design. Detailed understanding of the molecular transformations is employed to identify desired actives sites, which are then synthesized and tested.

Historically, there has been a significant interest in advancing predictive theories of heterogeneous catalysis aimed at the bottom-up design of more energy efficient and/or selective catalysts. Bottom-up catalyst design, conceptually depicted in Figure 1-3, is based on attaining a detailed understanding of the molecular transformations that govern catalytic processes and controlling these transformations through targeted synthesis of optimal materials. Advances in a

number of fields in past years have collectively enabled a methodology for rationally identifying optimal catalytic materials. Some of these include:

1) *Quantum chemical theory breakthroughs and improved computing resources*, permitting accurate and computationally manageable descriptions of chemical systems. These methods, including the highly utilized Density Functional Theory (DFT), permit calculation of molecular geometries, reaction energies, and activation barriers, which can be used to predict catalytic interactions and reaction mechanism from first principles. The electronic structure of solid materials can also be probed and related to reactivity.[34–36]
2) *Surface science of well defined model systems*, allowing characterization of specific active surface sites and their interactions with molecular adsorbates. These techniques generally have been made possible by ultra-high vacuum conditions ($<10^{-12}$ atm), which permit exposure of single-crystal "model catalysts," with specified surface termination, to controlled quantities of various reactive species, which can then be characterized with various vibrational and electronic spectroscopies to discern the nature of elementary reaction steps.[37–39]
3) *Sub-nanometer imaging and spatially resolved spectroscopy,* allowing direct observation of the atomic structure of catalytic materials, including high resolution compositional mapping and direct measurement of electronic structure. Electron microscopy forms the basis for such analysis, and with the newest generation of aberration-corrected scanning transmission

electron microscopes it is possible to reduce probe diameters below 1 Å, meaning that excitations and corresponding spectroscopic signals from a sample can be localized with high precision.[40–42]

4) *Highly controlled catalyst synthesis methods,* which in contrast to conventional catalyst preparations involving decomposition of precursor salts, exploit metal interactions with specialized atmospheres, solvents, surfactants, and/or additional ligands to guide the nucleation and growth of particles, creating specific geometries terminated in particular surface facets. Uniform catalysts with controlled structure can be exploited to selectively drive chemistries that are unique to the specific structure.[43–45]

1.4 Scope of the Dissertation

The overarching goal of this dissertation is to apply insights from a fundamental understanding of molecular-level interactions and heterogeneous reaction kinetics to interpret macroscopic reactivity trends in electrochemical systems and to design optimal electro-catalysts. The electrochemical oxygen reduction reaction (ORR) is chosen as a focal point due to its great potential impact on energy production. Herein we demonstrate that the experimentally observed kinetic response of the ORR to electrode potential, as well as reactant concentrations, is readily interpreted in terms of elementary steps, and that the kinetic behavior is a distinguishing fingerprint of the elementary mechanism. This mechanistic understanding provides clear design criteria for improved catalytic materials and is discussed for current-standard Pt-based catalyst materials, as well

as Ag, which is a potential basis for economical next-generation ORR catalysts. We then discuss the experimental development of Ag-based alloy materials with 3d-transition metals and demonstrate their improved ORR activity.

In Chapter 2, fundamental concepts governing the rate of reactions on catalytic and electro-catalytic materials are introduced, and classic rate theories are reviewed. Modern theories of chemisorption and trends in catalytic activity across materials are discussed in relation to the electronic structures of materials. The chapter concludes with a detailed discussion of the design of optimal catalytically active sites. The central issues addressed are: (i) How to identify the critical molecular descriptors of catalytic performance and (ii) How to search for optimal active sites, based on these critical descriptors.

Chapter 3 reviews a number of the experimental techniques and theoretical modeling methods used in this work. The chapter outlines the various methods with an emphasis on the underlying scientific principles upon which they are based. The aim is to develop an understanding of each method that will make clear its applicability when a particular piece of information is sought. Theoretical methods including density functional theory calculations and microkinetic modeling are discussed, followed by catalyst synthesis techniques, electrochemical characterization and performance evaluation, and atomistic characterization with various microscopic and spectroscopic techniques. Where applicable, specific alterations or constraints pertinent to our work synthesizing, characterizing, and modeling metal/alloy ORR catalysts are discussed. Experiment-specific conditions are deferred until later chapters in where specific results are discussed.

In Chapter 4, we use microkinetic modeling to illustrate that deviations from ideal Tafel kinetics, which assume a linear relationship between electrode potential and log-current, are an inherent property of multi-step heterogeneous electrocatalytic reactions. We show that in general, deviations from ideal Tafel behavior can often be attributed to a simultaneous increase in the rate of the rate-limiting elementary step and a change in the number of available active sites on the electrode as overpotential is induced. Our analysis shows that in the oxygen reduction reaction (ORR) on Pt electrodes, which exhibits nonlinear Tafel behavior, changing the electrode potential affects not only the rate-limiting step (the initial electron transfer to molecular oxygen), but also the concentration of surface intermediates—mainly OH and H_2O. Based on comparison of measured and predicted changes in Tafel slope (as well as pH dependence), we show that alternative interpretations of the non-ideal Tafel behavior of ORR on Pt, such as changes in rate-limiting step or adsorbate repulsion effects, are inconsistent with the observed ORR kinetics.

Chapter 5 provides a comparative study of the ORR kinetic parameters in alkaline environments, using cyclic voltammetry (CV) and rotating disk electrode (RDE) kinetic measurements to compare the rates on each material and how these rates vary as a function of potential and adsorbate coverage. The apparent transfer coefficient and reaction orders with respect to hydroxyl ion concentration and oxygen partial pressure are found to be consistent with a microkinetic model in which the first electron transfer to molecular oxygen is rate limiting. However, we find that in contrast to Pt, where changes in the rate parameters correlate well to

adsorbate coverage on the surface, a very weak relation exists between adsorbate coverage and changes in the kinetics on Ag. This points to a strong role of undercoordinated sites, which can become poisoned at lower potential than the more well-coordinated surface facets. Thus for Ag, moving in the direction of stronger binding should lead to higher ORR activity by increasing turnover rates on the more predominant surface facets, whereas Pt suffers from poisoning of essentially all sites and can only be made more active by moving to compositions with weaker affinity toward oxygen.

In Chapter 6, we demonstrate the design of relatively inexpensive Ag-Co surface-alloy nanoparticle electro-catalysts for the ORR, with equivalent area-specific activity to commercial Pt-nanoparticles at 0.8V (reversible hydrogen electrode scale), and more than five-fold improved performance over pure Ag nanoparticles. The Ag-Co materials were identified with quantum chemical calculations and synthesized with a novel technique that generates a surface alloy, despite the bulk immiscibility of the constituent materials. Characterization studies show that the origin of the activity improvement comes from a ligand effect, in which Co perturbs the Ag surface sites and improves their inherent activity. The observed enhancements in the ORR activity of Ag through alloying represent an important step towards making fuel cell technology viable.

In Chapter 7 we explore the use of rapid reduction of bimetallic $Ag_x[M(CN)_y]$ precursors (M=Fe, Ni, Co) as a possible means to induce alloying between the metals and enhance ORR activity relative to pure Ag. The materials were characterized with x-ray diffraction at each stage of synthesis, as well as cyclic voltammetry to assess

surface reactivity. Oxygen reduction activity measurements show relatively high activity for Ag-Co. However, Ag-Ni and Ag-Fe exhibit similar activity to monometallic Ag, which can be attributed to a failure to produce alloying. We relate the segregation of these materials to the structure and stability of the individual precursors.

In Chapter 8 we summarize the major findings throughout this work and discuss their impact with relation to heterogeneous catalysis and electro-catalysis. We discuss outstanding questions and possible directions for continued research.

1.5 References

1. Van Santen, R. A. & Neurock, M. *Molecular heterogeneous catalysis: a conceptual and computational approach*. (Wiley-VCH, 2006).

2. Appl, M. Ammonia. *Encyclopedia of Industrial Chemistry* (2006).

3. Whitely, K. Polyethylene. *Encyclopedia of Industrial Chemistry* (2011).

4. *U.S. DOE Energy Information Adminsistration International Energy Outlook*. (2011).

5. Lewis, N. & Nocera, D. Powering the planet: Chemical challenges in solar energy utilization. *Proc. Nat. Acad. Sci.* **103,** 15729–15735 (2006).

6. Borup, R. *et al.* Scientific aspects of polymer electrolyte fuel cell durability and degradation. *Chemical Reviews* **107,** 3904–3951 (2007).

7. Gontard, L. C., Dunin-Borkowski, R. E. & Ozkaya, D. Three-dimensional shapes and spatial distributions of Pt and PtCr catalyst nanoparticles on carbon black. *J. Microscopy* **232,** 248–259 (2008).

8. Gontard, L. C. *et al.* Aberration-Corrected Imaging of Active Sites on Industrial Catalyst Nanoparticles. *Angew. Chem. Int. Ed.* **46,** 3683–3685 (2007).

9. Debe, M. K. Electrocatalyst approaches and challenges for automotive fuel cells. *Nature* **486,** 43–51 (2012).

10. Markovic, N. M., Schmidt, T. J., Stamenkovic, V. R. & Ross, P. N. Oxygen Reduction Reaction on Pt and Pt Bimetallic Surfaces: A Selective Review. *Fuel Cells* **1,** 105–116 (2001).

11. Antoine, O., Bultel, Y. & Durand, R. Oxygen reduction reaction kinetics and mechanism on platinum nanoparticles inside Nafion{Æ}. *J. Electroanalytical Chem.* **499,** 85–94 (2001).

12. Gasteiger, H. A., Kocha, S. S., Sompalli, B. & Wagner, F. T. Activity benchmarks and requirements for Pt, Pt-alloy, and non-Pt oxygen reduction catalysts for PEMFCs. *Applied Catalysis B: Environmental* **56,** 9–35 (2005).

13. *Mineral Commodity Summaries 2010*. (2010). at <http://minerals.usgs.gov/minerals/pubs/mcs/>

14. The US Department of Energy (DOE). Energy Efficiency and Renewable Energy. at <http://www1.eere.energy.gov/hydrogenandfuelcells/mypp/>

15. Paulus, U. A. *et al.* Oxygen reduction on high surface area Pt-based alloy catalysts in comparison to well defined smooth bulk alloy electrodes. *Electrochimica Acta* **47,** 3787–3798 (2002).

16. Koh, S. & Strasser, P. Electrocatalysis on bimetallic surfaces: Modifying catalytic reactivity for oxygen reduction by voltammetric surface dealloying. *J. Am. Chem. Soc.* **129,** 12624–+ (2007).

17. Stamenkovic, V. R. *et al.* Improved oxygen reduction activity on Pt3Ni(111) via increased surface site availability. *Science* **315,** 493–497 (2007).

18. Cui, C., Gan, L., Heggen, M., Rudi, S. & Strasser, P. Compositional segregation in shaped Pt alloy nanoparticles and their structural behaviour during electrocatalysis. *Nature Materials* **12,** 765–771 (2013).

19. Zhang, J. L. *et al.* Mixed-metal Pt monolayer electrocatalysts for enhanced oxygen reduction kinetics. *J. Am. Chem. Soc.* **127,** 12480–12481 (2005).

20. Zhang, J. *et al.* Platinum monolayer on nonnoble metal-noble metal core-shell nanoparticle electrocatalysts for O-2 reduction. *J. Phys. Chem. B* **109,** 22701–22704 (2005).

21. Sasaki, K. *et al.* Core-Protected Platinum Monolayer Shell High-Stability Electrocatalysts for Fuel-Cell Cathodes. *Angew. Chem. Int. Ed.* **49,** (2010).

22. Gong, K., Su, D. & Adzic, R. R. Platinum-monolayer shell on AuNi(0.5)Fe nanoparticle core electrocatalyst with high activity and stability for the oxygen reduction reaction. *J. Am. Chem. Soc.* **132,** 14364–6 (2010).

23. Sasaki, K. *et al.* Recent advances in platinum monolayer electrocatalysts for oxygen reduction reaction: Scale-up synthesis, structure and activity of Pt shells on Pd cores. *Electrochimica Acta* **55,** 2645–2652 (2010).

24. Wang, D. *et al.* Structurally ordered intermetallic platinum–cobalt core–shell nanoparticles with enhanced activity and stability as oxygen reduction electrocatalysts. *Nature Materials* **13,** 81–87 (2013).

25. Xin, H. L. *et al.* Atomic-resolution spectroscopic imaging of ensembles of nanocatalyst particles across the life of a fuel cell. *Nano letters* **12,** 490–7 (2012).

26. Guo, S., Zhang, S. & Sun, S. Tuning Nanoparticle Catalysis for the Oxygen Reduction Reaction. *Angew. Chem. Int. Ed.* n/a–n/a (2013). doi:10.1002/anie.201207186

27. Wagner, F. T., Lakshmanan, B. & Mathias, M. F. Electrochemistry and the Future of the Automobile. *J. Phys. Chem. Lett.* **1,** 2204–2219 (2010).

28. Proietti, E. *et al.* Iron-based cathode catalyst with enhanced power density in polymer electrolyte membrane fuel cells. *Nature Communications* **2,** 416 (2011).

29. Wu, G., More, K. L., Johnston, C. M. & Zelenay, P. High-performance electrocatalysts for oxygen reduction derived from polyaniline, iron, and cobalt. *Science* **332,** 443–7 (2011).

30. Lefèvre, M. Iron-Based Catalysts with Improved Oxygen Reduction Activity in Polymer Electrolyte Fuel Cells. *Science* **324,** 71–74 (2009).

31. Weissermel, K. & Arpe, H. J. *Industrial Organic Chemistry*. (Wiley-VCH, 1993).

32. Horvath, I. T. *et al. Encyclopedia of Catalysis*. (Wiley & Sons, 2002).

33. Ertl, G., Knoezinger, H. & Weitkamp, J. *Handbook of Hetergeneous Catalysis*. (Wiley-VCH, 1997).

34. Norskov, J. K. *et al.* Universality in heterogeneous catalysis. *J. Catal.* **209,** 275–278 (2002).

35. Ruban, A., Hammer, B., Stoltze, P., Skriver, H. L. & Norskov, J. K. Surface electronic structure and reactivity of transition and noble metals. *J. Molecular Catalysis* **115,** 421–429 (1997).

36. Nørskov, J. K., Abild-Pedersen, F., Studt, F. & Bligaard, T. Density functional theory in surface chemistry and catalysis. *Proc. Nat. Acad. Sci.* **108,** 937–43 (2011).

37. Ertl, G. Reviews Reactions at Surfaces : From Atoms to Complexity (Nobel Lecture). 2–14 (2008). doi:10.1002/anie.200800480

38. Goodman, D. W. Model Studies in Catalysis Using Surface Science Probes. *Chemical Reviews* **95,** 523–536 (1995).

39. Linic, S. & Barteau, M. a. Formation of a stable surface oxametallacycle that produces ethylene oxide. *J. Am. Chem. Soc.* **124,** 310–7 (2002).

40. Batson, P. E., Dellby, N. & Krivanek, O. L. Sub-Ångstrom resolution using aberration corrected electron optics. *Nature* **418,** 617–20 (2002).

41. Krivanek, O. L. *et al.* Atom-by-atom structural and chemical analysis by annular dark-field electron microscopy. *Nature* **464,** 571–4 (2010).

42. Muller, D. a *et al.* Atomic-scale chemical imaging of composition and bonding by aberration-corrected microscopy. *Science* **319,** 1073–6 (2008).

43. Zhang, J., Yang, H., Fang, J. & Zou, S. Synthesis and Oxygen Reduction Activity of Shape-Controlled Pt(3)Ni Nanopolyhedra. *Nano Letters* **10,** (2010).

44. Xia, Y., Xiong, Y. J., Lim, B. & Skrabalak, S. E. Shape-Controlled Synthesis of Metal Nanocrystals: Simple Chemistry Meets Complex Physics? *Angew. Chem. Int. Ed.* **48,** 60–103 (2009).

45. Christopher, P. & Linic, S. Shape- and Size-Specific Chemistry of Ag Nanostructures in Catalytic Ethylene Epoxidation. *ChemCatChem* **2,** 78–83 (2010).

Chapter 2: Fundamentals of Heterogeneous Catalysis and Electro-catalysis

Fundamental concepts governing the rate of reactions on catalytic and electro-catalytic materials are introduced, and classic rate theories are reviewed. Modern theories of chemisorption and trends in catalytic activity across materials are discussed in relation to the electronic structure of materials. The chapter concludes with a detailed discussion of the design of optimal catalytically active sites. The central issues addressed are: (i) How to identify the critical molecular descriptors of catalytic performance and (ii) How to search for optimal active sites based on these critical descriptors.

2.1 Classical Thermochemical Heterogeneous Kinetics

In most heterogeneous reactions, transformations proceed through multiple intermediate steps. These often include adsorption of products onto a catalyst surface, reaction(s) on the surface, and desorption of products. Such processes are depicted in Figure 2-1, alongside a hypothetical potential energy surface showing the relative stabilities of reactants, products, intermediates, and transition states between these stages. The study of chemical kinetics aims to develop relationships that can accurately describe the rates of chemical reactions. It is a vast field that is

discussed in numerous textbooks,[1–4] and will only be highlighted here insofar as the details that pertain to design of catalytic materials.

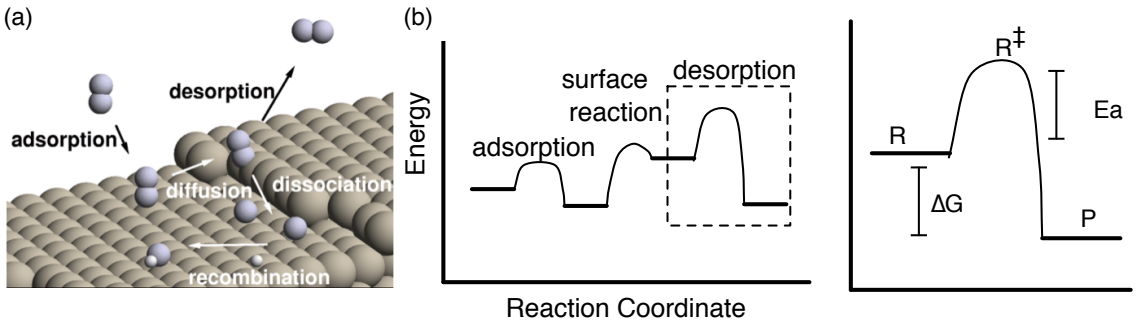

Figure 2-1: Elementary steps and the potential energy surface of a heterogenous reaction. (a) Depiction of various steps involved in a heterogeneous transformation (b) Potential energy of reactive species, intermediates, products and transition states as a reaction progresses (c) Potential energy surface of an elementary step

To begin, the rate of a chemical reaction is generally well described as being proportional to the activity (which scales with concentration or pressure) of each reacting species, raised to some power (the reaction order). Thus for two gaseous species 'A' and 'B' reacting, the forward reaction rate is given by the expression $r_f = k{\cdot}P_A{}^x P_B{}^y$, where k is the proportionality constant also known as the rate constant, P_i is the partial pressure of a given species, and x and y are their reaction orders. Rate constants were first noted by Arrhenius to vary with temperature, and generally fit the relationship given in Equation (2.1), where T is temperature, R is the ideal gas constant, and A and E_a are empirically determined parameters known as the preexponential factor and activation barrier.

$$k = A \cdot \exp\left(-E_a/RT\right) \tag{2.1}$$

Since reactions may be reversible and establish equilibrium over time, it is also important to note that the forward and reverse rates will eventually become equal. At this point, an equilibrium constant (K_{eq}) may be defined according to Equation (2.2), where pressure or concentration have been de-dimensionalized and replaced with the thermodynamic activity *a.*

$$K_{eq} = k_f/k_r = \prod_{\text{prod}} a_{i,\text{eq}}^{x_i} / \prod_{\text{reac}} a_{j,\text{eq}}^{x_j} \tag{2.2}$$

Since the net rate is the sum of forward and reverse reaction rates, if we define the approach to equilibrium, β, as the ratio of the reaction quotient ($Q = \prod_{prod} a_i^{x_i} / \prod_{reac} a_j^{x_j}$, at current conditions) to the equilibrium constant, the net rate may be compactly expressed as Equation (2.3). Kinetic studies are typically run under conditions of low product conversion so that reverse rates can be ignored, simplifying determination of kinetic parameters.

$$r = r_f \cdot (1 - \beta) \tag{2.3}$$

In cases where a reaction proceeds through multiple elementary steps, the rate law parameters in Eqn. (2.1) must only be considered as "apparent" quantities, without a precise interpretation in terms of molecular-level phenomena. In fact, in many cases an Arrhenius plot ($\ln(r)$ vs. $1/RT$) will deviate from the expected linearity due to complexities that will be discussed later in this chapter. For an elementary reaction, defined as a transformation involving only one step and one transition state, Eqn. (2.1) can be reexamined from a more fundamental basis. A prevailing description, known as Transition State Theory (TST), is based on the assumption that the transition state and reactant can be viewed as establishing

quasi-equilibrium, even though equilibrium between reactant and product is not established. Referring back to Figure 2-1(c), we consider the potential energy surface of a single elementary step. Using TST, we depict the elementary reaction from reactant to product as a series reaction, R ←→ R‡ → P, where 'R' represents the reactant, 'P' the product, and 'R‡' the transition state. We next express the rate of product formation as the product of the concentration of activated complex, [R‡], multiplied by an attempt frequency, ν, which is interpreted as the vibrational frequency along the reaction coordinate. Since R and R‡ are in quasi-equilibrium, this may be expressed symbolically as:

$$r = d[P]/dt = \nu \cdot [R^{\ddagger}] = \nu \cdot K_{eq}^{\ddagger} \cdot [R] \tag{2.4}$$

It can be inferred from Eqns. (2.4) that the rate constant can be expressed as: $k = \nu \cdot K_{eq}^{\ddagger}$. Next appealing to statistical mechanics (the reader is referred to appropriate textbooks[5,6]), $K_{eq}^{\ddagger}$ may be expressed as the ratio of partition functions for each state, q and $q^{\ddagger}$ (their ratio is effectively the ratio of probabilities each state is occupied). Statistical mechanics also dictates that individual contributions to the partition function may be factored out of the total partition function, and as such it is possible to extract the vibrational partition function of the activated complex along the reaction coordinate, q_ν. This quantity can be expressed as $q_\nu = k_b T/\nu h$, where k_b is the Boltzmann factor, h is Planck's constant, and ν is the same vibrational frequency of R‡ used in Eqns. (2.4). Taking these steps we find that the rate constant can be expressed according to Eqns. (2.5). Here the term q' has been introduced to denote that the reaction coordinate vibration frequency is separated from the partition function of R‡.

$$k = \nu \cdot K_{eq}^{\ddagger} = \nu \frac{q_\nu q'^{\ddagger}}{q} = \frac{k_b T}{h} \frac{q'^{\ddagger}}{q} = \frac{k_b T}{h} K_{eq}'^{\ddagger} \tag{2.5}$$

Using Eqns. (2.5), we may exploit the definition of the change in Gibbs free energy (ΔG=-RT·lnK_{eq}) to define a free energy of activation ($\Delta G^{\ddagger}$) and arrive at an Arrhenius-like rate law, known as the Eyring Equation:

$$k = \frac{k_b T}{h} \exp\left(-\frac{\Delta G^{\ddagger}}{RT}\right) = \frac{k_b T}{h} \exp\left(\frac{\Delta S^{\ddagger}}{R}\right) \exp\left(-\frac{\Delta H^{\ddagger}}{RT}\right) \tag{2.6}$$

While there are limitations to the Eyring rate equation—most notably its failure to capture quantum-tunneling effects that can be significant with light atoms—it applies to a wide range of reactions and conditions. The parameters in Eqns. (2.6) are accessible with computational chemistry techniques (and in some cases careful surface science experiments), and these can be used to construct rate models for full multistep reactions. This analysis forms a basis for comparison to apparent Arrhenius parameters measured experimentally.

2.2 Classical Electrochemical Kinetics

Electrochemistry is the branch of heterogeneous chemistry that deals with electron transfer reactions and other phenomena involving species that carry inherent charge. It is the topic of numerous dedicated texts,[7,8] and here we outline only the basic terminology and kinetic equations. While many thermochemical processes involve electron transfer from one species to another, electrochemistry differs in that oxidation and reduction generally are spatially and/or temporally separated. Consequently, individual electrode processes are often referred to as "half-reactions," which were illustrated for a fuel cell previously in Figure 1-2. Free

electrons participate directly in these half-reactions, and they must occur near the interface of an electronic conductor (the electrode) and an ionic conductor (the electrolyte). The participation of independent electrons—flowing from one electrode to another or vice versa—dictates that reaction rates depend not only on temperature, but also on electrode potential. One may also note that in these systems, it is often possible to utilize electronic control circuitry to force operation at a chosen current rather than a fixed potential. At steady state there should be a one-to-one mapping between these quantities, but we will develop the relevant kinetic equations as a function of potential. It is first necessary to establish how this potential is defined.

Unlike pure, thermochemical processes, in which the probability of surmounting an energetic barrier can be related to a well-defined intensive property, absolute temperate, electrochemical processes cannot be described in terms of an absolute potential. Instead, the driving force of these reactions must be defined in relation to the potential difference between the working electrode and a reference potential. It is worth noting that while numerous works have attempted to define electrode potentials on an absolute scale,[9–12] such definitions are predicated on the establishment of "zero" potential in a secondary reference state such as that of an electron in a field-free vacuum. This does not define a minimum or maximum possible energy for the electron, and electrode potential *difference* is still the only thermodynamically meaningful quantity that can be defined. While reference choices are arbitrary, the most convenient option is to choose a half-cell reaction that is relatively stable and measure the potential of a working electrode of interest

relative to it (instrumentation that allows for decoupling of the chemistry at each electrode when current flows will be discussed in Chapter 3).

For tabulation of thermodynamic data, it is common to list measured equilibrium potentials for half-reactions relative to the equilibrium of the reaction ½ H^+ + e- ←→ H_2 under standard conditions (solution with proton activity of unity, saturated with 1bar H_2 at 25°C), also known as the standard hydrogen electrode (SHE). Thus, a simple electrode equilibrium potential such as dissolution of silver, Ag ←→ Ag^+ + e^-, tabulated as 0.8V vs. SHE, corresponds to a measured potential difference of 0.8V between this reaction in equilibrium and the SHE. This potential also corresponds to the driving force required to move electrons through a circuit connecting one electrode to the other, and is equivalent to the free energy change for the net reaction (in this case Ag + H^+→Ag^+ + ½ H_2), divided by the number of electrons transferred, n, and Faradays's constant, F (96485 C/mol e^-), for appropriate unit conversion. In other words, $\Delta G=-nF\Delta E$ for any two half-reactions. These ΔE values may be derived for any pair of half reactions if their potentials are known on the SHE scale (or vs. any reference) due to cancellation of the reference value when taking differences—i.e. E_1-E_{ref}-(E_2-E_{ref}) = E_1-E_2. The equilibrium potentials of half-cell reactions may also be predicted with changes in conditions using the Nernst equation, Eqn. (2.7), which is an extension of the aforementioned relation between equilibrium constants and Gibbs free energy discussed in Section 2.1.

$$E_{eq} = E^\circ - \frac{RT}{nF} \cdot ln\left[\frac{\prod_{prod} a_i^{x_i}}{\prod_{reac} a_j^{x_j}}\right] \tag{2.7}$$

When potential deviates from its equilibrium value, current will flow through the electrode until equilibrium is restored. This is depicted in Figure 2-2(a), where the energy level of electrons in an electrode is shown relative to orbital energies of a hypothetical molecule. In the case shown, decreasing the electrode potential increases the energy of electrons, allowing them to reduce the molecule. Figure 2-2(b) shows a corresponding potential energy surface, illustrating how it changes shape as the potential decreases. The primary feature of interest in Figure 2-2(b) is that while the energy of the initial state, involving an electron contained in the electrode, is increased by the quantity $nF\Delta E$ (where ΔE is the applied change in potential), the energy of the transition state moves by only a fraction of this value. The fraction will be dictated by the symmetry of the potential energy surface along the reaction coordinate, and is known as the symmetry factor, β. For elementary reactions, the symmetry factor will always be between 0 and 1, and is found to be close to 0.5 in the majority of cases.

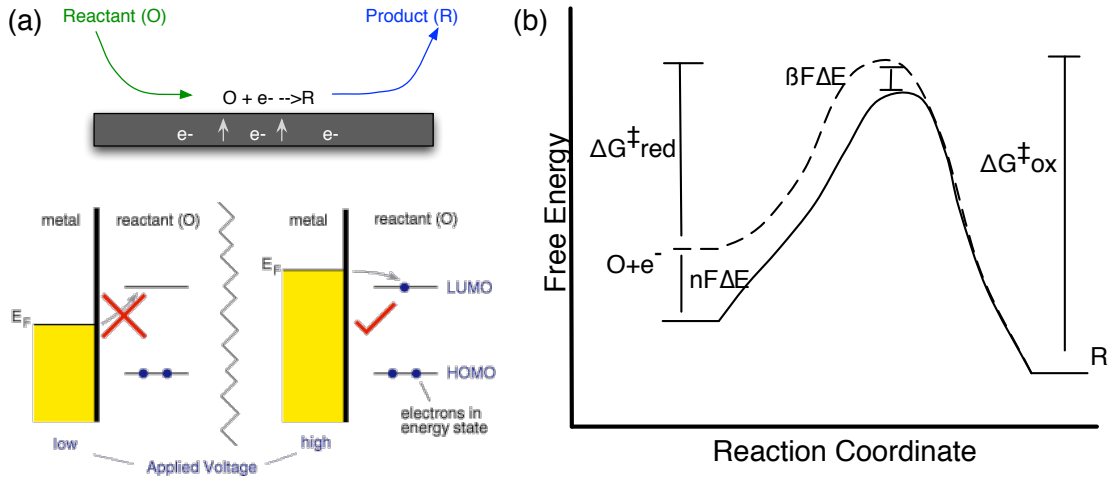

Figure 2-2: Basic principles of heterogeneous electron transfer. (a) Schematic of electron transfer from an electrode to a reactive species and the influence of electrode potential. Electrons in the electrode must have greater energy than a molecular orbital to populate it or lower energy to depopulate it. (b) Potential energy surface for an elementary electron transfer.

Considering the effect of electrode potential on the energy barrier between reactants and products, rate constants for an elementary electron transfer can be derived from transition state theory in an analogous manner to Eqns. (2.6), and the potential-dependent version is given in Equation (2.8), where $\Delta G^{0,\ddagger}$ designates the free energy barrier at the chosen reference potential E^0:

$$k = \frac{k_b T}{h} \exp\left(\frac{-\Delta G^{0,\ddagger} - n\beta F(E - E^0)}{RT}\right) \tag{2.8}$$

Rate expressions for each elementary step in a reaction then simply require multiplying the rate constant, in the form of Equation (2.8), by the activities of relevant species. Complex multistep reaction rates can then be constructed by developing systems of such elementary rate equations. However, as in heterogeneous reactions, it is common to describe an overall process empirically

with a single set of apparent parameters (rate constant, prefactor and reaction orders). Likewise it is common to ignore the weak dependence of the pre-exponential factor on temperature. Equation (2.9) gives an expression for the forward current density of a process that is far from equilibrium. In this expression several new parameters appear. First the number of electrons transferred overall, N, is divided by the stoichiometric number, ν, which designates the number of times the rate-limiting elementary step occurs for each overall molecular transformation. These may in some cases be lumped together with the rate constant k^0. Second, the symmetry factor has been replaced with an apparent parameter, α, known as the transfer coefficient, which describes the change in apparent barrier with respect to potential and may take on any value.

$$|i| = \frac{N}{\upsilon} \mathrm{F} k^0 \cdot \prod [a_i]^{x_i} \cdot \exp\left(\frac{-\Delta G^{0,\ddagger} - \alpha F(E - E^0)}{RT}\right) \tag{2.9}$$

Many electrochemical studies begin from a condition of equilibrium, and thus both forward and reverse rates must be considered. Additionally, due to the strong dependence of activation barriers on potential and the ease of rapidly sweeping through large electrical potential ranges (in comparison to temperature), it is quite simple to explore reaction kinetics in both the forward and reverse directions. Thus it is common in electrochemistry to use the equilibrium potential of the reaction being studied as the reference potential for theoretical analysis. Equation (2.10) shows the rate law for the net current density of an elementary electron transfer as a function of potential, also known as the Butler-Volmer Equation.

$$i = i_0 \left[\exp\left(\frac{(1-\beta)nF}{RT}(E - E_{eq}) \right) - \exp\left(\frac{-\beta nF}{RT}(E - E_{eq}) \right) \right] \quad (2.10)$$

The new parameter introduced in Eqn. (2.10), i_0, is known as the exchange current density. It lumps various constants, as well as the equilibrium concentrations of reactant and product, and describes the rate of equal-but-opposite current exchange at the electrode. In other words it is the magnitude of both the forward and reverse rates, even though the net current at equilibrium is zero. The rate of a typical electrochemical reaction near its equilibrium potential is shown in Figure 2-3(a), where the forward and reverse contributions to observed current are each illustrated along with the net current. Further from equilibrium, the current becomes dominated by one direction of electron transfer and a simple exponential relationship with potential is observed. In this limit it is common to analyze log-current vs. potential plots, known as Tafel plots, illustrated in Figure 2-3(b). The slope of the Tafel plot yields the transfer coefficient in an analogous manner to Arrhenius plots and activation barriers.

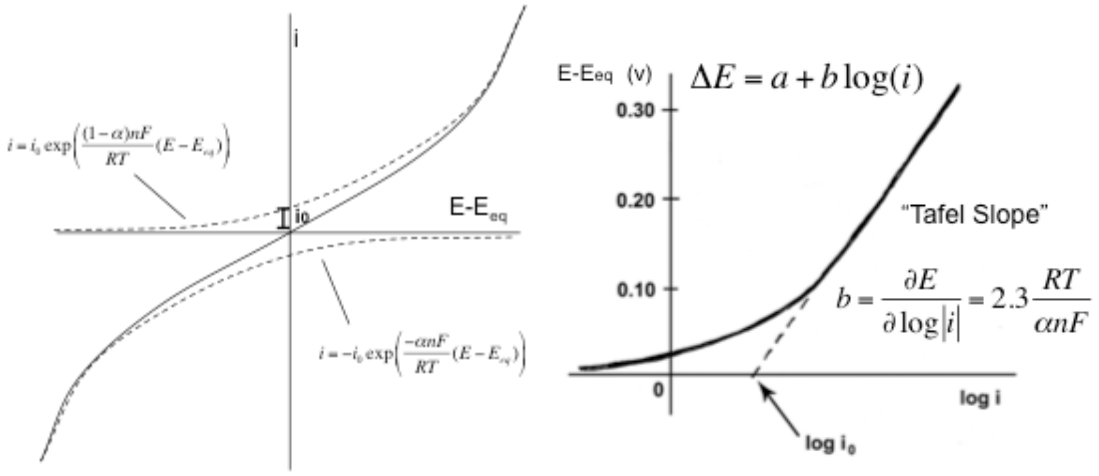

Figure 2-3: Rate of electron transfer vs. potential. (a) Butler-Volmer relationship for reversible reaction (b) Tafel relationship for reaction far from equilibrium

The kinetic framework discussed above provides a firm starting point for an analysis of electrochemical reaction rates. However, it may be necessary to consider a number of other effects in certain scenarios. Most importantly, the kinetics of many reactions are fast enough that the surface concentrations of reactive species are dictated entirely by equilibrium, and the reaction rates are controlled by mass transport. This is relevant primarily with certain single-electron processes that do not involve significant rearrangement of molecular bonds. The surface concentration (or flux in controlled current applications) effectively sets a boundary condition for mass transport. Such scenarios will not be discussed in detail as this work focuses on kinetics, but the reader is referred to appropriate texts on transport phenomena.[8,13] Additionally, due to the content of ionic species in electrolytes and the inherent charging of electrodes when a potential is applied, electrostatic interactions occur and attract an "electrochemical double layer" of accumulated ions, effectively turning the electrode into a crude capacitor. Currents

arising from such non-reactive processes, also known as non-Faradaic current, must be taken into consideration when analyzing experimental results. Finally, interactions of reactive species with these weakly adsorbed ions, as well as solvent molecules and electric fields may play a role and must be addressed as required.

2.3 Catalytic Materials Selection

Having discussed the basic concepts governing heterogeneous thermochemical and electrochemical reactions, it is now possible to study in more detail the role of catalysts and the mechanisms through which they influence reaction rates. This section will mainly focus on the design of optimal catalytically active sites, with emphasis on metal/alloy catalysts, which are a very broad and important class of materials for both thermal and electrochemical processes. Here, an active site will be defined as a collection of catalyst surface atoms that directly participate in a catalytic cycle, through chemical bond breaking and formation, and the neighboring atoms that could influence the energetics of these processes. We focus on (i) How to identify critical molecular descriptors of catalytic performance and (ii) How to search for optimal active sites based on these critical descriptors.

2.3.1 The Sabatier Principle

It has been recognized since the late 19th century that a catalytic material must interact strongly enough with a molecule to influence its transformation, but not so strongly as to irreversibly bind the product—a concept that was first articulated by

the chemist Paul Sabatier and is now known as the Sabatier principle. This simple principle still forms the basis of the modern understanding of catalysis, which we begin to discuss below with a limited but instructive analysis of the rate of a catalytic chemical reaction taking place on the surface of an extended solid material (a collection of active sites).

For the sake of discussion, we assume a hypothetical two-step reaction mechanism in which species 'A' reacts to form species 'B.' In the mechanism, A first adsorbs to form the surface-bound intermediate A*, then reactively desorbs forming B. Assuming a particular rate-limiting elementary step (adsorption or desorption here), the steady state turnover frequency (TOF) of such a catalytic transformation can be expressed in terms of an intrinsic rate (intrinsic TOF), which contains reactant activities and a rate constant dependent solely on catalyst material, multiplied by the fraction of active sites that are available for the reaction (condition and material dependent), i.e., site that are not occupied by adsorbates (A* in this case) or impurities under steady state conditions. We give this simple relation in Equation (2.11), where θ_{ads} is the total coverage of adsorbates.[2,14–16]

$$\mathrm{TOF} = \mathrm{TOF}_{\mathrm{int}} \cdot (1 - \theta_{\mathrm{ads}}) \qquad (2.11)$$

The intrinsic reaction rate will be influenced by (i) the activation energy for the rate limiting elementary step (RLS), and (ii) the energy of formation of the reactants involved in the RLS with respect to the reactant state. These two contributions together dictate the energetic difference between the transition state in the RLS and the reactant state. We label this quantity $\Delta H^{\ddagger}_{\mathrm{intrinsic}}$ and illustrate the concept with a potential energy surface for the A→B reaction, assuming limitation

by formation of B, in Figure 2-4. As one might intuitively expect, a highly reactive surface will adsorb A strongly, pushing down the net intrinsic barrier. However, the fractional occupancy of free sites depends on (iii) the energy associated with the removal of reaction intermediates from the surface of the catalyst, given by the coverage of an intermediate multiplied by its desorption energy (summed over all intermediate species). This effectively means that on a highly reactive surface there will also be very few sites available for new reactants to adsorb. The sum of contributions (i), (ii), and (iii) mentioned above will yield the apparent activation barrier for the process under given conditions. Catalysts that exhibit the highest turnover rates will thus be characterized by a low activation barrier for the RLS and small energies of adsorption for intermediates involved in the catalytic cycle.

It is also worth noting that if we choose not to frame the kinetics in terms of a specific rate-determining step, a similar conclusion will be met. As the catalytic surface is changed from one that binds adsorbates very weakly to one that binds adsorbates very strongly, the degree to which a given step controls the rate will change—in other words we can view a decreasing number of available sites as a transition from limitation by adsorption to limitation by desorption. While such an approach can become analytically cumbersome for reactions with many steps, it is often the case that the kinetics will be dominated only two elementary steps across a wide range of catalysts. An optimal catalyst will strike a balance between these processes, binding the reactants strongly enough to activate them, but not so strongly as to be unable to release the products.

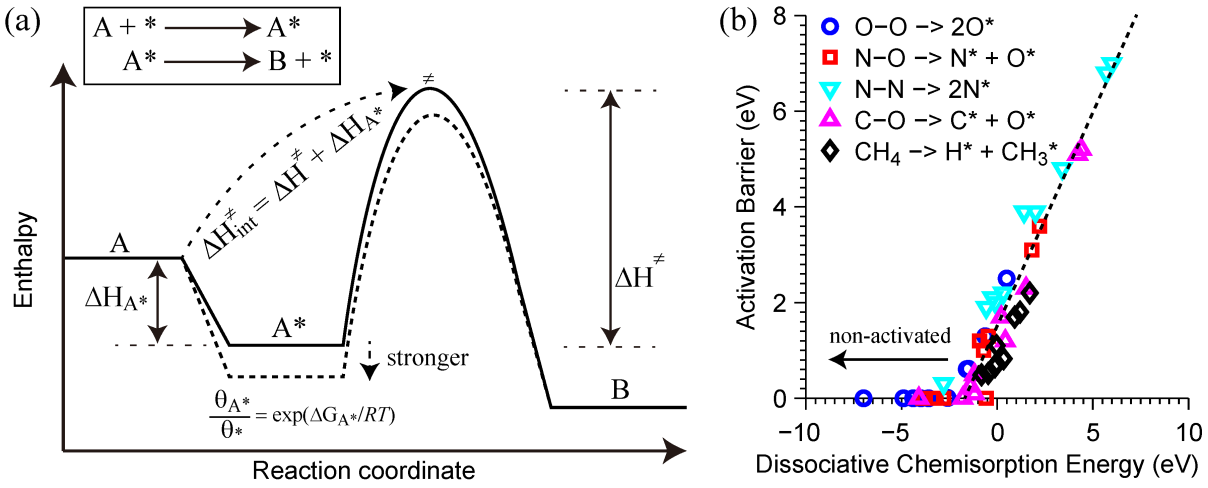

Figure 2-4: Trends in the potential energy surface. (a) Schematic of the potential energy surface for a simple two-step reaction mechanism for the transformation A→B, where * denotes an adsorbed species. (b) Linear scaling (Brønsted-Evans-Polanyi relationship) between dissociative chemisorption energies of simple molecules and the corresponding activation barriers for their dissociation on various transition metals, calculated with DFT. All data points with a given symbol represent the same molecule on different surfaces. O_2, NO, and N_2 calculations are on closed-packed surfaces ((111) for fcc metals and (0001) for hcp metals) and are taken from ref.[17], while CO and CH_4, calculations are on (211) surfaces and taken from refs. [18] and [19] respectively.

Even the simple framework discussed above allows one to qualitatively rationalize the utility of various materials for catalyzing different reactions. For example, the process of ammonia synthesis involves the activation of the chemically inert N-N triple bond of N_2 in the RLS, followed by the reaction of nitrogen atoms with hydrogen atoms on the catalyst surface to form ammonia.[20–23] The energy of the transition state for the dissociation of N_2, with respect to the reactant state energy, governs the intrinsic reaction rate. To stabilize this transition state and increase the intrinsic reaction rate, the process of ammonia synthesis requires very chemically reactive catalysts, i.e., materials that interact with adsorbates strongly, such as Fe or Ru. However, these materials will inherently also bind reaction intermediates strongly, and the free energy of adsorption for these intermediate

states must consequently be manipulated with operating conditions to maintain a thermodynamic driving force for their removal. This is accomplished by increasing operating temperature and thereby increasing the entropy of the gas phase products. Unlike ammonia synthesis, where the fairly inert N_2 molecule is activated, oxidation reactions require the activation of considerably weaker O-O bonds in O_2. This can be accomplished with more chemically benign materials, such as Pt and Ag, at relatively low operating temperatures.[24,25]

2.3.2 Scaling Relations

As may be expected from the Sabatier principle, a major natural barrier to the design of improved catalysts (i.e., sites that can support high reaction rates) comes from the fact that the adsorption energies of many adsorbates on solid surfaces—both stable surface species and transition states—often scale with respect to each other. Simply put, a surface that binds one adsorbate stronger than other surfaces will generally bind all adsorbates more strongly, making it difficult to independently lower an activation barrier and weaken an adsorbate bond or simultaneously enhance rates of both adsorption and desorption. The effect is illustrated in Figure 2-4(a), where the transition state energy is reduced concurrently with the binding energy of A*, lowering $\Delta H^{\ddagger}_{\text{intrinsic}}$ and increasing the intrinsic rate (TOF_{int}), but simultaneously decreasing the number of available sites $(1 - \theta_{\text{ads}})$. This natural tradeoff between intrinsic TOF and availability of active sites, due to the nature of the scaling relationships, has been shown to imply that for most reactions, catalysts that support the highest rates are those that are only

fractionally occupied by reaction intermediates under steady state catalytic conditions.[26] Efforts to circumvent the coupling of various adsorption processes may involve strategies such as specific molecular functionalization of surfaces to stabilize one species relative to another (e.g., through hydrogen bonding, which is common in enzyme catalysts), but such structures are rarely stable under the high temperature conditions typical of industrially relevant reactions.

A significant body of work has been generated regarding quantitative prediction of scaling relations between various reactive species and transition states. Beginning with work performed by Brønsted, Evans, and Polanyi in the early 20th century, experiments have shown that measured activation barriers tend to scale linearly with measured heats of reaction. This concept can be extended to elementary steps in catalytic reactions, and activation barriers have been demonstrated to vary linearly with chemisorption energies for a variety of molecules using quantum chemical density functional theory (DFT) calculations,[27–31] as is illustrated in Figure 2-4(b). In the case of stable reactive intermediates, similar computational work has shown scaling of adsorption energies. Correlations are exceptionally high for molecular species bound through the same atom (as is often the case for intermediates in a specific reaction), and in simple cases such as CH_x moieties (relevant as intermediates in methane reforming reactions), binding energies have been found to scale linearly in accordance with bond-order conservation—e.g., a metal-CH_2 bond (double bond) is roughly half as strong as a metal-C bond (quadruple bond).

2.3.3 Descriptor Based Materials Searches

Discussion thus far has focused on the key point that the strength of chemical interaction between the active site and adsorbates (stable intermediates and relevant transition states), the adsorption energy, is a descriptor of the catalytic activity. Coupled with scaling relations, the most significant consequences are that (a) there is an inherent upper limit on the possible catalytic activity of an active site, and (b) the binding energy of a single intermediate will often be an adequate descriptor of the interactions between the surface and all reactive species.[32,33] To a first approximation, activity can be optimized knowing only the binding energy of a key adsorbate and extrapolating the potential energy surface characteristics based on previously developed correlations.

We illustrate the adequacy of a single activity descriptor by way of an example in Figure 2-5, where we show the electro-chemical activity (i.e., the reaction rate) of various well-defined surfaces for the electrochemical oxygen reduction reaction (ORR), plotted as a function of the adsorption energy of hydroxyl (OH) intermediate on these surfaces. We note that the ORR involves adsorption of O_2 onto the surface of a metal electrode, accompanied by proton-electron transfer, to form an OOH intermediate in the rate-limiting step. Subsequent dissociation of OOH into O and OH, protonation of O and OH on the surface, and desorption of H_2O are effectively equilibrated.[16,34–37] The most abundant reaction intermediate under operating conditions of interest is adsorbed OH, which blocks active sites.[38–40]

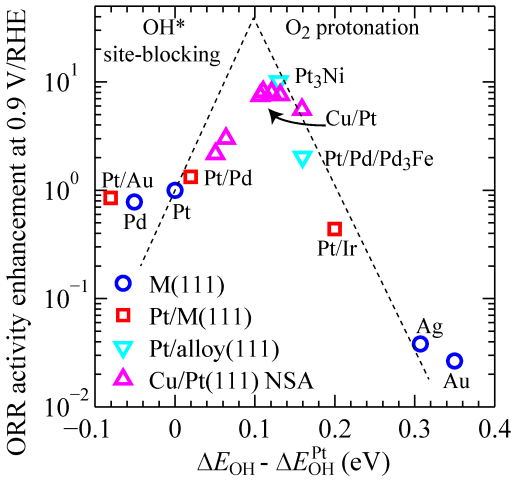

Figure 2-5: OH bond energy as a descriptor of oxygen reduction activity. Experimentally measured rate enhancement of ORR (ratio to the rate on pure Pt(111)) as a function of DFT-calculated OH binding energies on various (111) surfaces: ● different pure metal surfaces, ■ Pt monolayer on pure metal surfaces, ▼ Pt monolayer on alloy surfaces, ▲ Cu/Pt near surface alloys, characterized by varying Cu content in the first subsurface layer of a Pt(111) crystal. The OH adsorption energies are taken from refs. [35–37]. The rates were measured experimentally at 0.9 V with respect to the reversible hydrogen electrode in an acid electrolyte, and are taken from refs.[35,37]. The dashed lines represent the theoretical trend in rate enhancement assuming a simple kinetic model with limitation by either O_2 protonation (intrinsic rate) or OH removal (site blocking) as described in[35–37] and [41].

Several conclusions can be drawn from the analysis of Figure 2-5. Under a given set of operating conditions, the reaction rate exhibits a volcano-like dependence on the OH adsorption energy, with the materials to the left of the volcano peak binding adsorbates too strongly (these have highly blocked active sties), and those to the right of the volcano peak binding adsorbates too weakly (these materials are limited by their ability to activate O_2). The observed volcano relationship suggests that the adsorption energy of OH is a sufficient descriptor of catalytic activity, and a superior catalyst for ORR should bind OH by ~0.1 eV (10 kJ/mol) weaker than pure Pt—i.e., such a surface would provide an optimal

compromise between the ability to activate O_2 and the ability to avoid poisoning by the adsorbates, maximizing the rate.[35] This quantitative relationship between the OH adsorption energy and the activity of different materials for ORR is very useful since it identifies clearly the chemical characteristics of optimal catalysts for the reaction.

Having such a descriptor of catalytic activity, the important practical question is how to identify the active surface sites that bind the relevant adsorbate, such as OH in the case of ORR, with the desired binding energy. The data in Figure 2-5 show that no pure metal has the chemical properties of an optimal ORR electro-catalyst. For example, while Pt electrodes do show activity for the ORR, Pt is limited by a large adsorption energy of OH. On the other hand, its nearest neighbors in the periodic table (Pd, Ag, Au) are even further removed from the volcano maximum, and they are much less active under these conditions. Since pure metals offer only a limited number of sub-optimal catalyst choices, multi-metallic compounds—i.e., metal alloys—have received increasing attention. The main appeal of alloys is that they offer an opportunity to engineer optimal catalytic sites by fine-tuning the chemical properties of metal surface atoms through changes in their local chemical environment. Unfortunately, it is not obvious how a change in the local chemical environment of a surface site alters the strength of interaction between adsorbates and the site. For example, intuitively it might appear that mixing Pt with a more chemically benign element in the periodic table (for example, Ag) would result in an optimal material for ORR—i.e., one that binds OH with slightly lower adsorption energy than pure Pt; it has been shown, however, that this often is not the case and

more complex predictive models are required to identify optimal alloy compositions.[42–46]

2.3.4 Utility of Quantum Chemical Calculations

The most straightforward way to identify optimal alloy sites is to employ quantum chemical calculations such as DFT. While DFT calculations as implemented in most codes do not meet the chemical accuracy standard in terms of absolute values of adsorption energies, they exhibit adequate accuracy when comparing trends across similar systems. For example, in the case of ORR, the critical objective is to formulate Pt alloys with Pt surface sites that bind OH ~0.1 eV less strongly than pure Pt. DFT calculations have been used to identify many promising Pt-alloy ORR electro-catalysts. Some of these have been synthesized and experimentally confirmed to exhibit superior activity. In general, it has been found that families of alloys that exhibit the desired adsorption energies include various combinations of 3d metals with Pt, as well as core-shell materials containing Au and 3d metals in the particle core, surrounded with a thin Pt shell.[47–50] The ORR rates on some of these materials are shown in Figure 2-5.

The above-described approach, based on the identification of quantitative descriptors of catalytic activity and use of quantum chemical calculations to identify promising alloy catalysts, has been used to identify potential alloy catalysts for a number of other reactions. For example, activity trends in electrochemical hydrogen evolution are well described by H atom binding energy as a single descriptor.[51] The adsorption energy descriptor concept can also be easily extended to reactions

involving larger molecules containing more than one functional group. For example, the CO methanation reaction ($CO + 3H_2 \rightarrow CH_4 + H_2O$) and methanol decomposition to syngas ($CH_3OH \rightarrow CO + 2H_2$) involve a number of intermediates bound to the catalyst surface via C and O atoms. Using the binding energies of both C and O as activity descriptors, two-dimensional volcano plots have been constructed, identifying the optimal set of binding energies and alloy surfaces that provide the chemical environment needed to optimize activity in each case.[52–56] Finally, a descriptor-based volcano relationship can also guide cases where selectivity is the primary performance metric. For example, it has been demonstrated that oxygen binding energy is a descriptor of the selectivity of metal surfaces for ethylene epoxidation.[57,58] These studies led to the identification of Cu/Ag surface alloys and shaped Ag nanoparticles terminated by Ag(100) facets as highly selective catalysts for this reaction.[59–61]

2.3.5 Electronic Structure and Catalytic Activity

While the emergence of parallelized and computationally efficient approaches to quantum chemical calculations, capable of handling relatively large active sites, has made screening for superior catalytic materials based on critical descriptors more tractable, it is still inherently limited by a very large phase space of potential materials. For example, just considering metal alloys, the phase space is large not only due to the variety of different metals that can be mixed to form alloys, but also due to the fact that varying the concentration of these metals in the

neighborhood of the active surface site affects the value of the critical descriptor and the catalytic activity of the active site.

The process of descriptor-based screening for active catalytic sites can be dramatically accelerated if simpler but reliable models relating the chemisorption of adsorbates to the geometry of the active site are developed and employed, rather than resorting to quantum chemical calculations. For example, in the case of the ORR, the objective is to develop quantitative models relating changes in the adsorption energy of OH on Pt surface sites to changes in the local chemical environment of those sites. For these models to be of practical use in screening the immense space of possible alloy catalysts, it is desirable that they be based on easily accessible physical characteristics of the elements that form the active site.

The local electronic structure of the active site represents a natural link between the active site geometry and the adsorption energy. Hence, for many years a critical issue has been the identification of the descriptors of electronic structure that capture the chemisorption process. Efforts in this area have resulted in various models of chemisorption on metal surfaces. For example, the d-band model of chemisorption states that for a given geometry of an adsorbate on a surface site, the adsorption energy is governed by the position of the center of mass of the d electrons and holes (the d-band center) with respect to the Fermi level (highest occupied state) localized on the atoms that form the adsorption site. In general, metals with a d-band center closer to the Fermi level interact with adsorbates more strongly than those with a d-band center further below the Fermi level. This is due to the positioning of anti-bonding states of the adsorbate near the Fermi level,

causing these to be more or less populated with shifts in the d-band center. This picture of chemisorption is illustrated in Figure 2-6, and it has ben supported with a number of experimental electronic structure measurements involving x-ray emission and absorption.[32] Such models of chemisorption will not be described in detail here, as they require quite rigorous mathematical development for more than a qualitative understanding and have been reviewed in numerous articles. We note that they are a valuable starting point in understanding the chemical reactivity of a surface site in terms of a single descriptor of its electronic structure.[62–64]

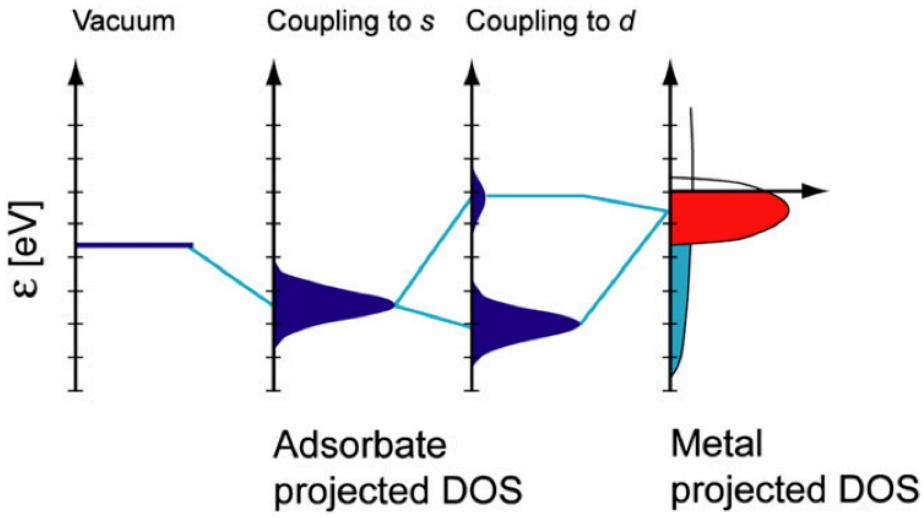

Figure 2-6: Interaction of adsorbate molecule states with a metal surface.[32] When a molecule approaches a metal catalyst surface, resonant interaction with the free s and p electrons leads to broadening of the orbital density of states. Moving closer and coupling to the localized (on the active site) d-electrons causes a classic two-level interaction, splitting the resonant state into new bonding and anti-bonding states. The anti-bonding states frequently lie near the Fermi level, and their filling with electrons often governs trends in reactivity because the sp-interaction is roughly constant across metals.

The main practical benefit of chemisorption theories like the d-band model is that the complex geometry of a surface site on a metal, i.e., the bond distances to the neighboring metal atoms and chemical composition of the local environment, is captured through one easily computed parameter that can be mapped to the adsorption energy of various adsorbates on the site. In recent years, these ideas have found their place in rapid computational screening for new catalysts. For example, a DFT-parameterized algebraic model that accounts for site geometry was recently used to estimate d-band properties of the surface sites of a large library of bimetallic surfaces. By mapping the position of the d-band center on the adsorption energy of sulfur, a number of metal alloys that exhibit improved tolerance to sulfur were identified.[65] More recently, Xin et al. developed a simple, predictive model of chemisorption on multi-metallic alloys, which showed that relative changes in adsorption energies of various adsorbates (the differences between the energy on a given surface and one that is perturbed by a change in the local environment of the active site), can be accurately and rapidly computed without the use of quantum chemical calculations. This model is essentially an augmented version of the d-band model of chemisorption, where the augmentation improves the accuracy by incorporating an additional contribution from changes in coupling strength between the adsorbate and d-band. The coupling strength has previously been shown to impact adsorption strength independently from the d-band center,[66] but several approximations were effectively implemented to estimate both of these parameters, in relative terms, with a handful of easily accessible variables: the electronegativities, atomic radii, and spatial extents of valence orbitals of the atoms

that form the active site.[67] This model was used to rapidly screen through a large phase space of Pt alloy catalysts (several thousand in minutes) and identify optimal alloys for the above-discussed electrochemical ORR.

2.4 Outlook

A great deal of progress in theoretical approaches to catalysis have been made, allowing us to inch closer to the ultimate goal of a more systematic, physically transparent design process for efficient and environmentally friendly heterogeneous catalysts and electro-catalysts. Presently, it is possible in some cases to use molecular insights regarding elementary steps, rate-determining steps, and active site geometries to identify quantifiable descriptors of catalytic activity, as we discussed for the ORR. These descriptors can then be used to identify and tailor optimal active sites. Unfortunately most reactions of interest are not understood at the level of ORR, and multiple outstanding problems face the field of catalysis.

First, there is a great deal of uncertainty regarding elementary step mechanisms in most reactions of interest. This uncertainty makes the identification of those elementary steps that affect the outcome of the catalytic reactions, and therefore the critical molecular descriptors of catalytic activity, challenging. This issue is further complicated by the fact that operating conditions (temperature and partial pressures or concentrations of reactants and products) can affect the nature of the elementary steps that control the reaction. Second, steady state catalytic processes generally take place on supported nanoparticles of active materials with a

variety of surface-site geometries. The diversity of surface sites on nanoparticles and at the nanoparticle/support interface, as well as possible adsorbate-induced restructuring of the surface at elevated temperature and pressure, makes the identification of active sites very challenging. This is even more problematic for alloys, where adsorbate-induced surface segregation of alloy elements has been reported.[68] Third, even in cases where the active surface structure and a critical descriptor of catalytic activity are known, there are difficulties in quantifying the value of the descriptor that would yield the optimal performance and difficulties identifying how to create optimal active sites. Most problems here are related on one hand to the limited accuracy of quantum chemical approaches used currently to study catalytic systems, and on the other hand to the adequacy of the schemes used to describe the kinetic interplay of elementary steps in terms of macroscopic reaction rates.

Due to these limitations, the most fruitful approaches to the identification of optimal active sites in the near future will rely on developing cohesive molecular mechanisms based on judicious combinations of multiple techniques, including kinetic measurements, quantum chemical calculations, and in-situ studies focused on characterizing surface chemistry and catalytic materials. We anticipate that the most promising routes will center on comparison of the *relative* performances of various materials and identification of families of potentially superior catalysts, as opposed to development of fully predictive models that can reproduce absolute reaction rates from first principles. Additionally, even when promising chemical structures are identified, the practicality of synthesizing such structures and

ensuring their stability under reactive conditions must be taken into consideration, although in some cases first-principles calculations have been used to address questions of stability.[69] Implementation of computationally designed catalysts will undoubtedly be tied to advances in chemical synthesis and nanotechnology to generate targeted active sites.

Even in the current nascent state of bottom-up catalyst design, the ideas discussed above are becoming useful for identifying optimal catalytic surfaces. It is also reassuring that there have been significant advances toward resolving the outstanding challenges. For example, in-situ characterization of catalytic materials with high spatial and temporal resolution is a rapidly evolving field, which will play a role in the identification and more accurate description of active sites.[70] Problems related to the accuracy of quantum chemical calculations are also being addressed by formulating more accurate functionals within the DFT framework and developing more robust and efficient algorithms for more accurate wavefunction-based approaches. Currently, the main limitations of these more accurate approaches are related to the size of systems that can be handled with such computationally demanding techniques. As these methods become more scalable, they may be integrated into other modeling techniques such as Monte Carlo simulations in order to capture the dynamics of catalytic systems.

2.5 References

1. Masel, R. I. *Chemical Kinetics and Catalysis*. (John Wiley & Sons, Inc., 2001).

2. Chorkendorff, Ib, Niemantsverdriet, J. *Concepts of modern catalysis and kinetics*. (Wiley-VCH, 2003).

3. Davis, M. E. & Davis, R. J. *Fundamentals of chemical reaction engineering*. (McGraw-Hill, 2003).

4. Fogler, H. S. *Elements of chemical reaction engineering*. (Prentice Hall, 2006).

5. McQuarrie, D. A. *Statistical Mechanics*. (University Science Books, 2000).

6. Chandler, D. *Introduction to Modern Statistical Mechanics*. (Oxford University Press, 1987).

7. Bard, A. J. & Faulkner, L. R. *Electrochemical Methods: Fundamentals and Applications*. (John Wiley & Sons, Inc., 2001).

8. Newman, J. & Thomas-Alyea, K. E. *Electrochemical Systems*. (Wiley, 2004).

9. Guggenheim, E. A. The conceptions of electrical potential difference between two phases and the individual activities of ions. *J. Phys. Chem. C* **33,** 842–849 (1929).

10. Trasatti, S. The absolute electrode potential - An explanatory note. *Pure and Applied Chemistry* **58,** 955–966 (1986).

11. Trasatti, S. The absolute electrode potential - The end of the story. *Electrochimica Acta* **35,** 269–271 (1990).

12. Llano, J. & Eriksson, L. A. First principles electrochemistry: Electrons and protons reacting as independent ions. *J. Chem. Phys.* **117,** 10193–10206 (2002).

13. Deen, W. M. *Analysis of Transport Phenomena*. (Oxford University Press, 1998).

14. Lynggaard, H., Andreasen, A., Stegelmann, C. & Stoltze, P. Analysis of simple kinetic models in heterogeneous catalysis. *Progress in Surface Science* **77,** 71–137 (2004).

15. Bligaard, T. *et al.* On the compensation effect in heterogeneous catalysis. *J. Phys. Chem. B* **107,** 9325–9331 (2003).

16. Holewinski, A. & Linic, S. Elementary Mechanisms in Electrocatalysis: Revisiting the ORR Tafel Slope. *J. Electrochem. Soc.* **159,** H864–H870 (2012).

17. Nørskov, J., Bligaard, T. & Logadottir, A. Universality in heterogeneous catalysis. *J. Catal.* **278,** 275–278 (2002).

18. Wang, S. *et al.* Universal Brønsted-Evans-Polanyi Relations for C–C, C–O, C–N, N–O, N–N, and O–O Dissociation Reactions. *Catalysis Letters* **141,** 370–373 (2010).

19. Wang, S., Petzold, V. & Tripkovic, V. Universal transition state scaling relations for (de)hydrogenation over transition metals. *Phys. Chem. Chem. Phys.* **13,** 20760–5 (2011).

20. Ertl, G. Reviews Reactions at Surfaces : From Atoms to Complexity (Nobel Lecture). *Angew. Chem. Int. Ed.* 2–14 (2008). doi:10.1002/anie.200800480

21. Honkala, K. *et al.* Ammonia synthesis from first-principles calculations. *Science* **307,** 555–558 (2005).

22. Schlögl, R. Catalytic synthesis of ammonia-a "never-ending story"? *Angew. Chem. Int. Ed.* **42,** 2004–8 (2003).

23. Boisen, A., Dahl, S., Nørskov, J. & Christensen, C. Why the optimal ammonia synthesis catalyst is not the optimal ammonia decomposition catalyst. *J. Catal.* **230,** 309–312 (2005).

24. Serafin, J. ., Liu, A. . & Seyedmonir, S. . Surface science and the silver-catalyzed epoxidation of ethylene: an industrial perspective. *J. Molecular Catalysis A: Chemical* **131,** 157–168 (1998).

25. Li, W.-X., Stampfl, C. & Scheffler, M. Why is a Noble Metal Catalytically Active? The Role of the O-Ag Interaction in the Function of Silver as an Oxidation Catalyst. *Phys. Rev. Lett.* **90,** 256102 (2003).

26. Cheng, J. & Hu, P. Theory of the Kinetics of Chemical Potentials in Heterogeneous Catalysis. *Angew. Chem. Int. Ed.* **50,** 7650–7654 (2011).

27. Abild-Pedersen, F. *et al.* Scaling Properties of Adsorption Energies for Hydrogen-Containing Molecules on Transition-Metal Surfaces. *Phys. Rev. Lett.* **99,** 16105 (2007).

28. Norskov, J. K. *et al.* Universality in heterogeneous catalysis. *J. Catal.* **209,** 275–278 (2002).

29. Bligaard, T., Nørskov, J. & Dahl, S. The Brønsted–Evans–Polanyi relation and the volcano curve in heterogeneous catalysis. *J. Catal.* **224,** 206–217 (2004).

30. Jones, G., Bligaard, T., Abild-Pedersen, F. & Norskov, J. K. Using scaling relations to understand trends in the catalytic activity of transition metals. *J. Phys. Condensed Matter* **20,** 64239 (2008).

31. Michaelides, A. *et al.* Identification of general linear relationships between activation energies and enthalpy changes for dissociation reactions at surfaces. *J. Am. Chem. Soc.* **125,** 3704–3705 (2003).

32. Nørskov, J. K., Abild-Pedersen, F., Studt, F. & Bligaard, T. Density functional theory in surface chemistry and catalysis. *Proc. Nat. Acad. Sci.* **108,** 937–43 (2011).

33. Nørskov, J. *et al.* The nature of the active site in heterogeneous metal catalysis. *Chem. Soc. Rev.* **37,** 2163–2171 (2008).

34. Greeley, J. *et al.* Alloys of platinum and early transition metals as oxygen reduction electrocatalysts. *Nature Chemistry* **1,** 552–556 (2009).

35. Stephens, I. E. L., Bondarenko, A. S., Grønbjerg, U., Rossmeisl, J. & Chorkendorff, I. Understanding the electrocatalysis of oxygen reduction on platinum and its alloys. *Energy & Environmental Science* **5,** 6744–6762 (2012).

36. Nørskov, J. K. *et al.* Origin of the overpotential for oxygen reduction at a fuel-cell cathode. *J. Phys. Chem. B* **108,** 17886–17892 (2004).

37. Viswanathan, V., Hansen, H. A., Rossmeisl, J. & Nørskov, J. K. Universality in Oxygen Reduction Electrocatalysis on Metal Surfaces. *ACS Catalysis* **2,** 1654–1660 (2012).

38. Tripković, V., Skúlason, E., Siahrostamia, S., Nørskov, J. K. & Rossmeisl, J. The Oxygen Reduction Reaction Mechanism on Pt(111) from Density Functional Theory Calculations. *Electrochimica Acta* **55,** 7975–7981 (2010).

39. Clay, C., Haq, S. & Hodgson, A. Hydrogen Bonding in Mixed OH+H2O Overlayers on Pt(111). *Phys. Rev. Lett.* **92,** 46102 (2004).

40. Bondarenko, A. S. *et al.* The Pt(111)/Electrolyte Interface under Oxygen Reduction Reaction Conditions: An Electrochemical Impedance Spectroscopy Study. *Langmuir* **27,** 2058–2066 (2011).

41. Rossmeisl Jan, Karlberg, G. S., Jaramillo, T. & Nørskov, J. K. Steady state oxygen reduction and cyclic voltammetry. *Faraday Discussions* **140,** 337–346 (2008).

42. Xin, H., Schweitzer, N., Nikolla, E. & Linic, S. Developing relationships between the local chemical reactivity of alloy catalysts and physical characteristics of constituent metal elements. *J. Chem. Phys.* **132,** 111101–111104 (2010).

43. Xin, H., Holewinski, A., Schweitzer, N., Nikolla, E. & Linic, S. Electronic Structure Engineering in Heterogeneous Catalysis: Identifying Novel Alloy Catalysts Based on Rapid Screening for Materials with Desired Electronic Properties. *Topics in Catalysis* **55,** 376–390 (2012).

44. Kitchin, J., Nørskov, J., Barteau, M. & Chen, J. Role of Strain and Ligand Effects in the Modification of the Electronic and Chemical Properties of Bimetallic Surfaces. *Phys. Rev. Lett.* **93,** 156801 (2004).

45. Xin, H. L. & Linic, S. Communications: Exceptions to the d-band model of chemisorption on metal surfaces: The dominant role of repulsion between adsorbate states and metal d-states. *J. Chem. Phys.* **132,** 221101 (2010).

46. Kitchin, J. R., Nørskov, J. K., Barteau, M. a & Chen, J. G. Modification of the surface electronic and chemical properties of Pt(111) by subsurface 3d transition metals. *J. Chem. Phys.* **120,** 10240–6 (2004).

47. Wang, C., Markovic, N. & Stamenkovic, V. Advanced Platinum Alloy Electrocatalysts for the Oxygen Reduction Reaction. *ACS Catalysis* **2,** 891–898 (2012).

48. Sasaki, K. *et al.* Core-Protected Platinum Monolayer Shell High-Stability Electrocatalysts for Fuel-Cell Cathodes. *Angew. Chem. Int. Ed.* **49,** (2010).

49. Bliznakov, S. T., Vukmirovic, M. B., Yang, L., Sutter, E. a. & Adzic, R. R. Pt Monolayer on Electrodeposited Pd Nanostructures: Advanced Cathode Catalysts for PEM Fuel Cells. *J. Electrochem. Soc.* **159,** F501–F506 (2012).

50. Gong, K., Su, D. & Adzic, R. R. Platinum-monolayer shell on AuNi(0.5)Fe nanoparticle core electrocatalyst with high activity and stability for the oxygen reduction reaction. *J. Am. Chem. Soc.* **132,** 14364–6 (2010).

51. Greeley, J., Jaramillo, T. F., Bonde, J., Chorkendorff, I. B. & Nørskov, J. K. Computational high-throughput screening of electrocatalytic materials for hydrogen evolution. *Nature Materials* **5,** 909–13 (2006).

52. Andersson, M. P. *et al.* Structure sensitivity of the methanation reaction: H2-induced CO dissociation on nickel surfaces. *J. Catal.* **255,** 6–19 (2008).

53. Andersson, M. *et al.* Toward computational screening in heterogeneous catalysis: Pareto-optimal methanation catalysts. *J. Catal.* **239,** 501–506 (2006).

54. Kandoi, S. *et al.* Prediction of Experimental Methanol Decomposition Rates on Platinum from First Principles. *Topics in Catalysis* **37,** 17–28 (2006).

55. Mehmood, F., Rankin, R. B., Greeley, J. & Curtiss, L. A. Trends in methanol decomposition on transition metal alloy clusters from scaling and Brønsted–Evans–Polanyi relationships. *Phys. Chem. Chem. Phys.* **14,** 8644–8652 (2012).

56. Studt, F. *et al.* CO hydrogenation to methanol on Cu–Ni catalysts: Theory and experiment. *J. Catal.* **293,** 51–60 (2012).

57. Linic, S. & Barteau, M. a. Formation of a stable surface oxametallacycle that produces ethylene oxide. *J. Am. Chem. Soc.* **124,** 310–7 (2002).

58. Linic, S., Piao, H., Adib, K. & Barteau, M. a. Ethylene epoxidation on Ag: identification of the crucial surface intermediate by experimental and theoretical investigation of its electronic structure. *Angew. Chem. Int. Ed.* **43,** 2918–21 (2004).

59. Linic, S., Jankowiak, J. & Barteau, M. A. Selectivity driven design of bimetallic ethylene epoxidation catalysts from first principles. *J. Catal.* **224,** 489–493 (2004).

60. Christopher, P. & Linic, S. Engineering selectivity in heterogeneous catalysis: Ag nanowires as selective ethylene epoxidation catalysts. *J. Am. Chem. Soc.* **130,** 11264–11265 (2008).

61. Christopher, P. & Linic, S. Shape- and Size-Specific Chemistry of Ag Nanostructures in Catalytic Ethylene Epoxidation. *ChemCatChem* **2,** 78–83 (2010).

62. Hammer, B. & Nørskov, J. K. Why Gold Is The Noblest Of All The Metals. *Nature* **376,** 238–240 (1995).

63. Hammer, B., Morikawa, Y. & Norskov, J. K. CO chemisorption at metal surfaces and overlayers. *Phys. Rev. Lett.* **76,** 2141–2144 (1996).

64. Hammer, B. Special sites at noble and late transition metal catalysts. *Topics in Catalysis* **37,** 3–16 (2006).

65. Inoglu, N. & Kitchin, J. R. Identification of Sulfur-Tolerant Bimetallic Surfaces Using DFT Parametrized Models and Atomistic Thermodynamics. *ACS Catalysis* **1,** 399–407 (2011).

66. Hammer, B. & Norskov, J. K. Theoretical surface science and catalysis--calculations and concepts. *Advances in Catalysis* **45,** 71–129 (2000).

67. Xin, H., Holewinski, A. & Linic, S. Predictive Structure-Reactivity Models for Rapid Screening of Pt-Based Multimetallic Electrocatalysts for the Oxygen Reduction Reaction. *ACS Catalysis* **2,** 12–16 (2012).

68. Tao, F. *et al.* Reaction-Driven Restructuring of Rh-Pd and Pt-Pd Core-Shell Nanoparticles. *Science* **322,** 932–934 (2008).

69. Greeley, J. & Norskov, J. K. Combinatorial Density Functional Theory-Based Screening of Surface Alloys for the Oxygen Reduction Reaction. *J. Phys. Chem. C* **113,** 4932–4939 (2009).

70. Zaera, F. Probing liquid/solid interfaces at the molecular level. *Chemical reviews* **112,** 2920–86 (2012).

Chapter 3: Experimental and Theoretical Methods

The work in this thesis employs numerous experimental techniques and theoretical modeling methods, many of which rely on specialized laboratory equipment and computer codes. This chapter outlines the various methods, with emphasis on their underlying scientific principles. The present aim is to develop an understanding of each method that will make clear its applicability when a particular piece of information is sought. Theoretical methods including density functional theory calculations and microkinetic modeling are discussed, followed by catalyst synthesis techniques, electrochemical characterization and performance evaluation, and atomistic characterization with various microscopies and spectroscopies. Where applicable, specific alterations or constraints relevant to the present work performed on synthesizing, characterizing, and modeling metal/alloy ORR catalysts are discussed. Experiment-specific conditions are deferred until later chapters where specific results are discussed.

3.1 Theoretical Methods

3.1.1 Microkinetic Modeling

Microkinetic modeling is a method of interpreting macroscopically observable chemical kinetics in terms of elementary reactions and surface chemistry. Kinetic data, as well as information from surface science, spectroscopy, catalyst characterization, and quantum calculations can all play a role in generating a picture of which reaction steps may be fast or slow and the nature of active sites and reactive intermediates. Using such information, one simply sets up a system of coupled rate equations (following the formalisms described in Chapter 2), and derives the rate of the overall reaction process. These models can be used to explore the sensitivity of the rate to different parameters (e.g., activation barriers, equilibrium constants, reactant concentrations, etc.) and test hypotheses regarding the nature of the elementary steps.[1–4] Ultimately one compares whether the expected rate based on a microscopic model is consistent with the macroscopically observed rate. Such models must be continually revised in light of new experimental observations and always taken with the caveat that multiple models may produce equivalent results—i.e., agreement between experiment and theory is a necessary condition, but does not suffice to confirm the uniqueness of a mechanistic hypothesis. Nonetheless microkinetic models are an indispensible tool for developing a firm understanding of elementary reaction mechanisms.

From a practical perspective, microkinetic models can often become quite cumbersome mathematically and only be solved numerically. A number of simplifying assumptions may be made in order to keep the analysis intuitive and to

permit estimation.[1,5] The primary assumptions employed in applicable cases are (i) *Steady State Approximation (SSA)*, in which transient behavior is ignored (all time derivatives are zero) and only the final rate and stable intermediate coverages and reactant/product concentrations are evaluated; (ii) *Quasi-equilibrium Approximation (QEA)*, in which one step is considered rate limiting and assigned rate constants, while all others are considered to be fast enough to maintain concentrations of participant species at an equilibrium ratio, and (iii) *Most Abundant Reactive Intermediate (MARI) Approximation*, in which it is assumed that all active sites are either free or covered with one particular surface species (e.g. adsorbed oxygen in an oxidation reaction). As always, good judgment must be used in choosing when a given model simplification is reasonable. For example, if spectroscopic evidence indicates there is only one species on a catalyst surface, the MARI approximation may be valid, but rates must also must not be extrapolated far beyond the conditions where it is known to hold.

3.1.2 *Density Functional Theory*

As described at the end of Chapter 2, quantum chemical calculations can provide a great deal of insight into catalytic mechanisms and materials design. The primary use of these techniques is to calculate the wavefunctions and energies of multi-body systems (electrons and atomic nuclei). This information can be used to predict molecular geometry, reaction energies, activation barriers, and even vibrational spectra. Density functional theory (DFT) is a particularly valuable quantum chemical calculation tool because it makes fairly large systems (on the

order of hundreds of atoms) tractable by simplifying the many-body problem, involving coupled wavefunctions for N electrons (3N variables, 4N if including spin), into a single function of spatial electron density (3 or 4 variables). The method was made possible by Hohenberg and Kohn,[6] who first showed that the electron density of a system is uniquely determined by the external potential (created by the positions of atomic nuclei), and that the energy corresponding to this density will be minimized at the ground state of the system. In other word, minimization of the energy functional computed with the density function will converge toward the ground state energy. The mathematics will not be discussed here, but the reader is referred to texts on DFT,[7,8] as well as quantum mechanics[9,10] and solid state physics[11,12] for background.

While the Hohenberg-Kohn theorems drastically reduce the magnitude of the many-body problem, they introduce difficulties in finding exact functional forms for certain contributions to the system energy. This issue was circumvented by Kohn and Sham,[13] who proposed treating the electrons in a system as non-interacting particles with the same density as the real system. The electrons have energy due to their momentum, as well as an "effective" potential energy, determined by the net classical coulombic interactions with the nuclei and electrons, and additional contributions relating to electron exchange and correlation effects. Ignoring relativistic effects (unimportant except for very heavy atoms) and making the Born-Oppenheimer approximation (due to the large mass of nuclei, their motion is negligible on the time scale of electron relaxation and thus nuclear kinetic and potential energy are treated as constant), the energy of a system may be described

by Equation (4.1), where ρ is the density, T is a kinetic energy functional, U_H is the electron-electron repulsion functional, U_{XC} is a functional describing electron exchange and correlation effects, and the final integral is the energy due to the external field imposed by atomic nuclei, which is unique to each system and given by the potential $v_{ext.}$

$$E[\rho(\vec{r})] = T[\rho(\vec{r})] + U_H[\rho(\vec{r})] + U_{XC}[\rho(\vec{r})] + \int \rho(\vec{r}) v_{ext}(\vec{r}) d\vec{r} \qquad (3.1)$$

Errors in DFT are introduced because exact density functionals do not exist for electron exchange and correlation (XC) energies. However, functionals describing these effects have been developed to a degree where the calculations often agree with experiment, particularly in predicting periodic trends. Since most of the errors are systematic, they largely cancel when computing energy differences, and reaction energies can usually be calculated accurately to within about 0.2-0.3eV (20-30kJ/mol) with the best XC functionals.[14,15] Trends across similar classes of molecules or materials are trustworthy with smaller margins of error.

In this work, DFT is used primarily to calculate the potential energy surface of reactive intermediates in various reactions. The underlying quantum mechanical calculations briefly described above are performed routinely in software packages, and in this case Dacapo, an open-source code (http://www.camd.dtu.dk) is used. Atomic nuclei are assigned positions, and the code then minimizes the energy functional to compute the ground-state energy. Forces can also be computed on the nuclei, and their positions can be iteratively adjusted to optimize molecular geometry with respect to energy as well (i.e. molecular mechanics). Despite the "black box" nature of the calculations, a number of critical choices must be made in

choosing constraints and convergence parameters for the calculations (both for accuracy and computer time). One major choice is that of orbital basis sets—i.e., orthogonal functions used to represent molecular orbitals, generally as linear combinations. These are usually based on single-atom-like atomic orbitals or plane waves. The latter are ideal for solid material and surface calculations due to mathematical simplifications in periodic systems, though they generally require the use of pseudo-potentials, which approximate the atomic nuclei and core electrons through an effective core potential. Pseudo-potentials remove difficulties in handling the sharp electron density gradients near nuclei, which otherwise require very large basis sets to fit the wavefunction. Dacapo is a pseudopotential plane wave code. It carries out most mathematical operations in reciprocal space (Fourier-Transform or k-space). The k-point mesh spacing and energy cutoff for the basis set dictate how many basis functions may be used, and hence impact the accuracy. These parameters are generally chosen to be as computationally simple as possible (e.g. large spacing and low cutoff) while ensuring the system energies converge to an acceptable accuracy (i.e., when increasing calculation accuracy no longer changes the result appreciably). The exchange and correlation functional also greatly impacts outcomes, and common options include the local density approximation (LDA) and generalized gradient approximation (GGA),[16] which express the exchange and correlation energy in terms of either the density only or the density as well as its gradient, respectively. GGA calculations are generally more accurate, and numerous variations exist even within these functionals. This work primarily uses the revised Perdew-Burke-Ernzerhof (RPBE) functional,[14] a GGA-variant which has

been shown to yield the best agreement with measured adsorption energies of small molecules on solid surfaces.

Model systems for heterogeneous catalyst calculations are most often slabs of metal atoms that are periodic in two directions to simulate an extended surface, and truncated with the desired surface facet in the third dimension. Since the calculation is periodic in 3 dimensions, a large vacuum space is included above the surface, with an artificial dipole layer included to electrostatically decouple the slabs. Such a model system is illustrated in Figure 3-1. Unit cell dimensions are chosen in the surface plane to fix the adsorbate coverage to chosen level (often to where adsorbate-adsorbate interactions are minimal). For example a 2x2 unit cell with single adsorbate atom will simulate an extended surface with ¼ monolayer of the adsorbate. In the normal direction, 3-5 atomic layers of metal are generally used so that the lowest layer(s) can be fixed in position to simulate the bulk lattice, while surface atoms and adsorbates are allowed to relax when minimizing energy. The energies of a clean slab and pure molecular species can be used as references to calculate adsorption energies (e.g. $\Delta E_{\text{adsorption}}=E_{\text{system}}-E_{\text{slab}}-E_{\text{adsorbates}}$).

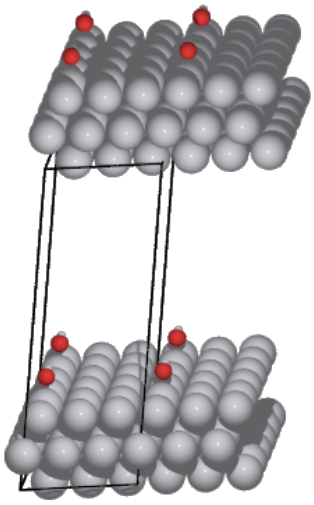

Figure 3-1: Typical DFT model system for molecule adsorption. System shows a 3x3x3 Pt slab, terminated with the [111] facet, with 1/9 monolayer adsorbed hydroxyl. The unit cell is drawn and repeated twice in all directions for clarity and illustration of the use of vacuum space in the normal direction.

3.1.3 Ab-initio Thermodynamics

DFT calculations determine the total electronic energy of a system with a constant volume (V) and number of particles (N) (a canonical ensemble in the language of statistical mechanics). Thus the energy corresponds to the Helmholtz free energy at zero Kelvin, $A(T,V,N)=E-TS$, where E is internal energy, T temperature, and S entropy. To describe molecular transformation at experimentally relevant conditions, adjustments for temperature and pressure must be made. The internal energy is composed of not only electronic, but also translational, rotational, and vibrational degrees of freedom that have temperature-dependent energy. Each must be accounted for with gaseous molecules, while for adsorbed species, translation and rotation can generally be ignored. These contributions can be computed from

appropriate partition functions, given in statistical mechanics texts,[17,18] or looked up in thermodynamic tables[19] for many simple gaseous molecules.

It is often most desirable to work with the Gibbs free energy, $G(T,p,N)=A+pV=H-TS$, (H being enthalpy) as it is an explicit function of temperature and pressure. It may be noted that electronic heat capacity is generally negligible, and the electronic entropy is only present for systems with degeneracy in the ground state (spin multiplicity) and is small at temperatures relevant to most chemical reactions (i.e. $A^{\mathrm{elec}} \approx E^{\mathrm{elec}}$). Thus a useful general expression for free energy in calculating reaction energetics from first principles is given by:

$$G = E^{\mathrm{elec}} + A^{\mathrm{trans}} + A^{\mathrm{rot}} + A^{\mathrm{vib}} + pV \tag{3.2}$$

For low temperature processes (up to a few hundred degrees Celsius), enthalpy changes are dominated by electronic and vibrational energy—rotation and translation contribute only an additional $RT/2$ per degree of freedom (0.012eV at 298K). Vibrational energy is dominated by the zero point energy, E^{ZPE} (vibrational energy present at 0 K due to quantum uncertainty), which can be computed with vibrational analysis using DFT. Thus, many reaction energies of interest are well described by Equation (3.3), where entropy may be obtained from compiled thermodynamic data for gas-phase species and assumed negligible for adsorbed species.

$$\Delta G = \Delta E_{DFT}^{elec} + \Delta E_{DFT}^{ZPE} - T\Delta S \tag{3.3}$$

Many electrochemical processes, and that studied in this work (oxygen reduction in aqueous environment) are performed near room temperature, and a maximum of ~100°C, making Equation (3.3) adequate. However, in electrochemical

systems, it is difficult to explicitly compute energies of solvated ions and excess electrons in an electrode with DFT. The simplest way to handle the thermodynamics of electrode processes in DFT is to assume equality of free energies at the experimental equilibrium potential between an ion/electron pair and a computationally accessible molecule.[20] For example the free energy of H_2 and a H^+/e^- pair at $0.0V_{NHE}$ is equivalent. Free energies may then be shifted by number of electrons in the electrode (n) times the potential difference from equilibrium: $ne(U-U_0)$, where e is the elementary charge and U is electrode potential. Field interactions with species' dipoles may also be considered but are generally negligible.[21] As such, potential-dependent free energy changes can be well approximated with Equation (3.4):

$$\Delta G = \Delta E + \Delta ZPE - T\Delta S + e(U - U_0)\Delta n \quad (3.4)$$

In this work, all reaction energies are computed with DFT, entropy changes are obtained from tabulated values (http://webbook.nist.gov/chemistry/), and zero point energies or species (ZPE) are computed or taken from prior DFT work when available (these are assumed to be similar for adsorbates across all surfaces).[20,22]

3.2 **Catalyst Synthesis**

3.2.1 General approaches

Catalysts comprise a diverse range of materials, although most contain metallic species. These usually occur in the form of either bulk metallic particles, ligated single-atom centers, or as metal oxides, sulfides, carbides, etc. Highly

dispersed, supported metallic nanoparticles are the most widely utilized category[23] (outside of biological systems), and this thesis is focused primarily on the design of metal and metal alloy materials. Thus, the synthesis of supported metals is discussed below.

Supported metal nanoparticles can either be synthesized directly on the support material, or generated as a colloidal solution and then subsequently deposited. Colloidal methods are highly flexible but often less scalable than syntheses on supports. They can generate very mono-disperse products with sharp size distributions and uniform shapes due to the option of exploiting solution-phase chemistry. Surfactants and reducing agents with specific properties often permit precise control over particle nucleation and selective growth of particular crystal facets, and they can also be manipulated to create complex multi-material architectures such as core-shell particles. Diverse structures such as nanowires, plates, and most simple polyhedra can be generated,[24] and in some cases different morphologies of the same material can exhibit drastically different catalytic activity.[25,26] Unfortunately these methods often leave behind capping agents which are difficult to remove (altering or suppressing catalytic activity),[27–29] and separation of particles from large volumes of solvent are often energy intensive, compromising scalability. On-support syntheses are significantly less controllable in most cases, but they find wide applicability in industry and many techniques can still be exploited to tailor such catalysts to have targeted properties.

The two most common on-support synthesis tehniques are impregnation and adsorption.[30] In impregnation synthesis—most often incipient wetness

impregnation—dissolved precursor salts are dripped onto a dry high-surface area support such that the solvent volume is comparable to the pore volume of the support, promoting even coating by the precursor. The impregnated support can then be dried, and the precursor salt decomposed and reduced under an appropriate gaseous atmosphere (usually H_2 and/or inert gas) at elevated temperature. Catalysts can also be calcined after reduction (heated in air to high temperature) to remove residual precursor materials, but care must be taken not to change the particle morphology in a detrimental way or to irreversibly oxidize the metals. In adsorption synthesis, electrostatic attraction between dissolved precursor ions and acid/base sites on supports is exploited. The precursor salt is dissolved and the support suspended in solution so that pH may be adjusted to protonate or deprotonate surface hydroxyl groups of the support. This method can achieve very high dispersions of metal and is most effective and controllable on oxide supports such as alumina, titania, or silica. After adsorption, standard reduction and calcination steps can be applied. Chemical reducing agents can also be used if deemed more practical (e.g. to avoid high temperature). Ultimately, the size and shape of supported particles will depend most heavily on the initial dispersion on the support and the reduction temperature.[31]

3.2.2 *Tailoring Conditions for Bimetallic and Alloy Catalysts*

As discussed in Chapter 2, multimetallic structures are a versatile class of catalysts because they allow one to fine-tune reactivity in a way that is not possible simply by moving from one element to the next across the periodic table. In cases

where an alloy between two metals is thermodynamically preferred, synthesis is often as simple as co-reducing appropriate precursor salts and annealing the product to permit interdiffusion and form a well-mixed solid solution.[32] It should be noted that the surface composition of such a bimetallic material may not necessarily reflect that of the bulk material, but surface structure can often be manipulated with exposure to particular environments during or after particle synthesis.[33,34]

In cases when the desired materials are not favored thermodynamically, it is possible to orchestrate a procedure that traps the material kinetically in a thermodynamically unstable state. It should be noted that "unstable" in the thermodynamic sense does not necessarily dictate instability under conditions in which the material will be used—for example if catalyzing a low temperature reaction. When attempting to combine two metals that do not preferentially alloy, mixing must be imposed in the precursor reduction phase, not only spatially, but also temporally. For example, one strategy to force immiscible metals to mix is to form a precursor compound that contains both metals interspersed and bridged via bonds to ligands.[32] This achieves the goal of spatial mixing, but if the reduction potentials of each metal (possibly modified depending on ligands in some precursors) are substantially different, it is likely that a reduction will occur for the more reducible species first (the one with higher redox potential), resulting in a pure phase of this species forming too rapidly and becoming segregated from the other. Any reduction of the species with the lower redox potential may also be reversed by galvanic displacement by unreacted ions of the species with higher redox potential. In such an event, it may be necessary to induce reduction rapidly

enough that the kinetics are essentially instantaneous for both species, either with very powerful chemical agents, very high temperatures, or other stimuli such as radiation.[35,36] The former will often be complicated by difficulties with mass transport of the reducing agent, while the latter risks inducing segregation by solid diffusion after the reduction.

In this work, carbon-supported nanoparticles of Ag and bimetallic Ag/M (M=Fe, Co, Ni) are explored for use as electrochemical oxygen reduction catalysts. Inspection of bulk phase diagrams for binary mixtures of Ag and the 3d-transition metals reveals that the solubility of these species in Ag is a fraction of a percent in all cases.[37–39] Large differences in redox potentials, melting points, and lattice constants for the pure species, summarized in Table 4-1, each provide challenges to synthesizing alloys, as discussed above. In addition, constraints such as incompatibility of certain solvents with reducing agents (e.g., many reducing agents strong enough to reduce 3d metals react with water or can only be stabilized at high pH where the metal precursors are not soluble) and side reactions such as AgCl precipitation from common 3d-metal precursors (e.g. $CoCl_2$, $FeCl_3$) further restrict the number of viable synthesis approaches to explore.

Property	Ag	Ni	Co	Fe	Issue
Redox Potential	0.80 V	-0.26 V	-0.28 V	-0.44 V	Kinetics & Galvanic Rxns.
Melting point	962°C	1455°C	1495°C	1538°C	Thermal Segregation
FCC Lattice Const.	4.09	3.52	3.55	3.45	Stability (Thermodynamic)

Table 3-1 Physical properties of Ag and 3d transition metals contributing to incompatibility in alloy synthesis.

To circumvent these issues, a modified incipient-wetness technique, adapted from concepts in several works, was employed.[32,40–42] Ordered, bimetallic precursor salts were precipitated onto a graphitic carbon support to create nanoparticles with atomic-scale mixing of the two metals. Reduction was carried out with very rapid heating and cooling to minimize thermal segregation and lessen differences between the rates of each of the metals' reductions. More specifically, the water-soluble precursors $K_3[Co(CN)_6]$, $K_4[Fe(CN)_6]$, or $K_2[Ni(CN)_4]$, and $AgNO_3$ were added to Vulcan XC72 carbon support, forming insoluble salts $Ag_x[M(CN)_y]$. Unprecipitated material could be washed away, leaving behind an almost pure phase of bimetallic nanoparticles. The bimetallic salt particles were then introduced into a preheated furnace at high temperature under dilute hydrogen and then quenched. Various characterization techniques, discussed below with specific results deferred until the appropriate chapters, showed that the method cannot produce complete bulk alloying, but can be optimized to isolate enough of the 3d metals in the near-surface region of Ag to modify its activity. The rapid heating was found to be critical to achieving this surface alloying, as slowly heated samples exhibited minimal activity enhancements.

3.3 Electrochemical Measurements

3.3.1 Voltammetry

Electrochemical measurements are generally centered on measuring the relationships between current, potential, and time at a working electrode. The

majority of routine analysis involves measuring one of these variables as a function of another. These can be performed with a potentiostatic or galvanostatic circuit, and modern measurement devices are described further below. The techniques are somewhat self-explanatory—for example, measuring current over time at a fixed potential (potentiostatic) is called 'chronoamperometry', while the fixed-current (galvanostatic) version would be 'chronopotentiometry.' Current may be integrated to measure total charge transfer, begetting 'coulometry,' and finally, the time derivative of potential may be fixed, which is just termed 'voltammetry.' Voltammetry may be performed as a simple linear sweep, or cyclically to determine hysteretic effects moving from high to low vs. low to high potentials (or to monitor the products formed during the initial sweep). A final technique, applicable for AC current/potential signals is known as electrochemical impedance spectroscopy (EIS), whereby the complex impedance (a function of both the magnitude and phase shift of electrode output relative to signal input) is measured as a function of the input frequency. This technique involves interpreting an electrochemical system's behavior in terms of an 'equivalent circuit,' and theoretical treatment would require extensive discussion that goes beyond the scope of this work. In this work EIS is used only for measuring the uncompensated resistance of electrochemical cells (discussed further below), and will not be elaborated upon.

The work in this thesis primarily uses linear-sweep and cyclic voltammetry to characterize electrocatalysts and measure their activity. Catalyst surface areas for Ag-based materials (deposited on an inert but electronically conductive substrate) were measured use stripping voltammetry, in which a probe species (Pb in this

case) was deposited as a monolayer on the Ag surface at a specified constant potential (well established in prior work) and then potential was swept in the oxidizing direction to perform coulometry and determine the amount of Pb removed (and hence Ag surface area).[43,44] To ensure that the measured current comes only from Pb stripping, the solution was first purged with inert gas to avoid stray currents from oxygen reduction, and the baseline current, due to double-layer capacitance, is subtracted. The process is depicted in Figure 3-2. Pt catalyst areas were measured in a similar manner using deposition of hydrogen atoms from water, which also form an ordered layer at potentials above the full reduction potential (i.e. $H^+ + e^- \rightarrow H^*$ occurs before $H^+ + e^- \rightarrow H_2$). This deposition process is rapid enough that a cyclic voltammetry (CV) scan can be used in the solution and the appropriate current peaks integrated.[45] A typical CV measurement of a platinum electrode in acid is also shown in Figure 3-2, along with the current measured at the same potentials in the presence of O_2. Performing CV in the electrolyte solution is also useful for characterizing a variety of other surface phenomena on electro-catalysts, such as the adsorption of auxiliary species that may influence activity. This is evident from the Pt voltammogram at higher potential, where it can be seen that surface oxidation begins to set in at higher potentials, first as OH, and eventually as PtO layers.

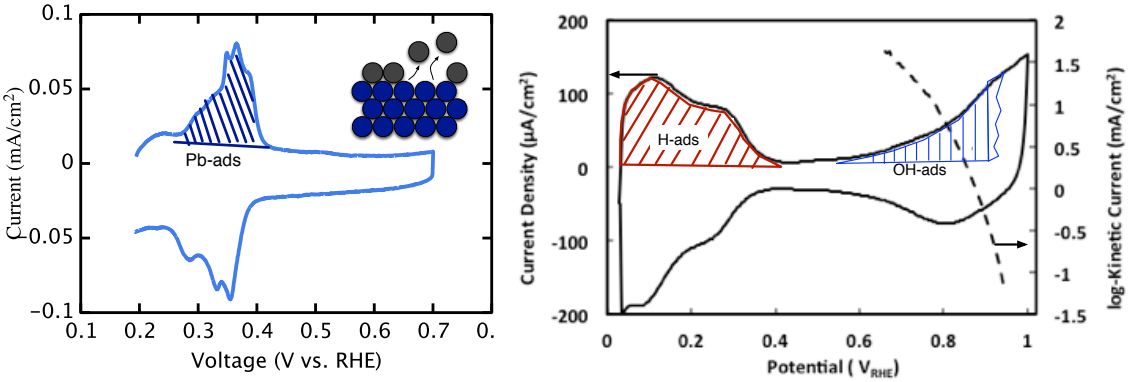

Figure 3-2: Representative data from voltammetry experiments. *Left:* Pb-stripping voltammogram for measuring Ag surface area. Polycrystalline Ag yields ~280μC/cm^2. (Conditions: Ar-purged 0.1M NaOH + 0.125mM $Pb(NO_3)_2$, 30s deposition and 10mV/s scan). *Right:* Cyclic voltammogram of Pt electrode in Ar-purged 0.1M $HClO_4$ at 50mV/s (left axis), and ORR kinetic current in O_2-saturated 0.1M $HClO_4$ at 10mV/s scan rate (right axis).

For oxygen reduction reaction (ORR) activity measurements, the electrochemical cell is saturated with O_2, and potentials are swept through a voltage range between the O_2/H_2O equilibrium potential and a large overpotential that would correspond to short-circuit conditions in an H_2/O_2 fuel cell. Higher current at smaller overpotential indicates improved catalytic activity, in accordance with the kinetic equations described in Chapter 2. Because the O_2 is fairly dilute in water (saturation is roughly 1mM at 1atm O_2), convection must often be induced in order to increase mass transport rates to a level where kinetics can be measured. The rotating disk electrode (RDE) method was used to achieve this. RDE is a common tool and its analysis is described in more detail below.

3.3.2 The Rotating Disk Electrode

Electrical polarization of an electrode surface and the reaction of active species in its vicinity naturally leads to depletion of these species at the electrode surface. Depending on the electrode geometry and mass-transport characteristics of the surrounding electrolyte, it may be possible to reach a steady state, or the domain of depletion may continuously grow with a corresponding decay in reaction rate over time. In order to achieve rates that are steady, governed by kinetics, and also large enough in magnitude to reproducibly measure, it is necessary in some cases to induce convection to the electrode surface. This is generally the case for reactions involving dissolved gaseous species, such as O_2 in the ORR. It should be noted that in applications such as ORR in fuel cells, very high transport rates can be achieved in gas-diffusion electrodes. Thus forced convection in a simple electrochemical cell is not unrealistic, but simply a useful way to study the reaction in isolation in a well-defined system.

In the RDE method, the working electrode is a disk embedded in a larger cylindrical housing of non-conductive material. This disk and housing are then rotated, drawing fluid upward toward the disk, with increasing radial velocity and decreasing axial velocity as it approaches the surface, effectively creating a thin boundary layer in which diffusion can occur very rapidly (it is assumed that the convection maintains the bulk concentration of reactive species near the boundary). The general operating principle is depicted in Figure 3-3. Using the velocity profile of the fluid and the convective-diffusion mass transport equations,[46] the maximum diffusive flux to the disk can be computed, and is described by the Levich Equation:

$$i_L = 0.62nFAD^{2/3}\nu^{-1/6}C^*\omega^{1/2} \tag{3.5}$$

Above, i_L is the limiting current, n the number of transferred electrons, F Faraday's constant, A electrode area, D diffusivity of reactant in the electrolyte solution, ν the kinematic viscosity of the electrolyte, C^* the bulk concentration of the reactant, and ω the electrode rotation frequency (in rad/s). One can effectively view the process as linear diffusion through a layer of thickness $\delta \sim 1.61D^{1/3}\nu^{1/6}\omega^{-1/2}$.

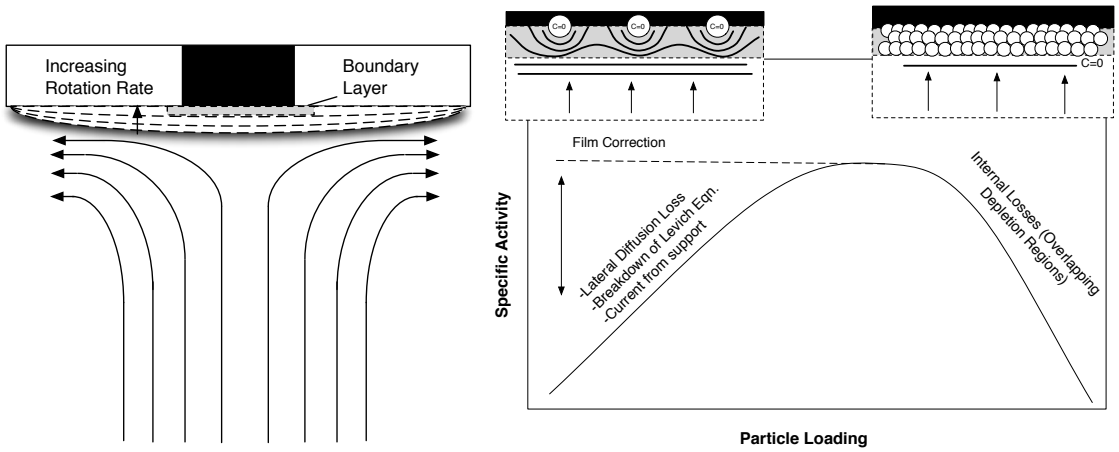

Figure 3-3: Rotating disk electrode operating principle and behavior with catalyst particle active layers. *Left:* Schematic of RDE apparatus and flow pattern *Right:* Qualitative relationship between measured specific-activity of a catalyst particle layer and catalyst loading on an RDE.

In this work, carbon-supported catalyst particles are deposited on an RDE in a thin film, approximating the flat disk behavior described by the Levich equation. In this method, care must be taken that the loading of catalyst particles is in the correct regime—if loading is too low, substantial regions of the disk will be inert and reactants may be required to diffuse far laterally and increase the transport resistance; if loading is too high, depletion of reactant around individual particles will lead to underutilization of the active surface area due to internal transport

losses and also obscure the specific activity of the catalyst. These factors are illustrated in Figure 3-3. Corrections may be made for these effects (such as treating the losses as diffusion through a second boundary layer of low diffusivity), but it is most effective to vary the loading and find where the kinetic currents (elaborated upon below) are linear with particle area. A good rule of thumb is to aim for particle surface area on the same order as the macroscopic area of the disk.

The critical reason for identifying the maximum mass-transfer-limited current at the RDE is that the overall process of diffusion to the electrode surface followed by reaction may be viewed as two resistive processes in series. In other words, the effective resistance to mass transport and the resistance to the charge transfer reaction (R=V/i in each case) may be added. This is the basis of the the Koutecky-Levich equation:

$$\frac{1}{|i|} = \frac{1}{|i_L|} + \frac{1}{|i_k|} = \frac{1}{\left|0.62nFAD^{2/3}\nu^{-1/6}C^*\omega^{1/2}\right|} + \frac{1}{|i_k|} \tag{3.6}$$

The Koutecky-Levich equation may be used solve for the kinetic current at a given potential in the absence of mass transfer resistance. This allows direct evaluation of the catalytic properties of the electrode material. In practice the limiting current may be determined as the plateau in current at low overpotential, making the analysis quite simple from an *i* vs. *E* data set (the resulting kinetic current for a typical ORR experiment was shown in Figure 3-2). A Koutecky-Levich plot—inverse current density ($1/j$) vs. inverse square-root rotation rate ($\omega^{1/2}$)—can also be generated, and is useful in measuring parameters such as the number of electrons transferred (e.g. when selectivity to parallel reactions may occur), or the mass-transfer properties of the system (via the slope of the plot). The intercept ($\omega \rightarrow \infty$

limit) also yields the kinetic current at the potential of interest. Typical RDE current-potential curves and a corresponding Koutecky-Levich plot are shown in Figure 3-4.

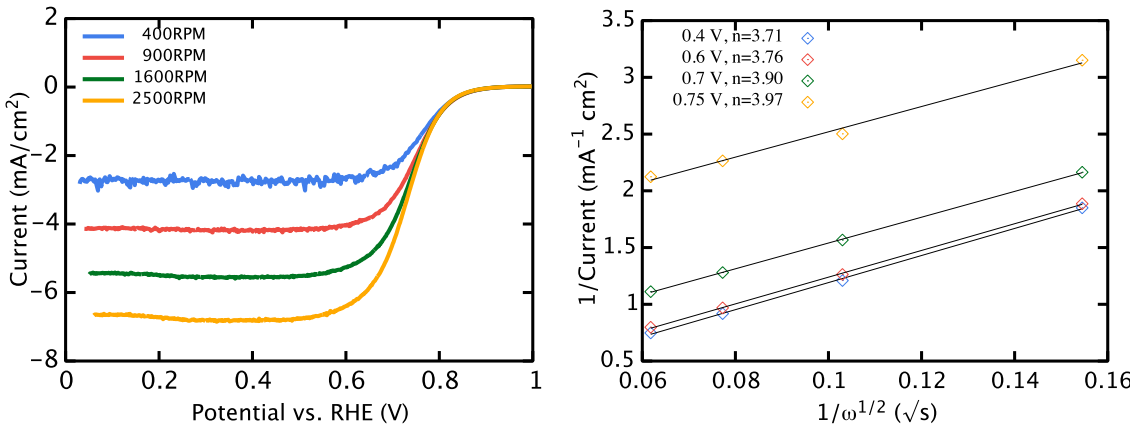

Figure 3-4: Representative RDE polarization curves and Koutecky-Levich plots. *Left:* Current-potential relationship for O_2 reduction at an Ag RDE electrode at different rotation rates. *Right*: Corresponding Koutecky-Levich plot showing average number of electrons transferred (a proxy for selectivity of H_2O ($4e^-$) vs. H_2O_2 ($2e^-$)), computed from the slope and properties of O_2 in 0.1M NaOH: D=1.93x10^{-5} cm^2/s, υ=1.09x10^{-2} cm^2/s, and C=1.26x10^{-3} mol/L.[47]

3.3.3 Potentiostats

The various techniques described above can generally be performed by commercially available electrochemical workstations, or 'potentiostats,' which actually house potentiostatic/galvanostatic/frequency-response-analysis circuitry. The inner workings of the potentiostat are not critical to understanding electrochemical reactions, but a few basic characteristics should be noted. The main operating principle of the potentiostat is comparison the potential of a working

electrode to that of a stable reference electrode, and using this difference to control a feedback loop, which controls a 'compliance voltage' (electrically isolated) to an auxiliary electrode (counter electrode).[46,48] Current flows between the working electrode (WE) and counter electrode (CE), and by controlling the CE/WE current with the compliance voltage, the WE potential relative to the reference electrode (RE) can be fixed without polarizing (passing current through) the RE, which would change its potential. A typical experimental setup is depicted in Figure 3-5. In general, potentiostats can perform rapid, accurate measurements over a wide range of currents and potentials. Typically stable states can be reached in microseconds with potential accuracy errors on the order of microvolts, with tradeoffs between control speed and accuracy (noise), as is common in most instruments.

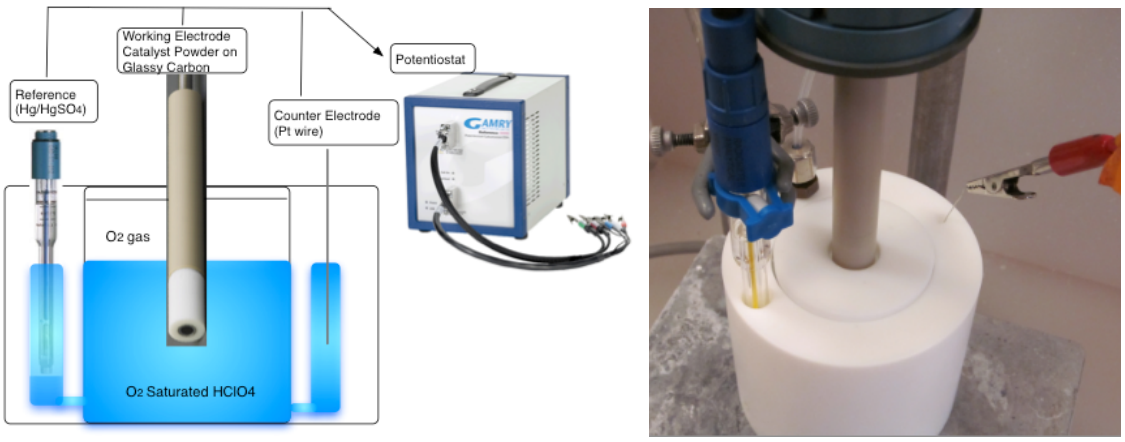

Figure 3-5: Electrochemical Measurement Setup. Schematic and photograph illustrating the 3-electrode setup with an RDE working electrode.

Accuracy and stability can often be enhanced by forcing the instrument to use a particular measurement resistor in the WE/CE current path, in accordance with Ohm's law ($V=iR$), such that easily measurable voltage differences are present (e.g., if attempting to measure 1μA level currents, the measurement resistor should be near 1MΩ to produce an easily measured 1V signal). If signal noise appears to be present as specific frequencies, (e.g., 60Hz from poorly shielded power supplies or other frequencies from stray RF), band-pass filters can often be utilized (within the instrument and software) to remove these, but care must be taken not to obstruct signal from the system. Cell capacitance, caused both by ionic double layer formation at charged electrodes and other factors such as very long lead cables, can also often cause oscillatory behavior due to phase shifts from the capacitive charging. This is problematic for rapid and high-frequency measurements, as well as pseudo-steady-state measurements when the control circuitry attempts to respond too quickly to changes. Various internal settings may be adjusted to slow down the control amplifier, and adding a high-frequency shunt around the cell to bypass feedback may also be useful[48]. In this work, oxygen reduction currents are generally high enough that these issues were not present, but in doing very low current voltammetry, for example stripping voltammetry to measure surface areas, high frequency AC filtering was necessary.

3.3.4 Electrochemical Cell Design

Electrochemical cells for performing voltammetry etc. in essence consist of three electrodes—working, counter, and reference—in contact with the same electrolyte solution. However, it is rarely reliable to simply place the three into a beaker and begin taking measurements. One major issue that must be accounted for is that of uncompensated resistance. While a potentiostat's internal circuitry is well-characterized and ohmic losses and phase shifts corrected, the resistance of the electrolyte solution leads to a discrepancy between the measured potential of the working electrode and its true potential—an effect exacerbated at higher currents where the Ohmic loss is largest. If one imagines the equipotential surfaces between a WE and CE, illustrated in Figure 3-6 for a simple linear geometry, it becomes clear that placing a reference electrode some distance away from the WE surface means that it will be in contact with solution that is at a lower potential than the WE.[49] Unfortunately, most REs are relatively large and would obstruct the flow of current and reactants to the WE if placed immediately at the surface. This can be overcome by utilizing a small capillary tube with a pathway leading to the RE. The tube is made of an insulator and thus the equipotential line at the tip, which is open, will determine the potential inside the capillary, up to the RE surface. There will still be some uncompensated resistance between the WE and capillary tip, but this is usually small enough to measure and safely apply a small correction to the potential data.

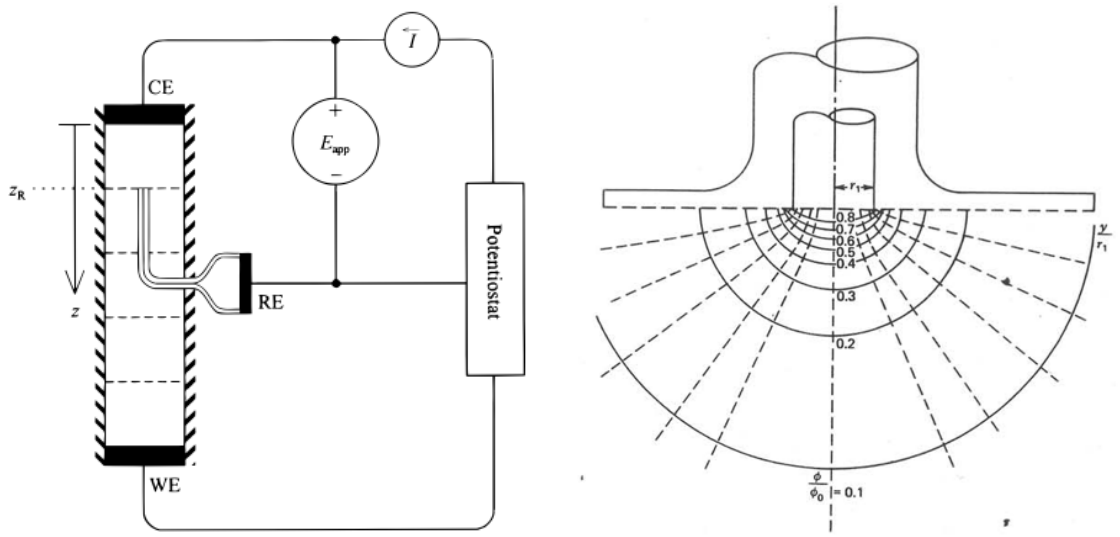

Figure 3-6: Equipotential surfaces and reference electrode placement. *Left:* Simplified electrochemical cell with equipotentials (dotted lines) between working and counter electrodes shown.[49] Reference electrode contact nearer to the WE surface reduces the discrepancy between measured and true potential caused by solution resistance. *Right:* Equipotentials at an RDE surface, showing the difficulty in reducing discrepancy due to rapid potential drop-off.[46]

Figure 3-6 also shows the potential distribution about a disk electrode (in the limit of complete kinetic control), and it can be seen that the potential drops off fairly rapidly with distance. Thus, significant compensation with a capillary is quite difficult, and one must settle for the sub-optimal method of applying a rather large correction. The uncompensated resistance is most easily measured with impedance spectroscopy in the limit of very high frequency. With very rapid voltage oscillation, reactions and capacitive charging do not contribute to impedance because they are too slow, and the solution resistance is the main component of the impedance. This work uses relatively conductive electrolytes to minimize solution resistance, and measured uncompensated losses with EIS in the 10kHz-1MHz range to determine the level of correction necessary.

In addition to electrode placement, cleanliness is of the utmost importance in electrochemical measurements. Trace quantities of foreign species can easily generate stray currents and obscure data. Aqueous solutions generally require ultrapure water (18.2MΩ) and electrolyte salts, acids, bases, etc should be of high purity. Along the same lines, the reference electrode, which often contains its own internal electrolyte solution, should be compatible with the primary electrolyte. Solution exchange is kept to a minimum with low-porosity frits, but ultimately ionic contact between the RE and main solution is a necessity (the RE is not polarized in principle, but must flow a small current in practice (pA scale) for measurements). Contamination of the working solution can be avoided if the electrolytes are identical, or made negligible if the species present cannot affect the reaction (e.g. poisoning the WE surface). Additionally, it is beneficial to provide a long diffusion path of stagnant electrolyte to keep RE species away from the working solution for the duration of tests (partially already accomplished with use of a capillary). Similarly, the CE may produce contaminant species when it is polarized, as voltage is applied indiscriminately by the potentiostat to achieve the desired current and every half-reaction at the WE must be accompanied by a corresponding reaction at the CE to maintain electroneutrality. Isolating the CE with a long diffusion path and/or frit is thus helpful. Finally, in some cases, the working electrode may only be stable in the electrolyte while under potential control. When it is imperative to control the potential of an electrode prior to contact with the cell and during immersion, a fourth electrode can be utilized—an inert dummy WE. Its placement is not crucial, but it is clipped to the WE potentiostat lead and held in solution while

the WE is immersed. It can then be removed without breaking electric contact in the system.

This work primarily uses aqueous cells in acid or base. In basic electrolyte, and Hg/HgO RE with 1M KOH internal solution is used, while in acid an Hg/Hg_2SO_4 element in saturated K_2SO_4 is used. When $HClO_4$ electrolyte is used, rather than H_2SO_4, the RE is separated by a second frit with K_2SO_4 bridging solution. No capillary is implemented in the cell design (Figure 3-5), but electrolytes were highly conductive and uncompensated resistance measurements generally were around 40 Ohm, meaning with maximum ~1mA currents, potentials were extrapolated at most 40mV. Catalyst kinetic currents were much smaller and not substantially influence by the uncompensated resistance.

3.4 Microscopy and Spectroscopy

3.4.1 X-Ray Diffraction

X-ray diffraction (XRD) crystallography is a technique that utilizes the elastic scattering of x-rays by crystalline materials to deduce the structure of the crystal lattice. Essentially, a sample is irradiated by an x-ray source, while a detector is moved radially around the sample (or alternatively the sample is rotated) to measured the angle of the scattered waves. The main operating principle is that regular periodic planes of atoms will generate constructive interference of scattered incident waves at specific angles. The Bragg equation,[50] given below, describes the

relationship between this angle, θ, the plane spacing, d, and the wavelength of the incident light, λ:

$$2d \cdot \sin(\theta) = n\lambda \tag{3.7}$$

The Bragg equation essentially states that along the coherent scattering angle, the lattice planes are separated by an integral number (n) of wavelengths. X-ray wavelengths happen to be on the same order of magnitude as interatomic spacings, and hence are utilized in this technique.

Each set of parallel planes in a given crystal will contribute to the scattered signal, and the exact spacing for each plane (and hence scattering angle) will depend on the crystal system and lattice parameter—these are compiled in various sources and can be worked out from basic geometry.[11,50] It should be noted that because XRD is based on elastic scattering, the signal comes from the bulk of the material. However, smaller crystals with fewer contributing planes will exhibit broader scattering peaks in comparison to large crystals. This effect was treated theoretically by Scherrer, who showed that the average crystallite size in the sample can be well estimated with Equation (3.8), where β is the width at half max of the signal peak:

$$d_c = 0.9\lambda/\beta\cos(\theta) \tag{3.8}$$

The relative intensities of XRD signals depend, foremost, on the identities and locations of the actual atoms in the lattice. The full theoretical prediction of spectra will not be discussed here, as this technique is only used here for simple material identification and plane spacing estimates. Databases exist with diffraction patterns for most known crystalline solids, and much of modern analysis simply requires a

rough idea of the species that could potentially be present and comparison to diffraction patterns in the database. XRD measurements in this work were conducted in a Rigaku rotating anode diffractometer with a monochromated CuKα x-ray source, and the Jade software package database was used to confirm the spectra produced by various samples.

3.4.2 TEM/STEM

Transmission electron microscopy (TEM) is a valuable technique for the direct visualization of materials down to the atomic scale. Features on this length scale, which are not accessible to visible light microscopy, are distinguishable due to the small wavelength of the electron. The technique essentially relies on irradiating thin samples with a high-energy electron beam (usually produced by application of a large voltage to a sharp metal tip causing field emission), which is focused through various electromagnetic lenses to produce an image. In standard TEM mode, the instrument is set to produce a broad parallel beam of electrons, which scatter off of atoms in the sample, decreasing the beam brightness in those areas and projecting an image onto a fluorescent viewing screen or CCD camera for electronic acquisition. A basic diagram of the operating principle is provided in Figure 3-7. This configuration is useful for both imaging and collecting diffraction patterns (diffraction involves changing the optics to place the focal plane, where rays from the same angle focus to a point, on the detector rather than the image plane). In contrast, the electron beam also may be focused to a point and rastered across the

sample, with a detector counting scattering electrons at each point in serial. This is a basis of scanning TEM (STEM), and is also depicted in Figure 3-7.

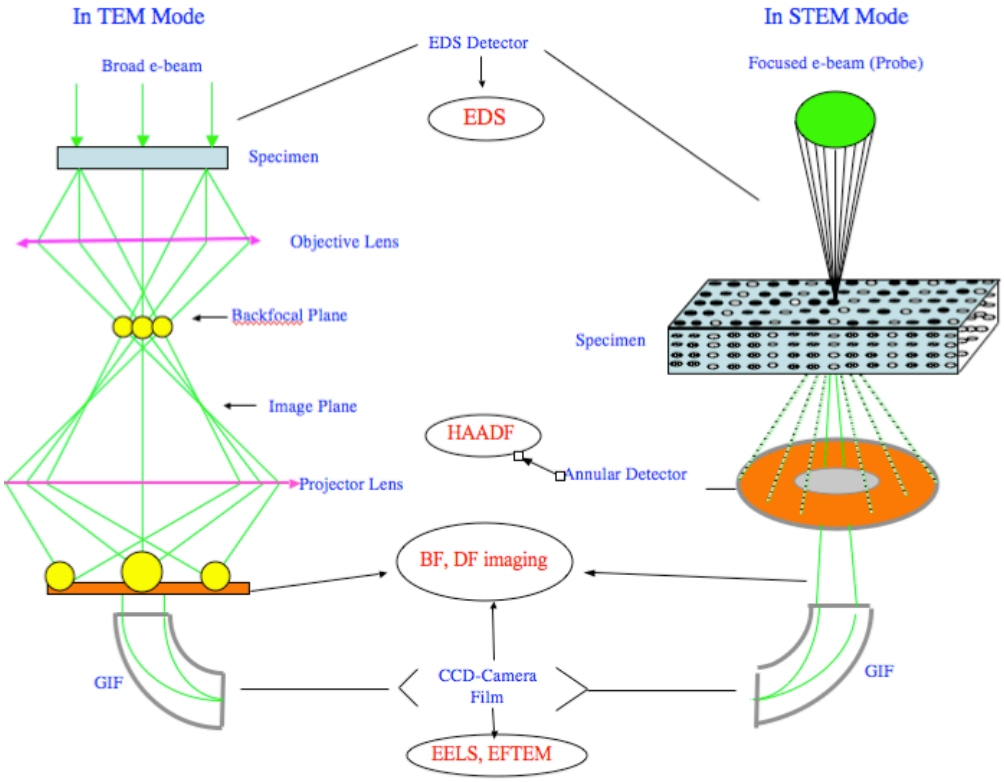

Figure 3-7: Standard and scanning transmison electron microscopy.[51] TEM collects images in parallel, STEM in serial. STEM permits high spatial resolution of spectroscopic signals.

An STEM has the added benefit of using the electron beam as a spatially localized spectroscopic probe. Figure 3-8 contains a schematic of the various photonic and electronic signals that emanate from a sample after absorption or scattering of an incident electron beam. Elastically scattered electrons can provide chemical information about individual atoms due to the fact that heavier nuclei cause scattering to higher angles. A wide annular detector (see Figure 3-7) can then

be used to produce so-called dark-field images (produced without the direct beam) with image contrast directly related to the mass of the atom(s) being imaged. Inelastic interactions with the sample are also of particular interest for chemical and electronic characterization, and these form two of the most widely utilized spectroscopic techniques performed in a TEM: energy dispersive x-ray spectroscopy (EDS) and electron energy loss spectroscopy (EELS), which are discussed in the next sections.

One practical aspect of STEM that should be noted is that the quantity of signal produced is proportional to the intensity of the electron beam striking a sample, while the spatial resolution is limited by the diameter of the probe.[52] In order to improve spatial resolution, it often becomes necessary to insert various beam-limiting apertures to assist in collimating the beam by blocking electrons that do not follow the idealized path through the microscope column. This inherently throws away potential signal. The biggest contribution to nonideality in the beam is spherical aberration in traditional electromagnetic lenses, which essentially causes electrons that are far from the optic axis to be bent to larger-than-necessary angles when the electrons nearer to the axis are correctly focused to a point.[52] In the past decade, however, commercial aberration-correction systems have become available (these were actually limited by computational power rather than theory), and in an aberration-corrected STEM, significantly higher signals and resolutions can be achieved (over an order of magnitude).[53,54] Of course, higher intensity also must be balanced with issues such as sample damage and contamination effects from cracking adsorbed organic species or stray hydrocarbons in the TEM column (which

is maintained at high vacuum). This work is focused on characterizing metallic materials, which do not suffer beam damage very rapidly. However, contamination is a frequent issue and was minimized by pre-heating samples in an inert atmosphere (Argon at ~200°C) to remove most residual species left after synthesis or introduced by the sample substrate or lab atmosphere at large.

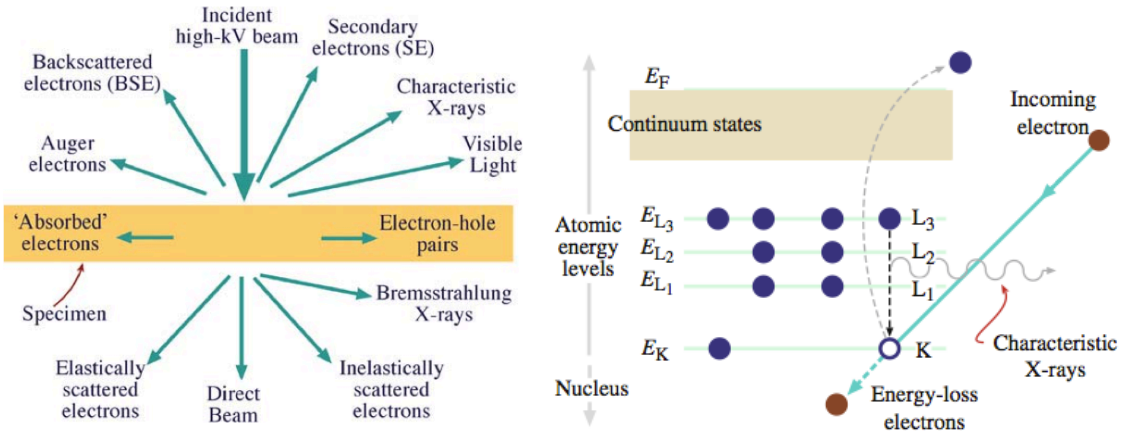

Figure 3-8: Signals produced by interaction of an electron beam with a sample.[52] The beam electrons can scatter elastically and inelastically off of a sample, leading to various trajectories for different types of scattering event, as well as photon emission events.

3.4.3 *Energy Dispersive X-ray Spectroscopy (EDS)*

Referring back to Figure 3-8, one can see that ionizations cause by adsorption of energy from an electron beam can result in x-ray fluorescence. The emitted x-rays occur at fixed characteristic energies, which are associated with the available electronic transitions in the excited atom. Thus, measurement of x-ray energy from a local point in a sample can yield information about its chemical composition. Fluoresced x-rays are emitted in all directions (spherically symmetric), and thus the acquirable signal in EDS is dictated by the solid angle subtended by the

detector about the sample. This is generally only a few mrad due to spatial constraints in TEMs, and significant time can thus be required to accumulate enough counts for reliable spectra—particularly if one wishes to generate an elemental map using spectra at many points.

The most common EDS detectors are comprised of a thick layer of silicon, with extremely thin Au electrodes on either side. Incident x-rays generate electron hole pairs in the Si, which are then collected by the electrodes with the measured current corresponding to the x-ray energy (more energy excites more electrons).[52] As such, EDS cannot detect very light elements (nothing lighter than carbon) because their characteristic x-rays are insufficient to excite the Si detector. The detection method also limits the energy resolution of EDS to about 0.1keV, which means that elements can be identified, but no fine electronic-structure is distinguishable, and in some cases it may be difficult to resolve certain elements' signals (specialized detection equipment does exist for high resolution, but is not implemented in most practical or commercialized setups). EDS is most useful for compositional analysis, and with care can be performed quantitatively, to sub-nm resolution with a stable enough instrument and sample.

It should be noted that care must be taken in assigning the presence of particular elements, as spurious x-rays can be generated by post-specimen scattered electrons or by plural fluorescence (i.e., an x-ray causing a second excitation and inducing fluorescence in another atom). Cu-signals are frequently seen in spectra due to the presence of this element in many TEM components; x-ray addition can occur if two photons enter the detector simultaneously; and 'escape peaks,' caused

by secondary fluorescence in the Si detector itself (appearing at ~1.74 keV negative of a true peak), can also appear. It is thus best to identify elements by multiple peaks if possible—these often occur in well-defined ratios. Judicious choices of materials can also alleviate spurious effects. For example, if a sample must be dispersed on a thin film (e.g. polymer or graphite substrate for depositing nanoparticle suspensions), the film support grid (a metal) can be chosen not to interfere with the elements being analyzed. EDS-tailored sample holders are also available and contain an x-ray transparent beryllium stage.

3.4.4 Electron Energy Loss Spectroscopy (EELS)

Complimentary to EDS is EELS, which measures the energy of electrons after they have interacted with the sample. While EDS is best suited for analysis of heavy elements with high-energy x-ray emission, EELS is ideal for light elements. More specifically, it can detect inelastic events with energies below ~2000eV, which roughly coincides with the lower limit of EDS. This is not to say, however, that heavy elements are undetectable—many elements possess weakly bound electrons in higher orbitals than those probed by EDS. Generally EELS is amenable to probing all elements through the 4^{th} row of the periodic table (and higher with very sensitive equipment and good analysis).

EELS detection involves collecting the electron beam after it exits the sample and passing it through a magnetic prism, which disperses the electrons by energy (they follow different radii of curvature through the prism), after which they are collected on a CCD camera to generate the energy loss spectrum.[52] A schematic of

the filtering system was shown at the bottom of Figure 3-7. Generally, an aperture is placed above the prism so that only forward-scattered electrons are collected. This is because typical semi-angles associated with low-energy scattering events are on the order of $\theta \sim E/2E_0$, where E is the scattering event energy and E_0 is the beam energy—in other words a 2000eV ionization by a 200keV beam will only cause the electron to deviate an average of 5mrad.[55] Wide collection angles open the door to collecting multiply-scattered electrons, which complicate spectra interpretation. The beam itself roughly exhibits a Gaussian energy distribution, and hence 'good' spectra will generally look like a decaying exponential background with well-defined peaks at characteristic energies. Because forward-scattered electrons are collected, signals in EELS are actually quite strong, and it is entirely possible to collect individual atomic spectra with an aberration corrected microscope (and a good sample).

Typical energy resolutions in EELS are about 1eV (better with beam monochromation), and thus EELS can detect very low energy events, such as plasmon excitation (physical oscillation of electrons), and also probe the fine-electronic structure (density of states, DOS) of a material. Specifically, the DOS above the Fermi level will be proportional to the probability an electron is ionized to a particular energy within a band (broadened collection of energy states associated with a particular orbital, such as metal d-states).[56,57] Such analysis is often referred to as EELS near edge structure or ELNES.

Ideal samples for EELS are very thin (generally < 10-20nm) so as to minimize the occurrence of multiple scattering events (the longer the electron spends in the

sample the more likely it is to participate in one or more events). For example, a metal film with sharp ionization peaks can have these peaks broadened and lose fine structure due to convolution with plasmon excitation if both events occur. Elastic events following an energy-loss event can also lead to sacrifice of signal because these electrons simply scatter out of the collection path. Keeping the collection angle low helps to restrict spectra to singly-scattered electrons, but as always this comes at the expense of signal counts. For samples that cannot be mechanically or chemically thinned, as in the case of supported nanoparticles, it is also generally necessary to use a support grid with holes and perform the spectroscopy on parts of the sample that overhang into free space for similar reasons of preventing overly complex spectra.

In this work, scanning transmission electron microscopy (STEM) with energy dispersive x-ray spectroscopy (EDS) was carried out in JEOL 2010F 200keV field-emission electron microscope with EDAX X-ray detector and Genesis software package. Electron energy loss spectroscopy (EELS) was carried out in a JEOL 2100F electron microscope (also 200keV) with CEOS spherical-aberration corrector on the probe forming side of the column. A Gatan Tridiem imaging filter was used to collect the EELS spectra.

3.5 References

1. Lynggaard, H., Andreasen, A., Stegelmann, C. & Stoltze, P. Analysis of simple kinetic models in heterogeneous catalysis. *Progress in Surface Science* **77,** 71–137 (2004).

2. Stoltze, P. Surface science as the basis for the understanding of the catalytic synthesis of ammonia. *Physica Scripta* **36,** 824–864 (1987).

3. Bligaard, T. *et al.* On the compensation effect in heterogeneous catalysis. *J. Phys. Chem. B* **107,** 9325–9331 (2003).

4. Stegelmann, C., Andreasen, A. & Campbell, C. T. Degree of Rate Control: How Much the Energies of Intermediates and Transition States Control Rates. *J. Am. Chem. Soc.* **131,** 8077–8082 (2009).

5. Chorkendorff, Ib, Niemantsverdriet, J. *Concepts of modern catalysis and kinetics*. (Wiley-VCH, 2003).

6. Hohenberg, P. & Kohn, W. Inhomogeneous electron gas. *Phys. Rev. B* **136,** B864 (1964).

7. Parr, R. G. & Yang, W. *Density-Functional Theory of Atoms and Molecules*. (Oxford University Press, 1989).

8. Koch, W. *A Chemist's Guide to Density Functional Theory*. (Wiley-VCH, 2008).

9. Szabo, A. & Ostlund, N. S. *Modern Quantum Chemistry: Introduction to Advanced Electronic Structure Theory*. (Dover Publications, 1996).

10. Shankar, R. *Principles of Quantum Mechanics*. (Springer, 1994).

11. Ashcroft, N. W. & Mermin, N. D. *Solid State Physics*. (Brooks Cole, 1976).

12. Kittel, C. *Introduction to Solid State Physics*. (Wiley, 1995).

13. Kohn, W. & Sham, L. J. Self-Consistent equations including exchange and corre- lation effects. *Physical Review* **140,** (1965).

14. Hammer, B., Hansen, L. B. & Norskov, J. K. Improved adsorption energetics within density-functional theory using revised Perdew-Burke-Ernzerhof functionals. *Phys. Rev. B* **59,** 7413–7421 (1999).

15. Bell, A. T. & Head-Gordon, M. Quantum mechanical modeling of catalytic processes. *Annual review of chemical and biomolecular engineering* **2,** 453–77 (2011).

16. Perdew, J. P., Burke, K. & Ernzerhof, M. Generalized gradient approximation made simple. *Phys. Rev. Lett.* **77,** 3865–3868 (1996).

17. McQuarrie, D. A. *Statistical Mechanics*. (University Science Books, 2000).

18. Chandler, D. *Introduction to Modern Statistical Mechanics*. (Oxford University Press, 1987).

19. http://webbook.nist.gov/chemistry/.

20. Nørskov, J. K. *et al.* Origin of the overpotential for oxygen reduction at a fuel-cell cathode. *J. Phys. Chem. B* **108,** 17886–17892 (2004).

21. Karlberg, G. S., Rossmeisl, J. & Norskov, J. K. Estimations of electric field effects on the oxygen reduction reaction based on the density functional theory. *Phys. Chem. Chem. Phys.* **9,** 5158–5161 (2007).

22. Kandoi, S., Gokhale, A. A., Grabow, L. C., Dumesic, J. A. & Mavrikakis, M. Why Au and Cu are more selective than Pt for preferential oxidation of CO at low temperature. *Catalysis Letters* **93,** 93–100 (2004).

23. Ma, Z. & Zaera, F. Heterogeneous Catalysis by Metals. *Encyclopedia of Inorganic Chemistry* 1–17 (2006). doi:10.1002/0470862106.ia084

24. Xia, Y., Xiong, Y. J., Lim, B. & Skrabalak, S. E. Shape-Controlled Synthesis of Metal Nanocrystals: Simple Chemistry Meets Complex Physics? *Angew. Chem. Int. Ed.* **48,** 60–103 (2009).

25. Christopher, P. & Linic, S. Engineering selectivity in heterogeneous catalysis: Ag nanowires as selective ethylene epoxidation catalysts. *J. Am. Chem. Soc.* **130,** 11264–11265 (2008).

26. Christopher, P. & Linic, S. Shape- and Size-Specific Chemistry of Ag Nanostructures in Catalytic Ethylene Epoxidation. *ChemCatChem* **2,** 78–83 (2010).

27. Lopez-Sanchez, J. A. *et al.* Facile removal of stabilizer-ligands from supported gold nanoparticles. *Nature Chemistry* **3,** 551–556 (2011).

28. Borodko, Y., Lee, H. S., Joo, S. H., Zhang, Y. & Somorjai, G. Spectroscopic Study of the Thermal Degradation of PVP-Capped Rh and Pt Nanoparticles in H(2) and O(2) Environments. *J. Phys. Chem. C* **114,** (2010).

29. Rioux, R., Song, H., Grass, M. & Habas, S. Monodisperse platinum nanoparticles of well-defined shape: synthesis, characterization, catalytic properties and future prospects. *Topic in Catalysis* **39,** 167–174 (2006).

30. Ertl, G., Weitkamp, J. & Helmut Knözinger. *Preparation of Solid Catalysts*. (John Wiley & Sons, Inc., 1999).

31. Campbell, C. T., Parker, S. C. & Starr, D. E. The Effect of Size-Dependent Nanoparticle Energetics on Catalyst Sintering. *Science* **298,** 811–814 (2002).

32. Wang, D. & Li, Y. Bimetallic nanocrystals: liquid-phase synthesis and catalytic applications. *Advanced Materials* **23,** 1044–60 (2011).

33. Peng, Z., Kisielowski, C. & Bell, A. T. Surfactant -free preparation of supported cubic platinum nanoparticles. *Chem. Comm.* **48,** 1854–1856 (2012).

34. Menning, C. A. & Chen, J. G. General trend for adsorbate-induced segregation of subsurface metal atoms in bimetallic surfaces. *J. Chem. Phys.* **130,** 174709 (2009).

35. Zhang, Z. Y., Nenoff, T. M., Huang, J. Y., Berry, D. T. & Provencio, P. P. Room Temperature Synthesis of Thermally Immiscible Ag-Ni Nanoalloys. *J. Phys. Chem. C* **113,** 1155–1159 (2009).

36. Vasquez, Y., Luo, Z. & Schaak, R. E. Low-temperature solution synthesis of the non-equilibrium ordered intermetallic compounds Au3Fe, Au3Co, and Au3Ni as nanocrystals. *J. Am. Chem. Soc.* **130,** 11866–7 (2008).

37. Karakaya, I. and Thompson, W. T. The Ag-Co (Silver-Cobalt) System. *Bulletin of Alloy Phase Diagrams* **7,** 259–263 (1986).

38. Singleton, M. & Nash, P. The Ag-Ni (Silver-Nickel) System: *Bulletin of Alloy Phase Diagrams* **8,** 119–121 (1987).

39. Swartzendruber, L. J. The Ag-Fe (Silver-Iron) System. *Bulletin of Alloy Phase Diagrams* **5,** 560–564 (1984).

40. Gong, K., Su, D. & Adzic, R. R. Platinum-monolayer shell on AuNi(0.5)Fe nanoparticle core electrocatalyst with high activity and stability for the oxygen reduction reaction. *J. Am. Chem. Soc.* **132,** 14364–6 (2010).

41. Goodwin, A. L. *et al.* Colossal positive and negative thermal expansion in the framework material Ag3[Co(CN)6]. *Science* **319,** 794–7 (2008).

42. Ludi, A., Gudel, H. U. & Dvorak, V. The structure of H3Co(CN)6 and Ag3Co(CN)6. *Helvetic Chimica Acta* **7,** 2035–2039 (1967).

43. Kirowa-Eisner, E., Bonfil, Y., Tzur, D. & Gileadi, E. Thermodynamics and kinetics of upd of lead on polycrystalline silver and gold. *J. Electroanalytical Chem.* **552,** 171–183 (2003).

44. Herrero, E., Buller, L. J. & Abruna, H. D. Underpotential deposition at single crystal surfaces of Au, Pt, Ag and other materials. *Chemical Reviews* **101,** (2001).

45. Markovic, N. M. & Ross, P. N. Surface science studies of model fuel cell electrocatalysts. *Surface Science Reports* **45,** 117–229 (2002).

46. Bard, A. J. & Faulkner, L. R. *Electrochemical Methods: Fundamentals and Applications*. (John Wiley & Sons, Inc., 2001).

47. Blizanac, B. B., Ross, P. N. & Markovic, N. M. Oxygen reduction on silver low-index single-crystal surfaces in alkaline solution: Rotating ring Disk(Ag(hkl)) studies. *J. Phys. Chem. B* **110,** 4735–4741 (2006).

48. *Reference 3000 Potentiostat/Galvanostat/ZRA Operator's Manual*. (Gamry Instruments Inc., 2009).

49. Myland, J. C. & Oldham, K. B. Uncompensated resistance. 1. The effect of cell geometry. *Analytical Chemistry* **72,** 3972–80 (2000).

50. Smart, L. E. & Moore, E. A. *Solid State Chemistry*. (Taylor & Francis Group, 2005).

51. www.emal.engin.umich.edu.

52. Williams, D. B. & Carter, C. B. *Transmission Electron Microscopy*. (Springer, 2009).

53. Muller, D. a *et al.* Atomic-scale chemical imaging of composition and bonding by aberration-corrected microscopy. *Science* **319,** 1073–6 (2008).

54. Batson, P. E., Dellby, N. & Krivanek, O. L. Sub-ångstrom resolution using aberration corrected electron optics. *Nature* **418,** 617–20 (2002).

55. Egerton, R. F. Electron energy-loss spectroscopy in the TEM. *Reports on Progress in Physics* **72,** 016502 (2009).

56. Keast, V. J., Scott, a J., Brydson, R., Williams, D. B. & Bruley, J. Electron energy-loss near-edge structure -- a tool for the investigation of electronic structure on the nanometre scale. *J. Microscopy* **203,** 135–75 (2001).

57. Nikolla, E., Schwank, J. & Linic, S. Measuring and Relating the Electronic Structures of Nonmodel Supported Catalytic Materials to Their Performance. *J. Am. Chem. Soc.* **131,** 2747–2754 (2009).

Chapter 4: Elementary Mechanisms in Electrocatalysis: Revisiting the ORR Tafel Slope

We use microkinetic modeling to illustrate that deviations from ideal Tafel kinetics, which assumes a linear relationship between overpotential and log-current, are an inherent property of multi-step heterogeneous electrocatalytic reactions. We show that in general, deviations from ideal Tafel behavior can often be attributed to a simultaneous increase in the rate of the rate-limiting elementary step and a change in the number of available active sites on the electrode as overpotential is induced. Our analysis shows that in the oxygen reduction reaction (ORR) on Pt electrodes, which exhibits nonlinear Tafel behavior, changing electrode potential affects not only the rate-limiting step (the initial electron transfer to molecular oxygen), but also the concentration of surface intermediates—mainly OH and H_2O. Based on comparison of measured and predicted changes in Tafel slope (as well as pH dependence), we show that alternative interpretations of the non-ideal Tafel behavior of ORR on Pt, such as changes in rate-limiting step or adsorbate repulsion effects, are inconsistent with the observed ORR kinetics.

4.1 Introduction

Uncovering the elementary mechanisms of catalytic reactions is paramount to the design and optimization of new catalyst materials, including electrodes for electrocatalytic transformations, such as the oxygen reduction reaction (ORR), O_2 + $4H^+ + 4e^- \rightarrow 2H_2O$. Though many mechanistic inferences can be drawn by probing current-potential behavior and performing various in-situ and ex-situ characterization studies, the poor accessibility and complex structure of the electrode-electrolyte interface have hindered our understanding of electrocatalytic processes in comparison to their thermochemical counterparts.

One phenomenon that is poorly understood is the deviation of the observed kinetic behavior, for some reactions (most notably ORR), from that predicted by the electro-kinetic Tafel equation:

$$\Delta E = a + b \log(i) \tag{4.1}$$

Here, ΔE is the difference between the applied potential and the equilibrium potential, a is a constant related to the magnitude of forward and reverse current at equilibrium, and b is the Tafel slope, also a constant and expressed in mV/decade current gain. The Tafel equation points to a linear relation between electrode potential and the log of current. Surprisingly, it has been demonstrated experimentally that the measured Tafel slope for many electrocatalytic reactions including ORR on Pt changes with applied potential.[1–8] In addition, reaction orders—the dependences of rate on reactant concentrations—have similarly been

found to vary with potential. These changes in kinetic behavior have been explained in terms of coverage-dependent repulsion between adsorbed intermediates (usually modeled using a Temkin isotherm), active-site blocking by unreactive species, and even potential-induced change in the rate-limiting step (RLS).[1–3,5,9,10]

Herein, we utilize microkinetic modeling to demonstrate analytically that rapid changes in the kinetic behavior (Tafel slope and reaction orders) of electrochemical reactions are an inherent property of electrode kinetics that involve multiple elementary steps, even with non-interacting adsorbates (a Langmuir isotherm) and a single RLS. For the ORR on Pt, our analysis reveals that the measured Tafel slope, including its shift from about ~60mV/decade of current at low overpotential to ~120mV/dec at higher overpotential, is consistent with the initial electron transfer as the sole RLS over the entire range of operating potentials. We show that oxygen-containing reaction intermediates impact the rate at small overpotentials through surface site blocking even when their removal involves fast quasi-equilibrated steps. The coupling of such equilibrium processes to the rate-limiting step leads to a coverage-dependent, and hence potential-dependent apparent Tafel slope. We further calculate the apparent pH dependence of the ORR kinetics and illustrate that non-constant reaction orders with respect to proton and hydroxyl concentrations are also the natural consequence of potential-dependent equilibria affecting the surface concentrations of adsorbed intermediates and free sites. This analysis fits within a long-established framework of heterogeneous kinetic theory[11–13] and serves as a means of interpreting the Tafel slope in terms of elementary electrochemical reactions.

4.1.1 Oxygen Reduction on Pt Electrodes

Oxygen reduction ($O_2 + 4H^+ + 4e^- \rightarrow H_2O$) on Pt electrodes has been studied extensively for over half a century, and a great wealth of literature exists, cataloging the kinetic behavior, the state of the active electrode surface, and proposed mechanisms. Pt is the best pure metal ORR catalyst, but it still requires a large overpotential (~300mV) to achieve any appreciable current density.[14,15] Thus, there is great room for improvement and a mechanistic understanding of the reaction may provide the insight needed to achieve better performance.

Figure 4-1(a) shows an ORR Tafel plot (log kinetic current vs. overpotential) for polycrystalline Pt in O_2-saturated, 0.1M $HClO_4$ (full experimental details are provided in section 4.5). At low current densities (*lcd*), the Tafel slope is ~ -60mV/dec, but it rapidly increases to ~ -120mV/dec at high current density (*hcd*), which has been observed in prior work.[1,2,16,17] Such changing Tafel behavior has also been reported for low-index single crystal Pt electrodes[4,9,18–22] and supported Pt nanoparticles.[23,24] We note that the precise values of the slope reported tend to vary a small amount with crystal facet and factors such as electrolyte purity, uncompensated resistance correction, and the chosen boundaries for linear fitting of the curve. Adsorbing electrolyte ions such as sulfate[17,18,25] or phosphate[26,27] inhibit adsorption of intermediates and impact the observed slopes as well, but in non-adsorbing electrolytes (e.g. perchloric acid or alkaline solutions) there are many independent measurements of an *lcd* Tafel slope in the -50 to -80mV/decade range, growing to -100 to -130 mV/decade at *hcd*. The transition is also marked by a change in the apparent pH dependence, as the reaction order with respect to the

concentration of H^+ is observed to fall from about 3/2 to 1 in acid solution and with respect to the concentration of OH- in base from about -1/2 to 0.[2,28,29]

The changes in ORR kinetic behavior on Pt surfaces have been noted to accompany changes in the coverage of adsorbed oxygen-containing species. These species can originate from both water and O_2. Cyclic voltammetry (CV) on Pt(111) in deaerated solution shows two distinct oxidative features, the first of which ($\sim 0.8 V_{RHE}$) is fully reversible and attributed to hydroxyl adsorption. The second oxidation of Pt(111) occurs above $\sim 1.0 V_{RHE}$ and yields a poorly defined phase referred to as "surface oxide". Other low-index facets of Pt exhibit overlap in what is assumed to be initial OH adsorption and transition to "oxide."[10,30] Polycrystalline Pt thus tends to exhibit a broad oxidative feature, which we show in a CV in Figure 4-1(b). We also overlay a representative ORR polarization curve (rotating disk electrode method) on the same material to illustrate the overlap between onset of ORR activity and removal of oxygen containing species. It is in this region that the Tafel slope also undergoes its characteristic shift on all low-index surfaces of Pt.

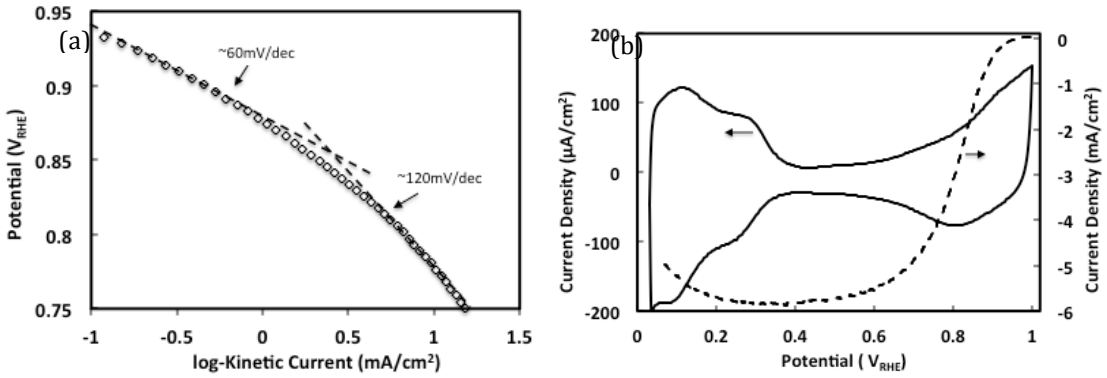

Figure 4-1: Comparison of ORR Tafel plot and cyclic voltammetry in deaerated electrolyte. *(a)* Tafel plot for ORR *i-E* behavior measured for a polycrystalline Pt rotating disk electrode at 1600RPM and a scan rate of 10mV/s in O_2 saturated 0.1M $HClO_4$ electrolyte. *(b) Dashed line:* ORR polarization curve corresponding to Tafel plot. *Solid line:* Cyclic voltammogram recorded at 100mV/s in Ar-deaerated 0.1M $HClO_4$

The mechanism of the ORR on Pt is not conclusively agreed upon, but a number of recent DFT studies probing the energy of potential intermediates[31–34] have indicated that oxygen is most likely adsorbed in the molecular state prior to dissociation. After addition of a proton/electron pair, the resulting OOH intermediate is high in energy and should rapidly decompose. In-situ infrared spectroscopy[35,36] also supports molecular adsorption and has suggested the formation of superoxide ion (O_2^-), pointing to sequential rather than simultaneous electron/proton transfer. Regardless of this detail, the high sensitivity required to detect such trace intermediates supports the theory that decomposition after the initial reduction is a fast process. An OOH intermediate could decompose in a pure chemical step to O and OH surface species, or electrochemically through reduction to either two OH groups or a water molecule and adsorbed O. These mechanistic possibilities are illustrated in Figure 4-2(a). Once atomic oxygen and hydroxyl groups are generated, these are reduced to water, as shown in Figure 4-2(b). Each

reduction is generally assumed to be an electrochemical proton/electron addition, but reductions can also occur by hydrogen atom transfer from adsorbed water molecules, so only the intermediate species are shown in Figure 4-2. Arguments have been put forth proposing that the RLS may be electron transfer to O_2,[1,20,30] OH-removal,[33,37] or even multiple steps that control the rate at different potentials.[5] The consequences of various limiting processes on the kinetics of a given mechanism are explored below.

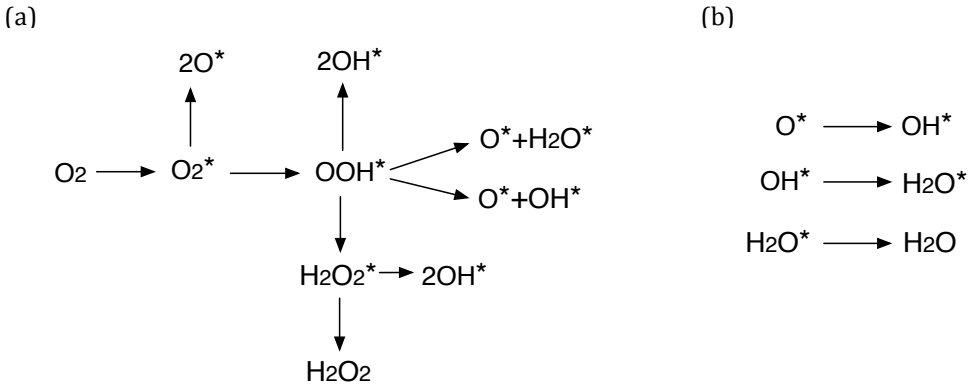

Figure 4-2: Possible ORR reaction pathways. Potential mechanisms of *(a)* initial reduction and decomposition of O_2 and *(b)* removal of adsorbed oxygen and hydroxyl. Species with an asterisk (*) are adsorbed.

4.2 Electrode Rate Laws and Microkinetic Modeling

The rate of an elementary electron transfer reaction can be described by the Butler-Volmer current-potential relationship, given in Equation (4.2).[38]

$$i = i_0 \left[\exp\left(\frac{(1-\beta)nF}{RT} (E - E_{eq}) \right) - \exp\left(\frac{-\beta nF}{RT} (E - E_{eq}) \right) \right] \qquad (4.2)$$

Here, E and E_{eq} are the applied and equilibrium potentials respectively, n is the number of electrons transferred, F is Faraday's constant, R is the gas constant, and T is the absolute temperature. The kinetic parameters that are unique to a given

reaction and electrode material are the exchange current, i_0, and the symmetry factor, β. The exchange current is the magnitude of the anodic and cathodic currents at equilibrium, while the symmetry factor ranges between 0 and 1 and describes the influence of the electrode potential on the energy of the transition state—it is typically assumed to be near 1/2. At moderately large overpotentials (E-E_{eq}), the reaction is effectively irreversible and Equation (4.2) will reduce to a single exponential (Tafel equation) describing either the anodic or cathodic current.

For a multistep, multi-electron process, if one assumes a single RLS, one can express the overall rate in a similar form, replacing the symmetry factor and number of electrons with an empirical parameter α (the transfer coefficient), which is not restricted in range and describes the sensitivity of the overall reaction rate to potential.[39] We give a generalized rate law for an irreversible cathodic reaction (e.g. ORR) in Equation (4.3), where for simplicity we reference the potential relative to a standard state reference potential, E^0, which is constant and generally chosen to be the equilibrium potential of the overall reaction at standard conditions. We also explicitly include the standard free energy of activation at the reference potential, ($\Delta G^{0,\ddagger}$), rather than absorbing it into the prefactor (k^0).

$$|i| = \frac{N}{\upsilon} \mathrm{F} k^0 \cdot \prod [a_i]^{\delta_i} \cdot \exp\left(\frac{-\Delta G^{0,\ddagger} - \alpha F(E - E^0)}{RT}\right) \tag{4.3}$$

In the general rate law above, activities of reactants are designated as a_i, and their reaction orders are given by δ_i. The total number of electrons transferred in the reaction is N, and ν is the stoichiometric number, signifying the number of times the rate limiting step must turn over to yield a complete reaction. Given such a rate law, it follows that the apparent transfer coefficient for the reaction is given by

Equation (4.4). This expression holds for any electrode process that is far from equilibrium.

$$\alpha = -\frac{RT}{F}\frac{\partial \ln|i|}{\partial E} \tag{4.4}$$

Alternatively, we may rearrange Equation (4.4) to give the Tafel slope, shown in Equation (4.5). Our analysis will focus on the transfer coefficient, as it is more directly computed and does not require inverting the rate law, but it is easily converted to the Tafel slope via Eqn. (4.5).

$$\frac{\partial E}{\partial \log|i|} = -\frac{2.3RT}{\alpha F} \tag{4.5}$$

We will consider a likely, acid-mediated ORR mechanism, in which O_2 is electrochemically reduced to OOH, followed by a fast, chemical decomposition to O and OH. The O and OH are then reduced electrochemically to create water. This pathway, shown below, will be designated Mechanism 1. Asterisks (*) indicate active surface sites, which we assume are equivalent on a given facet. Rate laws for a variety of other mechanisms are analyzed in the supporting information.

(1) $O_2 + H^+/e^- + * \leftrightarrows OOH^*$

(2) $OOH^* + * \leftrightarrows O^* + OH^*$

(3) $O^* + H^+/e^- \leftrightarrows OH^*$

(4) $2(OH^* + H^+/e^- \leftrightarrows H_2O + *)$

We now develop rate laws and the resulting Tafel slopes and reaction orders assuming that different elementary steps in Mechanism 1 are rate limiting and that all other steps are quasi-equilibrated. We will first assume that the initial electron transfer is rate-limiting and that steps 2-4 are in quasi-equilibrium. The rate for this

mechanism is given by Equation (4.6), for which we note that each pressure and concentration is a unitless activity and should be divided by a reference value.

$$i = i_1 = k_1 P_{O_2} [H^+] \theta_* - k_{-1} \theta_{OOH} \tag{4.6}$$

The coverages of each surface intermediate (θ_i) are then determined by the equilibria of the fast steps (2-4) and the constraint that all coverages must sum to unity. These are shown in Equations (4.7)-(4.10).

$$\theta_{OH} = \frac{1}{K_4 [H^+]} \theta_* \tag{4.7}$$

$$\theta_O = \frac{1}{K_3 K_4 [H^+]^2} \theta_* \tag{4.8}$$

$$\theta_{OOH} = \frac{1}{K_2 K_3 K_4^2 \, [H^+]^3} \theta_* \tag{4.9}$$

$$\theta_* = \left(1 + \frac{1}{K_4 [H^+]} + \frac{1}{K_3 K_4 [H^+]^2} + \frac{1}{K_2 K_3 K_4^2 \, [H^+]^3}\right)^{-1} \tag{4.10}$$

In the above expressions, each electron transfer reaction has an elementary rate constant, k_i, and an equilibrium constant, K_i, with the forms:

$$k_i = k_i^0 \exp\left(\frac{-\Delta G_i^{0,\ddagger} - n_i \beta_i F (E - E_i^0)}{RT}\right) \tag{4.11}$$

$$K_i = \exp\left(\frac{-\Delta G_i^0 - n_i F (E - E_i^0)}{RT}\right) \tag{4.12}$$

After plugging Equations (4.7)-(4.12) into the rate law where appropriate, we may compactly express the rate as Equation (4.13), where we define K_{eq} as the product of elementary equilibrium constants, and we use the reaction quotient, $Q = 1/(P_{O2}[H^+]^4)$, to define the fractional approach to equilibrium, Q/K_{eq}.

$$i = k_1 P_{O_2} [H^+] \cdot \left(1 - \frac{Q}{K_{eq}}\right) \cdot \theta_* \tag{4.13}$$

Since the reaction occurs far beyond the equilibrium potential, Q=0 and the forward (cathodic) rate, given by $k_1 P_{02}[\mathrm{H^+}]\theta_*$, is dominant. We may apply Equation (4.4) to find the transfer coefficient:

$$\alpha = -\frac{RT}{F}\frac{\partial}{\partial E}\left[\ln\left(k_1 \cdot P_{O_2} \cdot [H^+] \cdot \theta_*\right)\right] = \beta_1 + \theta_{OH} + 2\theta_O + 3\theta_{OOH} \qquad (4.14)$$

Here, the β_1 term comes from the elementary rate constant of step 1 (the RLS), and each coverage term is derived from the electrochemical equilibrium constants in the expression for θ_*. If we perform the analysis above again, considering each possible RLS, we find the transfer coefficient expressions given in Table 4-1. Further information regarding the adsorbate coverages is needed to calculate numerical values for the transfer coefficients and Tafel slopes, but in Table 4-1 we provide values for Tafel slopes in the limit of zero adsorbate coverage (assuming symmetry factors of ½ for elementary electron transfers). These Tafel slope values will apply in the high overpotential, high current regime of the ORR, where the surface is effectively clean. Under these conditions the measured slope is ~ 120mV/dec. Based on our analysis, it is clear that the most experimentally consistent RLS on Pt appears to be the initial electron transfer to O_2. Our analysis also shows that for this RLS, the slope will decrease as the coverage of intermediates rises. This is also consistent with experiment and will be discussed in more detail later in this text. Additionally, in Appendix 4.6.3 we show that the transfer coefficient does not change when the mechanism is base-mediated.

Elementary Step	Apparent α if RLS	Tafel Slope (θ_*=1)
(1) O_2 + H^+/e- + * → OOH*	$\alpha = \beta_1 + \theta_{OH} + 2\theta_O + 3\theta_{OOH}$	120
(2) OOH* + * → O*+OH*	$\alpha = 1 + 2\theta_{OH} + 4\theta_O - 2\theta_{OOH}$	60
(3) O* + H^+/e- → OH*	$\alpha = \beta_3 + 2 + \theta_{OH} - 2\theta_O - \theta_{OOH}$	24
(4) 2(OH* + H^+/e- → H_2O+*)	$\alpha = \beta_4 + 1 - \theta_{OH} - \theta_{OOH}$	40

Table 4-1 Apparent transfer coefficients and corresponding zero adsorbate coverage Tafel slopes for each potential RLS of Mechanism 1.

4.2.1 *The Apparent Transfer Coefficient*

The apparent transfer coefficient describes the sensitivity of an electrochemical reaction rate (more specifically the apparent free energy of activation) to applied electrical potential. We have determined that for any set of elementary steps in an electrocatalytic cycle, the apparent transfer coefficient, and hence the Tafel slope, can be obtained with the expression:

$$\alpha = \underbrace{\beta n_e^{\ddagger}}_{i} + \underbrace{\frac{1}{\nu}\sum_{RLS\text{reactants}} n_{e,i}^{f}}_{ii} + \underbrace{N_*^{\ddagger}\sum_{\text{Adsorbates}} n_{e,i}^{des}\,\theta_i}_{iii} \qquad (4.15)$$

Each term in Equation (4.15) describes the sensitivity of a component of the apparent free energy of activation to the applied potential as described below:

i) Term i describes the sensitivity of the free energy of activation of the RLS to applied potential. This is the symmetry factor of the RLS (β) multiplied by the number of electrons transferred in each turnover of the RLS ($n_e^{\ddagger}$).

ii) Term ii describes the sensitivity of the formation energy of the reactants in the RLS to potential, and it is given by the number of

electrons transferred to form the reactants participating in the RLS (n_e^f) divided by the stoichiometric number (ν). This can be interpreted as an increase in the activity of the reactants participating in the RLS due to the overvoltage, which affects the overall reaction rate by shifting any electrochemical (quasi)equilibria in which they participate.

iii) Term iii describes the sensitivity of the free energy required to liberate adsorption sites (any free site), to the applied potential. It is given by the number of electrons transferred in the desorption process for each surface species ($n_{e,i}^{\mathrm{des}}$), multiplied by the respective coverage of each surface species and the number of sites involved in the RLS ($N_*^{\ddagger}$). This term arises because the rate of reaction is proportional to the number of free sites. The transfer coefficient changes with changes in the coverage of any site blocking species, whether it is a reactive intermediate or a spectator species whose coverage responds to potential.

We note that terms (i) and (ii) have been described to some extent in prior derivations of an apparent transfer coefficient.[40–42] Herein, we show that the availability of active sites also influences the apparent transfer coefficient and therefore the response of the reaction rate to potential. It is the impact of the applied potential on the availability of active sites that can account for shifts in the observed Tafel slope without any change in mechanism or rate-limiting step. This is

an inherent kinetic phenomenon, which is present even without consideration of any additional effects, such as adsorbate-adsorbate interaction, electrolyte ion adsorption, or electric field interaction with adsorbate dipoles (though these effects may still account for some discrepancies between predicted and observed values).

4.2.2 Apparent Reaction Orders

In a similar manner to the determination of transfer coefficients, we may use the rate law to determine the apparent reaction order with respect to a given reactant. The dependence of rate on reactant activities can be an additional diagnostic criterion for various mechanisms and can be straightforwardly computed according to:

$$\delta_i = \frac{\partial \ln|i|}{\partial \ln(a_i)} \tag{4.16}$$

For a general elementary step mechanism, the apparent reaction order will be given by:

$$\delta_i = \delta_i^0 + N_*^{\ddagger} \sum_j N_{i,j}^{des} \theta_j \tag{4.17}$$

Much like the apparent transfer coefficient, apparent reaction orders can be broken into their fundamental contributions. Each reaction order contains two components: (i) a constant, δ_i^0, that is the stoichiometric coefficient of the species in the rate-limiting step, and (ii) a coverage term that expresses that changing the concentration of a species will change the number of free sites and impact the rate. The coefficient in front of each adsorbate coverage ($N_{i,j}^{\text{des}}$) will equal the number of molecules of the species of interest (the species we are finding the reaction order for) required to remove the adsorbate, and it will also be multiplied by the number

of sites in the RLS, $N_*^{\ddagger}$. For example, if we assume step 1 limits Mechanism 1, we would express OOH removal as the sum of steps 2-4. This process ($OOH^*+3H^+/e^-=2H_2O+^*$) has a stoichiometric coefficient of 3 for $[H^+]$, which results in a $3\theta_{OOH}$ term for the apparent order wrt $[H^+]$. These coefficients may be positive or negative depending on whether increasing the concentration causes the adsorbate coverage to decrease or increase respectively. In a similar manner, the constant stoichiometric coefficient, δ_i^0, can be found by adding the appropriate equilibrium steps to the RLS so that the reactants are in terms of the non-adsorbed species of interest.

In Table 4-2, we show the expected coverage-dependent reaction orders of Mechanism 1 for both acid and base-mediated reactions (full derivations in Appendix 4.6.4). As mentioned above, moving from *lcd* to *hcd*, the experimental reaction order of ORR on Pt with respect to H^+ falls from about 3/2 to 1 in acid solution and with respect to OH- from about -1/2 to 0 in base. Using the reaction order expressions in Table 4-2 for each possible RLS, we see that the most consistent mechanism in both environments involves the initial electron transfer step as RLS. This step gives an expected order of 1 in acid and 0 in base under low coverage, *hcd* conditions. According to Table 4-2 these reaction orders will shift in the directions consistent with experimental observations as the coverage of adsorbates increases.

Elementary Step	Order wrt [H^+]	Order wrt [OH-]
(1) O_2 + * → OOH*	$1+\theta_{OH}+2\theta_O+3\theta_{OOH}$	$-\theta_{OH}-2\theta_O-3\theta_{OOH}$
(2) OOH* + * → O*+OH*	$1+2\theta_{OH}+4\theta_O-2\theta_{OOH}$	$-1-2\theta_{OH}-4\theta_O+2\theta_{OOH}$
(3) O* → OH*	$3+\theta_{OH}-2\theta_O-\theta_{OOH}$	$-2-\theta_{OH}+2\theta_O+\theta_{OOH}$
(4) 2(OH* → H_2O+*)	$2-\theta_{OH}-\theta_{OOH}$	$-1+\theta_{OH}+\theta_{OOH}$

Table 4-2 Apparent reaction orders with respect to H^+ and OH^- for each potential RLS of Mechanism 1.

4.3 Discussion

Thus far, we have shown that changes in the electrode surface coverage of adsorbed intermediates are manifested as a shift in the measured Tafel slope of a reaction. We also showed that the ORR Tafel slope of -120mV/dec, measured at low surface coverage of adsorbates, suggests that under these conditions the initial electron transfer to O_2 is the RLS. Tafel slope expressions for a number of alternative mechanisms and rate-limiting steps are provided in Table 4-3 in Appendix 4.6.5. There, we show that in each case, the initial reduction of O_2 is the only RLS that gives a low-coverage Tafel slope consistent with those observed experimentally.

In the regime of high adsorbate coverage, the complexity of "surface oxide" formation makes a quantitative assessment difficult for polycrystalline Pt. On the other hand, since Pt(111) shows well-resolved separation between OH adsorption and further surface oxidation, we attempt to quantitatively interpret the full Tafel behavior on this surface. We note that Pt(111) is the most stable and most active Pt facet, making it the most representative of polycrystalline and nanoparticle samples. Assuming OH to be the only intermediate present in significant quantities during the Tafel slope shift on Pt(111), we used the analysis discussed above to calculate the Tafel slope as a function of OH coverage (Figure 4-3). It is known from cyclic

voltammetry that on Pt(111) the saturating OH coverage is about 1/3. The plot indicates that if the initial electron transfer is limiting (step 1), the Tafel slope values are fairly consistent with experiment, shifting from -120mV/dec on a clean surface to -72mV/dec at a θ_{OH} value of 1/3. By comparison, if one assumed limitation by OH-removal, the Tafel slope would be close to the experimental value at high OH coverage, but it follows the incorrect trend, decreasing as OH-coverage decreases. It must also be noted that at extremely large overpotentials (beyond what is experimentally accessible without complete mass transport control) an electrochemical step will eventually become barrierless and controlled by its prefactor ($n_i\beta_i F(E - E_i^0) \geq \Delta G_i^{0,\ddagger}$ in Eq. (4.11)). This would result in an infinite Tafel slope, and we restrict our current conclusions to the region of experimentally accessible kinetics where the Tafel slope values can be confirmed, above ~0.6V_{RHE}. In terms of the individual components of the apparent transfer coefficient discussed above, the observed Tafel behavior can be understood as the number of free sites decreasing (by adding OH) concurrently with the rate of the RLS, leading to a larger sensitivity of the rate toward potential than the RLS would exhibit alone. There is no contribution from the formation energy of RLS reactants because the pH and partial pressure of oxygen are fixed externally and do not depend on electrochemical equilibria.

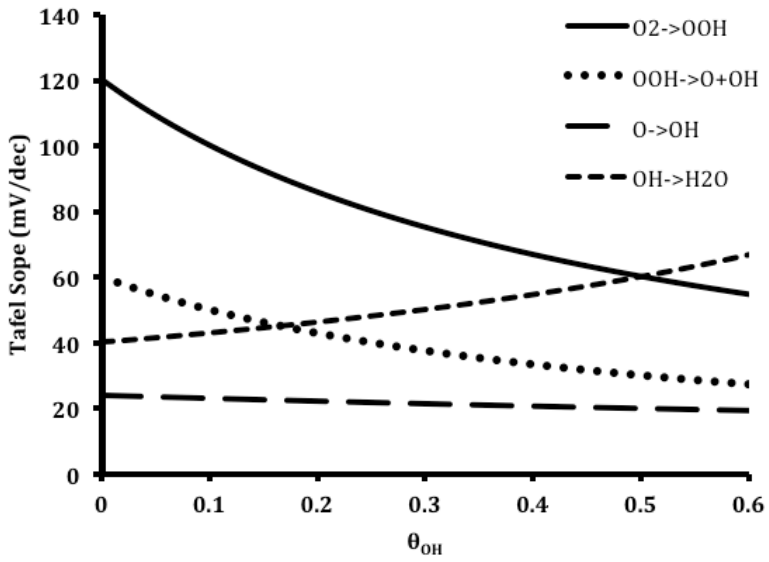

Figure 4-3: Tafel slope, as a function of OH coverage, for ORR Mechanism 1 assuming various rate-limiting steps on Pt(111).

Though there is reasonable agreement between the measured Tafel slope and that predicted by the micro-kinetic model discussed above in the limits of zero and saturating OH coverage, we note that numerous UHV experiments[43,44] and Density Functional Theory calculations[37,45] have indicated the propensity of OH to form ordered networks with coadsorbed water molecules on certain (111) surfaces, including Pt. These adsorbed water molecules do not contribute to the measured current in CVs, but they do have the potential to play a role in ORR kinetics. In order to probe the impact of these networks on the reaction kinetics, we performed electrochemical Density Functional Theory calculations to develop a phase diagram for the Pt(111) surface in the presence of the OH and H_2O adsorbates, shown in Figure 4-4. The calculations were performed using the generalized-gradient approximation (RPBE functional) and a plane-wave basis set, which have been shown to capture effects such as H-bonding with accuracy of about 0.05eV/bond.[46]

Further corrections were made to compensate for van der Waals interactions (full details in section 4.5). The calculations allow us to identify the surface configurations with the lowest Gibbs free energy as a function of electrode potential. These configurations will dominate the surface as long as there are no kinetic limitations that would prevent their formation. If we assume that the initial reduction of O_2 is the rate-limiting step and that other steps are quasi-equilibrated for all potentials of interest, then these networks of OH and H_2O will be a natural consequence of the equilibrium established at the Pt/H_2O interface.

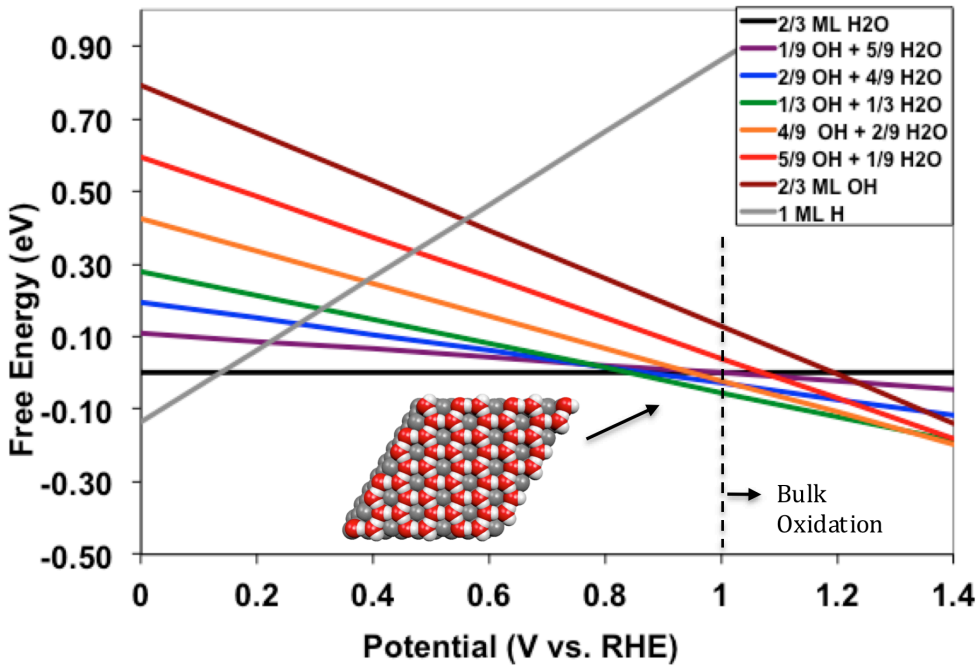

Figure 4-4: DFT-calculated phase diagram of adsorbate phases at the water-Pt(111) interface. Free energy of formation is normalized to the number of surface sites. *Inset:* Stable structure formed at 1/3 OH coverage.

The calculations in Figure 4-4 indicate that over a wide range of low potentials the most stable Pt surface in solution contains only weakly physisorbed water, with no other adsorbates. At potentials above ~0.8V_{RHE}, the most stable

surface structure changes to one characterized by an OH coverage of 1/3, interacting with an equal amount of water molecules through a network of H-bonds (see inset). These structures are consistent with previous reports using DFT,[37] and similar ordered phases have been identified with molecular dynamics simulations.[47] It is important to note that this network stabilizes water on the Pt(111) surface and that in this configuration the partial molar energy of adsorption for H_2O is similar to that of OH (referenced to H_2O and H^+/e^-). This suggests that under these conditions, water also behaves as a site-blocking species. The OH + H_2O surface coverage should thus approach 2/3 at high potentials, with some variation due to thermal fluctuations.

If we include adsorbed water, the site balance on Pt(111) would be given as $\theta_* + \theta_{OH} + \theta_{H_2O} = 1$. We can relate the coverage of water and OH by assuming $\theta_{H_2O} = x\theta_{OH}$, where x is the number of water molecules bound per OH (not necessarily one-to-one at low coverages). If the initial reduction of O_2 is the RLS and water also plays a role as a site blocker, the transfer coefficient becomes β_1+[1+x]$\theta_{OH.}$ We find that under these conditions the Tafel slope approaching the saturating coverage would be near -51mV/dec (x=1), which is still in reasonable agreement with the experimentally observed value of -60mV/dec.

Our analysis suggests that the ORR rate on Pt(111) at fixed pH can be expressed as follows:

$$i = k \cdot P_{O_2}\theta_*(E) \cdot \exp\left[\frac{-\beta FE}{RT}\right] \tag{4.18}$$

$$\theta_* = \left(1 + \frac{1+x}{K_4(E)}\right)^{-1} \tag{4.19}$$

All constant terms are contained in the prefactor, k, and the free site concentration, $\theta_*(E)$, is given as a function of potential via the quasi-equilibrium of OH + H_2O removal (K_4). These adsorbates will be abundant at small overpotentials, and the surface will be clean at larger overpotentials. As demonstrated above in the text, this rate expression yields experimentally consistent Tafel slopes. In comparison, several authors have proposed an empirical rate law in the form of Equation (4.20):[3,9,30,48]

$$i = k \cdot P_{O_2}(1 - \theta_{ad}) \cdot \exp\left[\frac{-\beta FE}{RT}\right] \exp\left[\frac{-\gamma r \theta_{OH}}{RT}\right] \qquad (4.20)$$

In this model, the fractional coverage of free sites (1-θ_{ad}) is obtained by integration of cyclic voltammograms, which account only for electrochemically deposited adsorbates, i.e., H_2O is not included in this balance. An additional coverage-dependent contribution to the activation barrier is also included (the second exponential term), in which r is a parameter describing adsorbate-adsorbate interaction strength and γ is a symmetry factor (assumed to be ½) relating this to the activation barrier. More specifically, in the adsorbate interaction model, OH adsorption is modeled with a Temkin isotherm, which assumes an increasingly endergonic adsorption energy with rising OH coverage (repulsive interaction). The adsorption energy of other oxygen-containing adsorbates (O_2, O, OOH) is then assumed to show a similar change with rising OH coverage, and the change in the activation barrier for these adsorption processes is assumed to scale as a fraction of the coverage-induced change in adsorption energy by using an additional symmetry factor, γ. Thus the activation barrier for the rate-limiting reductive adsorption of O_2 is shifted by $\gamma r \theta_{OH.}$ It is found that this additional barrier term significantly

improves the agreement with experimental results. However, the basis of Equation (4.20) on OH-OH repulsion is in sharp contrast to the observations showing that this interaction can be attractive due to the presence of water on the surface (i.e., H-bonding stabilizes the OH adsorbate at high OH coverage). Since water co-adsorption does not contribute to the integrated current in CVs, used in Eq. (4.20) to determine coverage, we propose that this model underestimates the occupancy of active sites at the low over-potential limit and the empirical repulsion term serves to partially offset the impact. We do not discount the notion that adsorbate interaction is influential at some magnitude, but it is likely smaller than previously assumed. Site availability and coupled equilibrium processes can largely account for the observed kinetic behavior.

A second hypothesis for the double Tafel slope is that changing potential may lead to different rate-limiting steps.[5] We mentioned above that two limiting steps (steps 1 and 4 in Mechanism 1) result in high-coverage Tafel slopes that are near the experimentally observed -60mV/dec. Slow OH-removal at high-coverage conditions could thus be argued to limit the rate at small overpotentials and surpass the rate of O_2 activation with increasing overpotential, giving way to a -120mV/dec Tafel slope. However, we believe that such an RLS tradeoff is unlikely. For elementary electrochemical reactions with Tafel-type rate laws, there are only two ways for one rate to surpass another. First, if the elementary symmetry factors are substantially different, one reaction rate may be more sensitive to potential than the other and overtake it as the potential is changed. However, since both OH-removal and initial O_2 reduction involve a proton/electron transfer, the assumption that the symmetry

factors are close in value is reasonable. Second, a large enough overpotential could make an initially fast step barrierless, causing the prefactor to control the rate. This elementary rate would cease to increase appreciably with potential and become rate limiting, while an initially slow step would continue to speed up. As mentioned previously, however, if a rate became dominated by the prefactor (or if a pure-chemical step became limiting), an infinite Tafel slope would be observed. This is not the case, and we expect the same step be rate limiting at all potentials.

Despite the arguments for limitation by the initial electron transfer to O_2, it is well known that electrodes with weaker OH binding energies, for example several Pt_3M alloys (M = Ni, Co, Fe), exhibit higher ORR activity than Pt.[16,17,48–50] Since our analysis points away from OH removal as rate limiting, we offer the following interpretation. Unlike most kinetic experiments done with differential conversion and low product concentration, water is the product of the ORR and it is abundant under reactive conditions. For this reason, the equilibrium coverage of OH (and accompanying H_2O) can be high, even if removal is fast and equilibrium is achieved very quickly. O_2 activation can be the slowest step while OH coverage still effectively reduces the rate. For an O_2-activation limited mechanism on a clean surface, an ordinary Sabatier analysis would indicate a more active electrode should bind oxygen more strongly. Unfortunately, making the surface more reactive will drive the equilibrium-driven decomposition of H_2O to OH to lower potentials, poisoning the surface. The next breakthrough in ORR catalysis will likely require materials that can decouple the binding energies of oxygen and hydroxyl groups, perhaps by destabilizing the hydrogen bonds that enhance the regime of OH poisoning.

4.4 Conclusions

We have demonstrated that for electrode reactions, simultaneous changes in electrocatalytic turnover rate and the number of active sites can lead to apparent nonlinear Tafel behavior and potential-dependent reaction orders. We have developed a microkinetic model which captures the relevant phenomena for oxygen reduction on Pt, and we find that the widely observed double Tafel slope, shifting from -60mV/dec to -120mV/dec, is indicative of a mechanism that is limited by the initial reduction of O_2. We show that intermediate species such as OH can block active sites and be present in high coverage, but can still be controlled by equilibrium. Coadsorbed species such as water are not apparent from cyclic voltammetry but may still alter the kinetics through site blocking as well. Alternate hypotheses for the non-ideal ORR kinetics, such as changes in rate-limiting step or adsorbate repulsion effects, are also shown to be inconsistent with observation. Our analysis serves generally as a means of interpreting the Tafel slope in terms of elementary electrochemical reactions.

4.5 Experimental Details

4.5.1 Electrochemical measurements

Electrochemical measurements were performed in an all-Teflon three-electrode cell (made in house) with a Princeton Applied Research PARSTAT 2273 potentiostat/galvanostat/FRA. Electrolyte solutions were prepared from ultrapure water (18MΩ, E-Pure), and perchloric acid (70% $HClO_4$, Fisher Scientific). Cyclic

voltammograms were taken in argon-purged water, and rotating disk polarization curves were taken in O_2-saturated water. The working electrode was a 5mm polycrystalline Pt disk (Pine Instruments), polished with 0.05μm alumina paste and sonicated in ultrapure water prior to use. The reference electrode (Radiometer Analytical) was Hg/Hg_2SO_4 in saturated K_2SO_4 (0.651V vs. NHE), and a platinum wire (Alfa Aesar) was used as a counter electrode. The reference and counter electrodes were both in isolated compartments with long diffusion paths to the working electrode chamber. An uncompensated resistance of ~40Ω was measured via the high frequency limit of the measured impedance, and this was corrected for in the polarization curves. All potentials are reported relative to the Reversible Hydrogen Electrode ($V_{RHE} = V_{NHE} + 0.0591pH$).

4.5.2 Density Functional Theory calculations

All DFT calculations were carried out with the Dacapo pseudopotential plane wave code (http://www.camd.dtu.dk), using the generalized gradient approximation (GGA) and RPBE exchange correlation functional. The Pt(111) system was modeled with three-layer, periodic 3x3 unit cells, separated by six layers of vacuum space in the (111)-direction and a dipole layer to electrostatically decouple the slabs. The bottom two layers were fixed to bulk positions (DFT optimized lattice constant of 4.00Å) while the top layer and all adsorbates were allowed to relax until the sum of the forces was below 0.05 eV/Å. Ultrasoft pseudopotentials were used to represent the ionic cores, while the valence electron density was determined through iterative diagonalization of the Kohn-Sham

Hamiltonian using Pulay mixing. All unit cells were sampled with a 3x3x1 Monkhorst-Pack k-point sampling grid, and the energy cutoff for the plane wave basis set was 350eV. An electronic temperature of 0.1 k_BT was used, with the final energies extrapolated to 0 K.

Electrochemical free energy phase diagrams were developed by using DFT to compute the adsorption energy of a given configuration of adsorbates on the Pt slab ($\Delta E_{adsorption}=E_{system}-E_{slab}-E_{adsorbates}$), then converting to Gibbs free energy with the following relationship: $\Delta G = \Delta E - T\Delta S + \Delta ZPE + ne(U-U_0)$. The adsorption energy is approximately equivalent to the change in enthalpy ($\Delta H \cong \Delta E$), while entropy changes (ΔS) were obtained from tabulated values (http://webbook.nist.gov/chemistry/). Zero point energy (ZPE) for each adsorbate was taken from prior DFT work (*J. Phys. Chem. B,* **108**, 17886, (2004)). The contribution of potential was computed using the computational equivalent to the standard hydrogen electrode, which exploits the equilibrium between H_2 and H^+/e^- at $0.0V_{NHE}$. The free energy of H_2 is thus substituted for the $[H^++e^-]$ pair to obtain ΔG values at $0.0V_{NHE}$. The free energy is then shifted by $ne(U-U_0)$, where n is the number of electrons transferred in the reaction.

The adsorption energy of adsorbed OH molecules was referenced to liquid water and gaseous H_2, and the reference state for adsorbed water was the average energy of a water molecule in a full aqueous bilayer on the Pt surface (the structure with 2/3 H_2O coverage). The reason for the different reference state for adsorbed water comes from the underprediction of Van der Waals forces by DFT. Prior work (*Electrochim. Acta,* **55**, 7975, (2010)) has shown that changing the reference state to

water in the bilayer yields similar formation energies to calculations using the vdF-DF functional (which better captures the Van der Waals effects) for surface structures containing adsorbed water molecules.

4.6 Appendices

4.6.1 List of Symbols

a_i	*activity of species i*
a	*Tafel intercept,* V
b	*Tafel slope,* V/log(A m^{-2}), (V/decade)
E	*electrode potential,* V
E_{eq}	*equilibrium potential,* V
E^0	*reference potential,* V
F	*Faraday constant,* 96,485 C mol^{-1}
ΔG_i	*Free energy change of reaction i,* J mol^{-1}
ΔG^0	*Free energy of reaction at reference conditions,* J mol^{-1}
$\Delta G_i^{\ddagger}$	*Free energy of activation of reaction i,* J mol^{-1}
i	*current density,* A m^{-2}
i_0	*exchange current density,* A m^{-2}
k_i	*rate constant of reaction i,* mol s^{-1} m^{-2}
K_i	*equilibrium constant of reaction i*
K_{eq}	*overall equilibrium constant*
k_i^0	*preexponential factor for reaction i,* mol s^{-1} m^{-2}
n	*number of electrons in an elementary step*
n_e^f	*number of electron transferred to form all RLS reactants*
$n_{e,i}^{des}$	*number of electrons transferred for desorption of species i*
$n_e^{\ddagger}$	*number of electrons in one RLS turnover*
N	*total number of electrons in reaction*

$N_*^{\ddagger}$ *number of free sites needed in RLS*

$N_{i,j}^{des}$ *number of i molecules required to remove adsorbate j*

P_i *partial pressure of species i,* Pa

Q *reaction quotient*

r *adsorbate interaction parameter,* J mol^{-1}

R *ideal gas constant*, 8.314 J mol^{-1} K^{-1}

T *temperature*, K

x *ratio of H_2O to bound OH*

α *transfer coefficient*

β_i *symmetry factor of charge transfer for reaction i*

γ *symmetry factor of adsorption*

δ_i *reaction order of species i*

δ_i^0 *reaction order of species i in the RLS*

θ_i *surface coverage of species i*

ν *stoichiometric number*

4.6.2 Full derivation of apparent transfer coefficient

Assume an elementary step mechanism as below:

(1) $O_2 + H^+/e^- + * \rightarrow OOH*$

(2) $OOH* + * \rightarrow O* + OH*$

(3) $O* + H^+/e^- \rightarrow OH*$

(4) $2(OH* + H^+/e^- \rightarrow H_2O + *)$

Quasi-equilibrium of steps 2-4 yields the following expressions:

$$K_2 = \frac{\theta_O \theta_{OH}}{\theta_{OOH} \theta_*} \qquad K_3 = \frac{\theta_{OH}}{\theta_O [H^+]} \qquad K_4 = \frac{\theta_*}{\theta_{OH} [H^+]}$$

For convenience, we rearrange them in terms to express each adsorbate coverage:

$$\theta_{OH} = \frac{1}{K_4 [H^+]} \theta_* \qquad \theta_O = \frac{1}{K_3 K_4 [H^+]^2} \theta_* \qquad \theta_{OOH} = \frac{1}{K_2 K_3 K_4^2 [H^+]^3} \theta_*$$

Using the additional constraint that all coverages sum to unity ($\theta_* + \theta_{OH} + \theta_O + \theta_{OOH} = 1$), we can express the coverage of free sites as below:

$$\theta_* = \left[1 + \frac{\theta_{OH}}{\theta_*} + \frac{\theta_O}{\theta_*} + \frac{\theta_{OOH}}{\theta_*}\right]^{-1} = \left[1 + \frac{1}{K_4[H^+]} + \frac{1}{K_3K_4[H^+]^2} + \frac{1}{K_2K_3K_4^2\,[H^+]^3}\right]^{-1}$$

Now that we can express θ_*, we may compute the transfer coefficient from the reaction rate, which is the forward rate of the assumed RLS, step 1:

$$i_c = r_1 = kP_{O_2}[H^+]\theta_*$$

Since the transfer coefficient is a derivative with respect to potential, we first show the derivatives of electrochemical rate constants (k_i) and equilibrium constants (K_i) as well as the derivatives of their logarithms, which will be required in later computations. This is only applicable to electron transfer reactions:

$$k_i = k_i^0 \exp\left[\frac{-\Delta G_{i,0}^{\ddagger} - n_i\beta_i F\left(E - E_i^0\right)}{RT}\right] \qquad \frac{\partial k_i}{\partial E} = -\frac{n_i\beta_i F}{RT}\cdot k_i \qquad \frac{\partial \ln k_i}{\partial E} = -\frac{n_i\beta_i F}{RT}$$

$$K_i = \exp\left[\frac{-\Delta G_{i,0} - n_i F\left(E - E_i^0\right)}{RT}\right] \qquad \frac{\partial K_i}{\partial E} = -\frac{n_i F}{RT}\cdot K_i \qquad \frac{\partial \ln K_i}{\partial E} = -\frac{n_i F}{RT}$$

The apparent transfer coefficient is thus computed as shown in the following steps. In each electron transfer reaction we have considered, n_i=1. Coefficients in front of the final coverage terms result from taking the product of multiple equilibrium constants.

$$\alpha = -\frac{RT}{F}\frac{\partial \ln|i|}{\partial E} = -\frac{RT}{F}\frac{\partial}{\partial E}\left[\ln k_1 + \ln P_{O_2} + \ln[H^+] + \ln\theta_*\right]$$

$$\alpha = \beta_1 + 0 + 0 + \frac{RT}{F}\theta_*\frac{\partial}{\partial E}[\theta_*^{-1}]$$

$$\alpha = \beta_1 + \frac{RT}{F}\theta_*\left[\frac{F}{RT}\frac{1}{K_4[H^+]} + \frac{2F}{RT}\frac{1}{K_3K_4[H^+]^2} + \frac{3F}{RT}\frac{1}{K_2K_3K_4^2\,[H^+]^3}\right]$$

$$\alpha = \beta_1 + \frac{RT}{F}\theta_* \left[\frac{F}{RT}\frac{\theta_{OH}}{\theta_*} + \frac{2F}{RT}\frac{\theta_O}{\theta_*} + \frac{3F}{RT}\frac{\theta_{OOH}}{\theta_*}\right] = \beta_1 + \theta_{OH} + 2\theta_O + 3\theta_{OOH}$$

4.6.3 Apparent transfer coefficient for hydroxide medium

In basic medium, H_2O is the source of protons rather than H_3O^+. We may convert an acid-mediated mechanism to equivalent steps in base by adding the autodissociation of water ($H_2O = H^+ + OH^-$) to each proton transfer step:

(1) O_2* + H_2O/e- + * → OOH* + OH^-

(2) OOH* + * → O* + OH*

(3) O* + H_2O/e- → OH* + OH^-

(4) 2(OH* + e- → * + OH^-)

Following the same procedure as given in section S1, it is easily shown that quasi-equilibrium approximation for steps 2-4 yields the adsorbate coverage expressions below.

$$\theta_{OH} = \frac{[OH^-]}{K_4}\theta_* \qquad \theta_O = \frac{[OH^-]^2}{K_3K_4}\theta_* \qquad \theta_{OOH} = \frac{[OH^-]^3}{K_2K_3K_4^2}\theta_*$$

These expressions are equivalent to the adsorbate coverage expressions derived for acid-mediated mechanisms, with the exception that $1/[OH^-]$ has replaced $[H^+]$. We could have achieved the conversion directly by invoking the equilibrium of water autodissociation: $[H^+] \propto 1/[OH^-]$. The solution-phase concentration of each species is not impacted by the potential, and thus, the subsequent steps outlined in section S1 yield the same derivatives with respect to potential and ultimately yield the same transfer coefficient.

4.6.4 Apparent reaction order derivation

Assuming the same acid-mediated mechanism shown in section S1, with step 1 as the RLS, we would once again have a forward rate given by $i_c = r_1 = kP_{O_2}[H^+]\theta_*$ and the same expression for θ_* as in section S1. We can calculate the apparent reaction order with respect to [H⁺] as illustrated below:

$$\delta_{H^+} = \frac{\partial \ln|i|}{\partial \ln[H^+]} = \frac{\partial}{\partial \ln[H^+]}\left[\ln k_1 + \ln P_{O_2} + \ln[H^+] + \ln \theta_*\right]$$

$$\delta_{H^+} = 1 - \theta_*[H^+]\frac{\partial \theta_*^{-1}}{\partial [H^+]} = 1 - \theta_*[H^+]\left[-\frac{1}{K_4[H^+]^2} - \frac{2}{K_3K_4[H^+]^3} - \frac{3}{K_2K_3K_4^2\,[H^+]^4}\right]$$

$$\delta_{H^+} = 1 + \theta_*[H^+]\left[\frac{1}{[H^+]}\frac{\theta_{OH}}{\theta_*} + \frac{2}{[H^+]}\frac{\theta_O}{\theta_*} + \frac{3}{[H^+]}\frac{\theta_{OOH}}{\theta_*}\right] = 1 + \theta_{OH} + 2\theta_O + 3\theta_{OOH}$$

4.6.5 Transfer coefficients and Tafel slopes for various potential reaction mechanisms

Below we present the formulas for the apparent transfer coefficient for a series of possible elementary step mechanisms for the ORR. The expressions are obtained with the formula derived in the main text, rewritten below. Each box following the formula contains a series of steps, the apparent α if a given step is rate limiting, and the corresponding values of the Tafel slope expected for a clean surface and one with θ_{OH}=1/3 if all other adsorbates are negligible. All Tafel slope values also assume elementary symmetry factors (β_i) are ½.

$$\alpha = \underbrace{\beta n_e^{\ddagger}}_{i} + \underbrace{\frac{1}{\nu}\sum_{RLS\text{reactants}} n_e^f}_{ii} + \underbrace{N_*^{\ddagger}\sum_{\text{Adsorbates}} n_{e,i}^{des}\,\theta_i}_{iii}$$

Step	**Apparent α**	**$\theta_*=1/\theta_{OH}$=0.33 Tafel**
(1) $O_2 + * \rightarrow O_2*$	$\alpha = \theta_{OH} + 2\theta_O + 3\theta_{OOH}+4\theta_{O2}$	∞ / 180
(2) $O_2* + H^+/e- \rightarrow OOH*$	$\alpha = \beta_2 + \theta_{OH} + 2\theta_O + 3\theta_{OOH}$	120/72
(3) $OOH* + * \rightarrow O* + OH*$	$\alpha = 1 + 2\theta_{OH} + 4\theta_O - 2\theta_{OOH}$	60/36
(4) $O* + H^+/e- \rightarrow OH*$	$\alpha = \beta_4 + 2 + \theta_{OH} - 2\theta_O - \theta_{OOH}$	24/21
(5) $2(OH* + H^+/e- \rightarrow H_2O + *)$	$\alpha = \beta_5 + 1 - \theta_{OH} - \theta_{OOH}$	40/51
(1) $O_2 + 2* \rightarrow 2O*$	$\alpha = 2\theta_{OH} + 4\theta_O$	∞/90
(2) $2(O* + H^+/e- \rightarrow OH*)$	$\alpha = \beta_2 + \theta_{OH}$	120/72
(3) $2(OH* + H^+/e- \rightarrow H_2O+*)$	$\alpha = \beta_3 + 1 - \theta_{OH}$	40/51
(1) $O_2 + H^+/e- + * \rightarrow OOH*$	$\alpha = \beta_1 + \theta_{OH} + 3\theta_{OOH}$	120/72
(2) $OOH* + H^+/e- + * \rightarrow 2OH*$	$\alpha = \beta_2 + 1 + 2\theta_{OH} - 2\theta_{OOH}$	40/28
(3) $2(OH* + H^+/e- \rightarrow H_2O+*)$	$\alpha = \beta_3 + 1 - \theta_{OH} - \theta_{OOH}$	40/51
(1) $O_2 + H^+/e- + * \rightarrow OOH*$	$\alpha = \beta_1 + \theta_{OH} + 2\theta_O + 3\theta_{OOH}$	120/72
(2) $OOH* + * \rightarrow O*+OH*$	$\alpha = 1 + 2\theta_{OH} + 4\theta_O - 2\theta_{OOH}$	60/36
(3) $O* + H^+/e- \rightarrow OH*$	$\alpha = \beta_3 + 2 + \theta_{OH} - 2\theta_O - \theta_{OOH}$	24/21
(4) $2(OH* + H^+/e- \rightarrow H_2O+*)$	$\alpha = \beta_4 + 1 - \theta_{OH} - \theta_{OOH}$	40/51
(1) $O_2 + H^+/e- + * \rightarrow OOH*$	$\alpha = \beta_1 + \theta_{OH} + 2\theta_O + 3\theta_{OOH}$	120/72
(2) $OOH* + H^+/e- + \rightarrow O* + H_2O$	$\alpha = \beta_2 + 1 + \theta_{OH} + 2\theta_O - \theta_{OOH}$	40/33
(3) $O* + H^+/e- \rightarrow OH*$	$\alpha = \beta_3 + 2 + \theta_{OH} - 2\theta_O - \theta_{OOH}$	24/21
(4) $OH* + H^+/e- \rightarrow H_2O+*$	$\alpha = \beta_4 + 3 - 3\theta_{OH} - 2\theta_O - \theta_{OOH}$	17/24
(1) $O_2 + H^+/e- + * \rightarrow OOH*$	$\alpha = \beta_1 + \theta_{OH} + 3\theta_{OOH} + 2\theta_{HOOH}$	120/72
(2) $OOH* + H^+/e- + \rightarrow H_2O_2*$	$\alpha = \beta_2 + 1 + \theta_{OH} - \theta_{OOH} + 2\theta_{HOOH}$	40/33
(3) $H_2O_2* + * \rightarrow 2OH*$	$\alpha = \beta_3 + 2 + 2\theta_{OH} - 2\theta_{OOH} - 4\theta_{HOOH}$	24/19
(4) $2(OH* + H^+/e- \rightarrow H_2O+*)$	$\alpha = \beta_4 + 1 - \theta_{OH} - \theta_{OOH} - 2\theta_{HOOH}$	40/51
(1) $O_2 + H^+/e- + * \rightarrow OOH*$	$\alpha = \beta_1 + \theta_{OH} + 2\theta_O + 3\theta_{OOH}$	120/72
(2) $OOH* + * \rightarrow O*+OH*$	$\alpha = 1 + 2\theta_{OH} + 4\theta_O - 2\theta_{OOH}$	60/36
(3) $O* + H_2O + * \rightarrow 2OH*$	$\alpha = 2 + 2\theta_{OH} - 4\theta_O - 2\theta_{OOH}$	30/23
(4) $3(OH* + H^+/e- \rightarrow H_2O+*)$	$\alpha = \beta_4 + {}^1/_3 - {}^1/_3\theta_{OH} - {}^2/_3\theta_O - \theta_{OOH}$	72/83
(1) $O_2 + H_2O + 2* \rightarrow OOH* + OH*$	$\alpha = 2\theta_{OH} + 4\theta_O + 6\theta_{OOH}$	∞ / 90
(2) $OOH* + * \rightarrow O* + OH*$	$\alpha = 1 + 2\theta_{OH} + 4\theta_O - 2\theta_{OOH}$	60/ 36
(3) $O* + H_2O + * \rightarrow 2OH*$	$\alpha = 2 + 2\theta_{OH} - 4\theta_O - 2\theta_{OOH}$	30/ 23
(4) $4(OH* + H^+/e- \rightarrow H_2O+*)$	$\alpha = \beta_5$	120/120
(1) $O_2 + 2* \rightarrow 2O*$	$\alpha = 2\theta_{OH} + 4\theta_O$	∞/90

(2) $2(O^* + H_2O \rightarrow 2OH^*)$	$\alpha = \theta_{OH}$	$\infty/180$
(3) $4(OH^* + H^+/e^- \rightarrow H_2O + *)$	$\alpha = \beta_3$	120/120
(1) $O_2 + H^+/e^- + * \rightarrow OOH^*$	$\alpha = \beta_1 + \theta_{OH} + 2\theta_O + 3\theta_{OOH}$	120/72
(2) $OOH^* + H^+/e^- + \rightarrow O^* + H_2O$	$\alpha = \beta_2 + 1 + \theta_{OH} + 2\theta_O - \theta_{OOH}$	40/33
(3) $O^* + H_2O \rightarrow 2OH^*$	$\alpha = 2 + \theta_{OH} - 2\theta_O - \theta_{OOH}$	30/26
(4) $2(OH^* + H^+/e^- \rightarrow H_2O + *)$	$\alpha = \beta_4 + 1 - \theta_{OH} - 2\theta_O - \theta_{OOH}$	40/51
(1) $O_2 + H_2O + 2^* \rightarrow OOH^* + OH^*$	$\alpha = 2\theta_{OH} + 4\theta_O + 6\theta_{OOH}$	$\infty/90$
(2) $OOH^* + H^+/e^- + \rightarrow O^* + H_2O$	$\alpha = \beta_2 + 1 + \theta_{OH} + 2\theta_O - \theta_{OOH}$	40/33
(3) $O^* + H^+/e^- \rightarrow OH^*$	$\alpha = \beta_3 + 2 + \theta_{OH} - 2\theta_O - \theta_{OOH}$	24/21
(4) $2(OH^* + H^+/e^- \rightarrow H_2O + *)$	$\alpha = \beta_4 + 1 - \theta_{OH} - \theta_{OOH}$	40/51
(1) $O_2 + H^+/e^- + * \rightarrow OOH^*$	$\alpha = \beta_1 + \theta_{OOH}$	120 ($\theta_* = 1$)
(2) $OOH^* + H^+/e^- + \rightarrow H_2O_2$	$\alpha = \beta_2 + 1 - \theta_{OOH}$	40 ($\theta_* = 1$)

*Final mechanism would still be susceptible to changes due to OH adsorbed from water. A more accurate analysis would include OH in the site balance.

Table 4-3 Apparent transfer coefficients and corresponding zero adsorbate coverage and 1/3 OH coverage Tafel slopes for a variety of mechanism with potential RLS's.

4.7 References

1. Damjanovic, A. & Brusic, V. Electrode kinetics of oxygen reduction on oxide-free platinum electrodes. *Electrochimica Acta* **12,** 615 (1967).

2. Sepa, D. B., Vojnovic, M. V & Damjanovic, A. Reaction intermediates as a controlling factor in the kinetics and mechanism of oxygen reduction at platinum-electrodes. *Electrochimica Acta* **26,** 781–793 (1981).

3. Wang, J. X., Markovic, N. M. & Adzic, R. R. Kinetic analysis of oxygen reduction on Pt(111) in acid solutions: Intrinsic kinetic parameters and anion adsorption effects. *J. Phys. Chem. B* **108,** 4127–4133 (2004).

4. Wang, J. X., Zhang, J. L. & Adzic, R. R. Double-trap kinetic equation for the oxygen reduction reaction on Pt(111) in acidic media. *J. Phys. Chem. A* **111,** 12702–12710 (2007).

5. Wang, J. X., Uribe, F. A., Springer, T. E., Zhang, J. & Adzic, R. R. Intrinsic kinetic equation for oxygen reduction reaction in acidic media: the double Tafel slope and fuel cell applications. *Faraday Discussions* **140,** 347–362 (2009).

6. Blizanac, B. B., Ross, P. N. & Markovic, N. M. Oxygen reduction on silver low-index single-crystal surfaces in alkaline solution: Rotating ring Disk(Ag(hkl)) studies. *J. Phys. Chem. B* **110,** 4735–4741 (2006).

7. Gasteiger, H. A., Markovic, N. M., Ross, P. N. & Cairns, E. J. Temperature-Dependent Methanol Electro-Oxidation on Well-Characterized Pt-RuAlloys. *J. Electrochem. Soc.* **141,** 1795–1803 (1994).

8. Gojkovic´, S. L., Vidakovic´, T. R. & Durovic´, D. R. Kinetic study of methanol oxidation on carbon-supported PtRu electrocatalyst. *Electrochimica Acta* **48,** 2614–3607 (2003).

9. Markovic, N. M., Gasteiger, H. A., Grgur, B. N. & Ross, P. N. Oxygen reduction reaction on Pt(111): effects of bromide. *J. Electroanalytical Chem.* **467,** 157 (1999).

10. Markovic, N. M., Schmidt, T. J., Stamenkovic, V. R. & Ross, P. N. Oxygen Reduction Reaction on Pt and Pt Bimetallic Surfaces: A Selective Review. *Fuel Cells* **1,** 105–116 (2001).

11. Lynggaard, H., Andreasen, A., Stegelmann, C. & Stoltze, P. Analysis of simple kinetic models in heterogeneous catalysis. *Progress in Surface Science* **77,** 71–137 (2004).

12. Bligaard, T. *et al.* On the compensation effect in heterogeneous catalysis. *J. Phys. Chem. B* **107,** 9325–9331 (2003).

13. Stoltze, P. Surface science as the basis for the understanding of the catalytic synthesis of ammonia. *Physica Scripta* **36,** 824–864 (1987).

14. Gasteiger, H. A., Kocha, S. S., Sompalli, B. & Wagner, F. T. Activity benchmarks and requirements for Pt, Pt-alloy, and non-Pt oxygen reduction catalysts for PEMFCs. *Applied Catalysis B: Environmental* **56,** 9–35 (2005).

15. Borup, R. *et al.* Scientific aspects of polymer electrolyte fuel cell durability and degradation. *Chemical Reviews* **107,** 3904–3951 (2007).

16. Stamenkovic, V. R., Schmidt, T. J., Ross, P. N. & Markovic, N. M. Surface composition effects in electrocatalysis: Kinetics of oxygen reduction on well-defined Pt3Ni and Pt3Co alloy surfaces. *J. Phys. Chem. B* **106,** 11970–11979 (2002).

17. Murthi, V. S., Urian, R. C. & Mukerjee, S. Oxygen reduction kinetics in low and medium temperature acid environment: Correlation of water activation and surface properties in supported Pt and Pt alloy electrocatalysts. *J. Phys. Chem. B* **108,** 11011–11023 (2004).

18. Markovic, N. M., Gasteiger, H. A. & Ross, P. N. Oxygen Reduction on Platinum Low-Index Single-Crystal Surfaces in Sulfuric Acid Solution: Rotating Ring-Pt(hkl) Disk Studies. *J. Phys. Chem. C* **99,** 3411–3415 (1995).

19. Markovic, N. M., Gasteiger, H. & Ross, P. N. Kinetics of oxygen reduction on Pt(hkl) electrodes: Implications for the crystallite size effect with supported Pt electrocatalysts. *J. Electrochem. Soc.* **144,** 1591 (1997).

20. Grgur, B. N., Markovic, N. M. & Ross, P. N. Temperature-dependent oxygen electrochemistry on platinum low-index single crystal surfaces in acid solutions. *Can. J. Chem* **75,** 1465–1471 (1997).

21. Lima, F. H. B. *et al.* Catalytic activity-d-band center correlation for the O-2 reduction reaction on platinum in alkaline solutions. *J. Phys. Chem. C* **111,** 404–410 (2007).

22. Schmidt, T. J., Ross, P. N., Markovic, N. M., Division, M. S. & Berkeley, L. Temperature dependent surface electrochemistry on Pt single crystals in alkaline electrolyte. 400–406 (2003). doi:10.1039/b208322a

23. Paulus, U. A., Schmidt, T. J., Gasteiger, H. A. & Behm, R. J. Oxygen reduction on a high-surface area Pt/Vulcan carbon catalyst: a thin-film rotating ring-disk electrode study. *J. Electroanalytical Chem.* **495,** 134–145 (2001).

24. Paulus, U. A. *et al.* Oxygen reduction on high surface area Pt-based alloy catalysts in comparison to well defined smooth bulk alloy electrodes. *Electrochimica Acta* **47,** 3787–3798 (2002).

25. Faguy, P. W., Marinković, N. S. & Adzic, R. R. An in Situ Infrared Study on the Effect of pH on Anion Adsorption at Pt(111) Electrodes from Acid Sulfate Solutions. *Langmuir* **12,** 243–247 (1996).

26. Strmcnik, D. *et al.* Enhanced electrocatalysis of the oxygen reduction reaction based on patterning of platinum surfaces with cyanide. *Nature Chemistry* **2,** 880–885 (2010).

27. Clouser, S. J., Huang, J. C. & Yeager, E. Temperature-dependence of the tafel slope for oxygen reduction on platinum in concentrated phosphoric-acid. *J. Appl. Electrochem.* **23,** 597–605 (1993).

28. Sepa, D. B., Vojnovic, M. V, Vracar, L. M. & Damjanovic, a. Different views regarding the kinetics and mechanisms of oxygen reduction at pt and pd electrodes. *Electrochimica Acta* **32,** 129–134 (1987).

29. Tarasevich, M. R. No Title. *Elektrokhimiya* **9,** 599 (1973).

30. Markovic, N. M. & Ross, P. N. Surface science studies of model fuel cell electrocatalysts. *Surface Science Reports* **45,** 117–229 (2002).

31. Nørskov, J. K. *et al.* Origin of the overpotential for oxygen reduction at a fuel-cell cathode. *J. Phys. Chem. B* **108,** 17886–17892 (2004).

32. Stamenkovic, V. R. *et al.* Changing the activity of electrocatalysts for oxygen reduction by tuning the surface electronic structure. *Angew. Chem. Int. Ed.* **45,** 2897–2901 (2006).

33. Greeley, J. *et al.* Alloys of platinum and early transition metals as oxygen reduction electrocatalysts. *Nature Chemistry* **1,** 552–556 (2009).

34. Jinnouchi, R., Kodama, K., Hatanaka, T. & Morimoto, Y. First principles based mean field model for oxygen reduction reaction. *Phys. Chem. Chem. Phys.* **13,** 21070–21083 (2011).

35. Shao, M., Liu, P. & Adzic, R. R. Superoxide Anion is the Intermediate in the Oxygen Reduction Reaction on Platinum Electrodes. *J. Am. Chem. Soc.* **128,** 7408–7409 (2006).

36. Kunimatsu, K., Toda, T., Tryk, D., Uchida, H. & Watanabe, M. In situ ATR-FTIR study of oxygen reduction at the Pt/Nafion interface. *Phys. Chem. Chem. Phys.* **12,** 621–629 (2010).

37. Tripković, V., Skúlason, E., Siahrostamia, S., Nørskov, J. K. & Rossmeisl, J. The Oxygen Reduction Reaction Mechanism on Pt(111) from Density Functional Theory Calculations. *Electrochimica Acta* **55,** 7975–7981 (2010).

38. Bard, A. J. & Faulkner, L. R. *Electrochemical Methods: Fundamentals and Applications*. (John Wiley & Sons, Inc., 2001).

39. Bockris, J. O. & Nagy, Z. Symmetry Factor and Transfer Coefficient - Source of Confusion in Electrode Kinetics. *J. Chem. Ed.* **50,** 839–843 (1973).

40. Parsons, R. General equations for the kinetics of electrode processes. *Trans. Faraday Soc.* **47,** 1332–1344 (1951).

41. Bockris, J. O. Modern aspects of electrode kinetics. *Annu. Rev. Phys. Chem* **5,** 477–500 (1954).

42. Mauser, H. Zur Berechnung der Stationaren Strom-Spannungskurve Eines Systems Einfacher Folgereaktionen. *Z. Elektrochem.* **62,** 419–425 (1958).

43. Verdaguer, A., Sacha, G. M., Bluhm, H. & Salmeron, M. Molecular structure of water at interfaces: Wetting at the nanometer scale. *Chemical Reviews* **106,** 1478–1510 (2006).

44. Clay, C., Haq, S. & Hodgson, A. Hydrogen Bonding in Mixed OH+H2O Overlayers on Pt(111). *Phys. Rev. Lett.* **92,** 46102 (2004).

45. Feibelman, P. J. Partial dissociation of water on Ru(0001). *Science* **295,** 99–102 (2002).

46. Ireta, J., Neugebauer, J. & Scheffler, M. On the Accuracy of DFT for Describing Hydrogen Bonds: Dependence on the Bond Directionality. *J. Phys. Chem. A* **108,** 5692 (2004).

47. Willard, A. P., Reed, S. K., Madden, P. A. & Chandler, D. Water at an electrochemical interface—a simulation studytle. *Faraday Discussions* **141,** 423–441 (2009).

48. Stamenkovic, V. R. *et al.* Improved oxygen reduction activity on Pt3Ni(111) via increased surface site availability. *Science* **315,** 493–497 (2007).

49. Stamenkovic, V. R. *et al.* Trends in electrocatalysis on extended and nanoscale Pt-bimetallic alloy surfaces. *Nature Materials* **6,** 241–247 (2007).

50. Mukerjee, S., Srinivasan, S., Soriaga, M. P. & Mcbreen, J. Role of structural and electronic-properties of pt and pt alloys on electrocatalysis of oxygen reduction - an in-situ xanes and exafs investigation. *J. Electrochem. Soc.* **142,** 1409–1422 (1995).

Chapter 5: Comparative Kinetic Analysis of Electrochemical Oxygen Reduction on Silver and Platinum Electrodes

Ag-based electrode oxygen reduction reaction (ORR) catalysts are a potentially viable alternative to using Pt based catalysts for alkaline fuel cells. This chapter provides a comparative study of the ORR kinetic parameters in alkaline environment, using cyclic voltammetry (CV) and rotating disk electrode (RDE) kinetic measurements to compare the rates on each material and how these rates vary as a function of potential and adsorbate coverage. The apparent transfer coefficient and reaction orders with respect to hydroxyl ion and oxygen partial pressure are found to be consistent with a microkinetic model in which the first electron transfer to molecular oxygen is rate limiting. However, we find that in contrast to Pt, where changes in the rate parameters correlate well to adsorbate coverage on the surface, a very weak relation exists between adsorbate coverage and changes in the kinetics on Ag. This points to a strong role of undercoordinated sites, which can become poisoned at lower potential than the more well-coordinated surface facets. Thus for Ag, moving in the direction of stronger binding should lead to higher ORR activity by increasing TOF's on the more predominant surface facets, whereas Pt suffers from poisoning of essentially all sites and can only be made more active by moving to compositions with weaker affinity toward oxygen.

5.1 Introduction

Developing highly active catalysts for the electrochemical oxygen reduction reaction (ORR) in alkaline environments, $O_2 + 2H_2O + 4e^- \rightarrow 4OH^-$, has great potential value in advancing low-temperature fuel cell technology toward large-scale implementation. Current state-of-the-art ORR electro-catalysts are generally expensive nanoparticle alloys of Pt, which is the most active pure-element ORR catalyst in terms of active-site turnover frequency (TOF) and the only metal that is both highly active and stable in common acid-electrolyte cells.[1] Ag, which is less active on a TOF basis but still cost-competitive, is stable in alkaline cells, which are quickly becoming a technologically feasible alternative to acidic cells due to the development of robust hydroxide conducting membranes.[2,3] Modification of Ag through compositional (alloying) and/or morphological engineering may have the potential to generate a viable Pt-free fuel cell electro-catalyst. However, the design criteria necessary to optimize the activity of Ag are still poorly defined. This contribution offers a comparative study of the ORR kinetic behavior on Ag and Pt electrodes in alkaline environments, with a focus on confirming which processes limit the rate and how to improve it. We use polycrystalline disk electrodes, which represent a useful model system for real dispersed nanoparticle catalysts, as they possess a heterogeneity of surface facets, but are not subject to interference by support materials or internal transport variations.

While oxygen reduction is a fairly well studied reaction, there still remains a debate over which steps(s) limit the rate, and how they may differ across materials and conditions. For reasons we will delve into shortly, a number of authors have

proposed that the limiting step on Pt is the transfer of the first electron to the O_2 molecule. Conversely, some argue that on Pt, removal of hydroxide groups from the surface limits the rate,[4,5] and it is known that alloys with weaker OH binding (e.g. Pt/Ni, Pt/Co, Pt/Fe) exhibit higher ORR activity than pure Pt.[6–10] On Ag, the ORR is generally believed to be limited by the initial electron transfer to activate O_2,[11,12] but little work has been done to confirm and exploit this by way of designing enhanced morphologies or compositions. Recently we proposed that the conflicting viewpoints in the case of Pt may be reconciled in light of a model in which high adsorbate coverages are not the result of slow desorption but rather are the result of equilibrium that is driven by the high concentration of water in the surrounding environment.[13] A tradeoff exists between the intrinsic TOF of an active site and the number of sites available to perform the reaction, meaning a material with lower ability to activate O_2 may still yield a higher rate due to coverage effects. This was framed in terms of a simple microkinetic model, which illustrated that the operative reaction mechanism will result in easily-predictable apparent kinetic parameters.

In Figure 5-1, we plot several representative sets of ORR rate data (measured current vs. potential), measured on Ag and Pt electrodes at two different pHs. Ordinarily, a linear relationship is expected between electrode potential and the log of the rate—i.e. most simple reactions follow the Tafel equation: $E - E_{eq} = a + b\log(i)$, where i is the measured current, a and b are constants, E and E_{eq} are the working potential and equilibrium potential respectively. It is thus also expected that the i vs. E curve should shift proportionally to changes in the equilibrium potential of a reaction. In Figure 5-1, it can be seen that the ORR follows different

apparent (Tafel-type) rate laws in different operating regimes. The slope of the plot shifts with potential, and the variation in rate with respect to pH is also not constant. Such non-ideal behavior is not uncommon for complex heterogeneous reactions that feature multiple elementary steps,[14] including a number of electrochemical processes involving multiple electron transfers.[15–18]

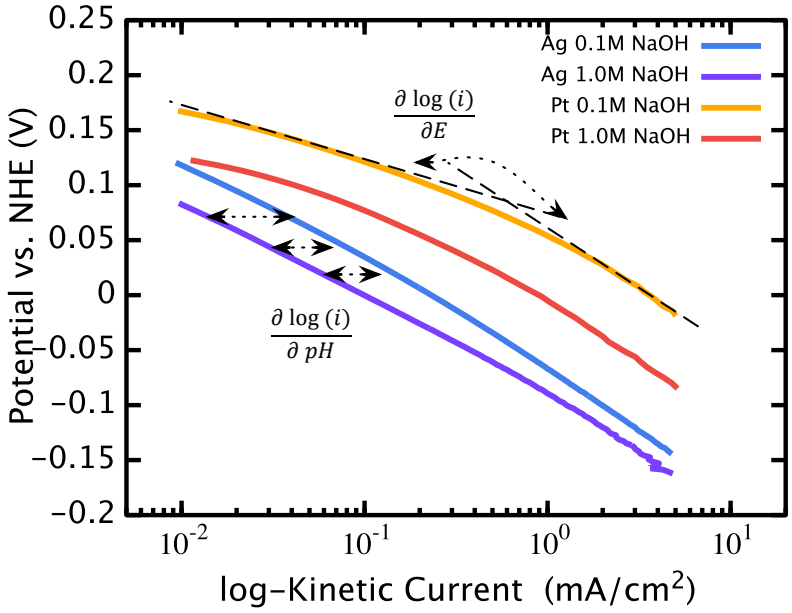

Figure 5-1: Examples of potential-dependent variation of Tafel slope and pH-dependence for ORR on polycrystalline Ag and Pt electrodes. All data collected in O_2-saturated electrolyte at 10mV/s using a rotating disk electrode at 1600rpm.

A number of apparent kinetic features of the ORR have been documented in prior literature, though focus has primarily been directed on the potential-dependence of the kinetics on Pt electrodes in acidic electrolytes, and the kinetic behavior is still not well interpreted in terms of elementary step mechanisms. Nonetheless, it is established that in both acid and basic environments, the apparent ORR Tafel slope on Pt shifts from about 60mV/dec at low current densities to

roughly 120mV/dec at high current densities.[11,19,20] This behavior appears largely independent of the geometry of the Pt surface (i.e. various low-index single crystals and most nanoparticle samples show the same features).[21–25] Several authors proposed as early as the 1960s that the 120mV/dec slope could only be explained by a reaction limited by the first electron transfer[26] (based on derived rate laws); however, the origin of the shift at higher potentials was attributed to adsorbate-adsorbate repulsion modifying the activation barrier, which doubt has been cast upon since.[5,13] The pH dependence has been less thoroughly investigated, but a few studies have found a shifting dependence on OH^- concentration from about -1/2 order at low currents to 0 order at high currents.[27,28] In comparison the kinetic parameters of ORR on Ag are less definitively reproduced, although a number of works have at least provided rate data at fixed pH,[29,30] including a recent pair of studies characterizing the Tafel behavior of low-index Ag single crystals.[16,31] The low index facets of Ag all show slopes close to 120mV/dec except at very low current densities, where shifts to between 70-100mV/dec are seen, depending on the crystal facet. The pH-dependence is not agreed upon by the few works that have explored it in any depth.[32]

For the sake of confirming prior results and performing all measurements under the exact same conditions, we measure the rates on both materials under all conditions of interest in the present work. Below, we discuss possible elementary steps involved in the ORR and then briefly introduce our model of apparent kinetic parameters and discuss how changes in the apparent ORR Tafel slope, as well as changes in reaction orders with respect to reactants (hydroxyl ion concentration

and oxygen partial pressure) occur with potential-induced changes in adsorbate coverage. We then present our measurements of the apparent kinetics on both Ag and Pt. We show that in both cases the kinetics are consistent with a microkinetic depiction in which the rate-limiting step (RLS) is the transfer of the first electron to molecular oxygen at all operating potentials. Unlike Pt, on which shifts in the apparent kinetic parameters are highly correlated to shifts in adsorbate coverage, the apparent kinetics on Ag are qualitatively similar to Pt despite having a relatively clean surface. We propose that this indicates the rate on Ag is governed by undercoordinated sites, which begin to be occupied by site-blocking adsorbates at potentials where the majority surface facets are still vacant. Thus, different design criteria should be followed in attempting to improve the activity of each material. On Pt, active sites can only be freed by moving to less reactive alloy compositions and choosing morphologies dominated by highly coordinated facets. On Ag, stronger binding will make the low-index surface facets more reactive and likely increase the overall rate even if under-coordinated sites become poisoned in the process.

5.1.1 ORR Mechanism

The elementary steps involved in the ORR are still debated (and likely differ on many materials) but a number of recent discoveries have established some consensus on certain aspects of the reaction. Recent quantum chemical calculations probing the energy of possible surface intermediates[4,33–35] have indicated that oxygen is most likely adsorbed in the molecular state prior to dissociation on Pt. Ag is a less reactive metal and should also not dissociate O_2. Low operating

temperatures also make this the likely case. The O_2 molecule may then be activated by the initial reduction, which may be either an independent electron transfer, forming an adsorbed superoxide ion (O_2^-), or a concerted step involving coupled proton addition (abstraction from water in base) resulting in an adsorbed peroxyl (OOH) intermediate. In-situ infrared spectroscopy[36,37] supports the formation of O_2^- rather than OOH in basic environments. However, this is a trace species that is difficult to detect, and it likely decomposes very quickly in either case. A second reduction of superoxide could result in adsorbed OOH^-, which could desorb in the case of poorly selective electrode materials (peroxide is a very minor product on Pt and Ag) but must otherwise discharge an OH^- ion resulting in an adsorbed O. On the other hand, a neutral OOH could dissociate (forming adsorbed O and OH) or be reduced again, discharging OH^- and leaving behind O. In alkaline environment OH^- discharge is not proton-assisted (as is the case in acid, where the electrodes are at higher absolute potentials and water is the product), and thus we anticipate an OOH intermediate will in fact discharge an OH^- faster than it may dissociate to O and OH in a pure chemical step. After the discharge, atomic oxygen on the surface should have only one mechanistic pathway involving formation of OH and then OH^-.

In this analysis we will treat the pathways requiring a proton and electron transfer as concerted steps, but the analysis that follows may be easily adapted to other possibilities. We have previously shown a number of the forks in the possible reaction network will be indistinguishable from rate data alone, but will also be irrelevant for purposes of developing better catalysts. This is ultimately because any sequential quasi-equilibrated steps may be treated as one net reaction without

affecting the predicted rate. Based on the discussed above, we have chosen to analyze the ORR in terms of the following elementary steps, where '*' denotes a free active site:

(5) $O_2 + H_2O + e^- + * \rightarrow OOH^* + OH^-$
(6) $OOH^* + e^- \rightarrow O^* + OH^-$
(7) $O^* + H_2O + e^- \rightarrow OH^* + OH^-$
(8) $OH^* + e^- \rightarrow OH^- + *$

We explore the consequences of this mechanism under different rate-limiting scenarios and then compare to the observed kinetics in the following sections.

5.1.2 Apparent kinetic parameter analysis

For any electrode reaction, we may describe the rate with an apparent Tafel rate law, which we give in Equation (5.1). Here, N is the number of electrons transferred, F is Faraday's constant, k^0 is the prefactor, a_i is the thermodynamic activity of a given reactant, δ_i is the corresponding reaction order, $\Delta G^{0,\ddagger}$ is the free energy of activation at the reference potential (E^0), α is the transfer coefficient, R is the ideal gas constant, T is the absolute temperature, and ν is the stoichiometric number, signifying the number of times the RLS must occur for the overall reaction to occur. The constant coefficients may be lumped into to a single apparent prefactor but are shown here simply to delineate the relation between measured current and reaction rate, which are often used interchangeably.

$$|i| = \frac{N}{\upsilon} \mathrm{F} k^0 \cdot \prod [a_i]^{\delta_i} \cdot \exp\left(\frac{-\Delta G^{0,\ddagger} - \alpha F(E - E^0)}{RT}\right) \tag{5.1}$$

The defining kinetic parameters for a given reaction rate will be the free energy of activation, the reaction orders, and the lumped constant prefactor. The transfer coefficient, which carries identical information to the Tafel slope ($\frac{\partial E}{\partial\, log\,|i|} = -\frac{2.3RT}{\alpha F}$), describes how the activation energy changes with potential. As alluded to above, the transfer coefficient can display non-constant behavior in many circumstances, as can the reaction orders and prefactor.

As derived in Chapter 4, in cases where an electrochemical reaction rate is dominated by a single RLS and the remaining steps can be approximated by quasi-equilibrium, simple algebraic expressions for the apparent electro-kinetic parameters of the forward rate may be deduced from a proposed reaction mechanism. Under any moderate overpotential (>~100mV, where the reaction may be regarded as irreversible), the apparent transfer coefficient and reaction orders are given by Equations (4.15) and (4.17) respectively. The apparent prefactor is fixed by these parameters and thus not necessary to explicitly compute. We note the expressions assume that each electrochemical quasi-equilibrium process is governed by the Nernst equation and that adsorption is Langmuirian—i.e. no adsorbate-adsorbate interaction occurs so that enthalpies are constant.

$$\alpha = -\frac{RT}{F}\frac{\partial \ln|i|}{\partial E} = \beta n_e^{\ddagger} + \frac{1}{\nu}\sum_{RLS\text{reactants}} n_{e,i}^{f} + N_*^{\ddagger}\sum_{\text{Adsorbates}} n_{e,i}^{des}\,\theta_i \qquad (5.2)$$

$$\delta_i = \frac{\partial \ln|i|}{\partial \ln(a_i)} = \delta_i^0 + N_*^{\ddagger}\sum_j N_{i,j}^{des}\theta_j \qquad (5.3)$$

In Equation (4.15), the first term describes the sensitivity of the free energy of activation of the RLS to applied potential. It is given simply by the symmetry factor of the RLS (β, generally assumed to equal ½) multiplied by the number of electrons transferred in each turnover of the RLS ($n_e^{\ddagger}$). The second term describes the sensitivity of the formation energy of the reactants in the RLS to potential, and it is given by the number of electrons transferred to form the reactants participating in the RLS (n_e^{f}) divided by the stoichiometric number (ν). This can be interpreted as an increase in the activity of the reactants participating in the RLS due to the overvoltage, which affects the overall reaction rate by shifting any electrochemical (quasi)equilibria in which they participate. Finally, the third term gives the sensitivity of the free energy required to liberate active sites from adsorbed species, to the applied potential. It is given by the number of electrons transferred in the desorption process for each surface species ($n_{e,i}^{\mathrm{des}}$), multiplied by the respective coverage of each surface species and the number of sites involved in the RLS ($N_{*}^{\ddagger}$). This term arises because the rate of reaction is proportional to the number of free sites. The transfer coefficient changes with variation in the coverage of any site blocking species, whether it is a reactive intermediate or a spectator species whose coverage responds to potential.

In Equation (4.17), the apparent reaction order consists of a constant, δ_i^0, that is the stoichiometric coefficient of the species in the rate-limiting step, and a coverage term describing how changing the concentration of a species will alter the number of active sites and impact the rate. The coefficient in front of each adsorbate coverage ($N_{i,j}^{des}$) will equal the stoichiometric coefficient of the species of interest

(the species we are finding the reaction order for) involved in the net desorption reaction of each adsorbed species, and it will also be multiplied by the number of sites in the RLS, $N_{*}^{\neq}$.

In Table 4-2 we compile the apparent transfer coefficients and reaction orders dictated by Equations (4.15) and (4.17) for the proposed mechanism under different RLS scenarios. As is evident from the table, the apparent values will exhibit characteristic shifts as a function of adsorbate coverage on the electrode surface. By coupling measured rates with surface coverages measured using cycling voltammetry, we can assess the consistency of each possible RLS with the observed kinetics. For comparison with alternatives, we will refer the reader back to Table 4-3 in the previous chapter, but we believe the present elementary steps give the most likely elementary steps under alkaline conditions.

Apparent α if RLS	**Order wrt $[OH^-]$**	**Order wrt P_{O2}**
(1) $\alpha=\beta_1+\theta_{OH}+2\theta_O+3\theta_{OOH}$	$\delta_{OH}=-\theta_{OH}-2\theta_O-3\theta_{OOH}$	$\delta_{O2}=1$
(2) $\alpha=\beta_2+1+\theta_{OH}+2\theta_O-\theta_{OOH}$	$\delta_{OH}=-1-\theta_{OH}-2\theta_O+\theta_{OOH}$	$\delta_{O2}=1-\theta_{OOH}$
(3) $\alpha=\beta_3+2+\theta_{OH}-2\theta_O-\theta_{OOH}$	$\delta_{OH}=-2-\theta_{OH}+2\theta_O+\theta_{OOH}$	$\delta_{O2}=1-\theta_O-\theta_{OOH}$
(4) $\alpha=\beta_4+3-3\theta_{OH}-2\theta_O-\theta_{OOH}$	$\delta_{OH}=-3+3\theta_{OH}+2\theta_O+\theta_{OOH}$	$\delta_{O2}=1-\theta_{OH}-\theta_O-\theta_{OOH}$

Table 5-1 Apparent transfer coefficients and apparent reaction orders with respect to OH^- concentration and O_2 pressure for each potential RLS of the proposed elementary step mechanism.

5.2 Results and Discussion

5.2.1 Electrode Surface Coverage

As indicated in Table 4-2, the apparent ORR kinetic parameters will vary with the coverage of adsorbates on the active sites of the electrode. In Figure 5-2(a-b), we show cyclic voltammograms collected on both the Ag and Pt electrodes in deaerated

electrolyte solutions with varying concentrations of NaOH (specific experimental details are given in Section 5.4). These show oxidative and reductive currents that correspond to adsorption and desorption of species from the aqueous environment on the metal surface. In the case of Ag, there are three features of interest. In the positive (anodic) scan direction, we first see a broad peak around -0.4V_{NHE}, followed by another broad feature at roughly 0.0V_{NHE} and a sharp oxidative feature rising up around 0.1-0.2V_{RHE}. Only the latter two features will impact the apparent ORR kinetics, for reasons we outline below.

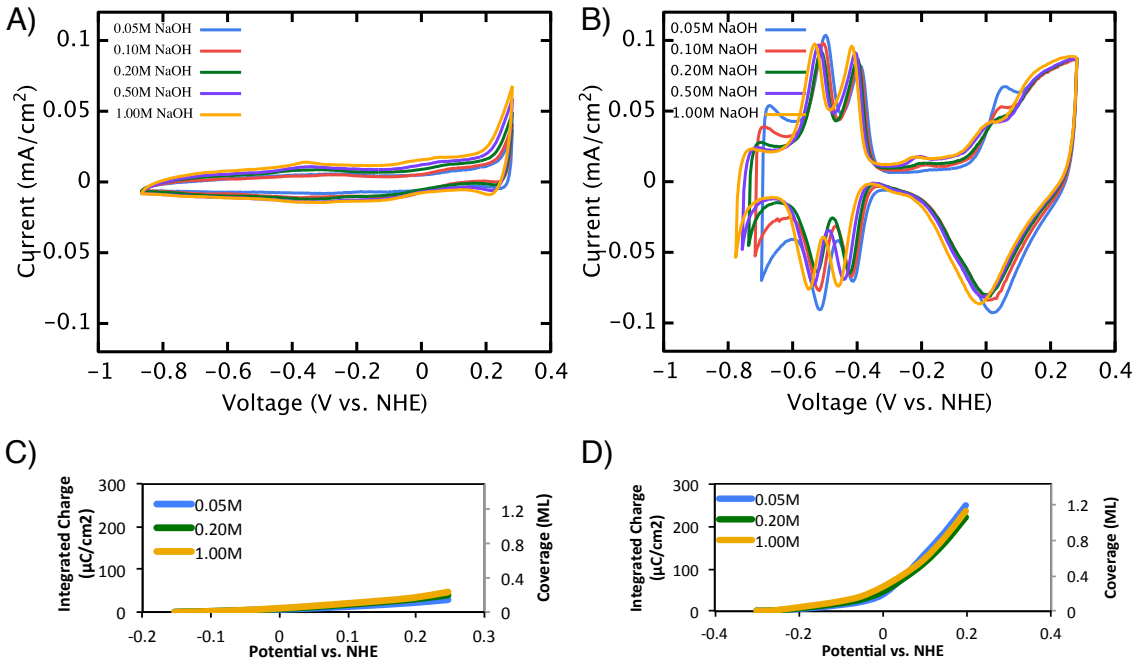

Figure 5-2: Cyclic voltammograms of Ag and Pt electrodes at varying pH and corresponding integrated oxidation charge. CV's for Ag (A) and Pt (B) were taken at 100mV/s in Ar-purged electrolyte with NaOH concentration varying between 0.05M and 1.0M. Charge associated with surface oxidation of Ag (C) and Pt (D) is obtained from integrating the CV's assuming a flat baseline at the narrowest point in the traces, representing the double-layer capacitance of the electrodes.

Previous authors have shown that the low-potential CV feature (-0.4V_{NHE}) on Ag single crystals is structure insensitive (identical for all low-index Ag facets). More specifically, when potentials are compared relative to the potential of zero-charge (PZC) for the (111), (100), and (110) crystal faces, the isotherms appear identical.[38] This is strong evidence that the peak is related to electrostatic interaction rather than covalent bonding. Furthermore, quantum chemical calculations do not support the ability of Ag to bind O or OH at these potentials,[39] and ex-situ XPS measurements of Ag electrodes emersed from solution under potential control have also shown that the species on the surface in this potential range is likely to be OH that retains its negative charge.[40] Thus, the peak most likely corresponds to a change in the differential capacitance of the metal surface as it crosses the PZC. We do not factor this coverage into the apparent kinetic parameters for two reasons: (i) electrostatically associated ions should be easily displaced by an atom forming a covalent bond with the surface, as would be the case in a catalyzed reaction, and (ii) the number of covered active sites associated with the peak would effectively be constant at the much higher potentials where ORR is measured—i.e. the derivative of sites with respect to potential would not cause measurable changes in current.

The higher two oxidative features in the CV of Ag are attributable to formation of a surface oxide layer. Comparison to single crystal data[16,38] would suggest that the smaller feature around 0.0V_{NHE} is related to oxidation of (110) and/or (100) facets (these show overlap), while the sharper current rise at 0.2V is related to oxidation of the (111) facets. XPS measurements have indicated that the oxygen-containing species is each of these cases is atomic oxygen rather than OH.[41]

We observe a shift of roughly 60mV per pH unit in these features, which is consistent with changes in the equilibrium potential for the surface oxidation reaction: $2OH^- + * = O* + 2e^- + H_2O$.

In contrast to Ag, the CV for Pt in Figure 5-2 shows much more distinct features due to higher reactivity toward water. The features are well-characterized in literature and were also discussed in Chapter 4 of this work. Briefly, we note that the low-potential peak corresponds to adsorption and desorption of a monolayer of hydrogen, while the higher potential features are related to oxidation of the various surface facets. Around $-0.3V_{NHE}$, the narrow region of the CV corresponds to pure capacitive current with no covalently adsorbed species, and at higher potential we see oxidation of the surface. While it is known that on Pt(111), adsorption of OH and a transition to coverage by atomic oxygen are well-resolved CV features, other low-index facets of Pt exhibit overlap in the initial OH adsorption and transition to a surface oxide.[42–44] Thus we simply see a broad oxidative current in the high potential region.

In Figure 5-2(c-d) we show integrated charges associated with the oxidation of each surface based on the CV's at various potential. For purposes of analysis using the kinetic parameters of Table 4-2, we will not assume any identity (O, OH, or OOH) for the adsorbates causing surface oxidation, and in fact we will later show that in the specific cases of ORR on Ag and Pt, the apparent kinetics are actually identical for a fixed amount of oxidative charge passed. Before moving to analyze the apparent kinetics, it is also important to note that while polycrystalline materials do have heterogeneity in surface structure and adsorbates may react with different

sites under different conditions, we will perform the present analysis as a mean field approximation. In most catalytic processes, the turnover frequency will be dominated by active sites with the most optimal geometry and electronic structure for the transformation in question. This means that either one type of active site will generally be relevant, or that in cases where multiple sites are active, it is because they have similar reactivity. Thus the active sites will also tend to become poisoned by adsorbates under similar conditions, and it is reasonable to treat the active sites as a single entity. If highly coordinated terrace sites contribute heavily to the activity, the CV-estimated site coverages should correlate well with total active site coverage, while underestimation of coverage effects may point to high activity of minority sites (e.g. steps and edges).

5.2.2 Apparent Tafel Slopes

In Figure 5-3(a and c), we show the apparent Tafel slopes measured for the ORR on Ag and Pt in O_2-saturated NaOH solution at several pHs. All rates were measured using the rotating disk electrode (RDE) method, and the RDE polarization curves and corresponding Tafel plots are shown in Figure 5-3(b and d). We note that the activity measurements are normalized to the solubility of O_2 in a given concentration of NaOH, as this parameter does vary significantly (about 50%) over the conditions studied (full experimental and data analysis details outlined in Section 5.4). On Ag, the Tafel slope shifts from ~120mV/dec at large overpotential to ~75mV/dec at small overpotential, with minor differences related to pH. Pt behaves in a qualitatively similar manner, but with a stronger shift to ~60mV/dec.

Inspecting Table 4-2, it is clear that the only possible RLS that can yield Tafel slopes larger than 60mV/dec is the initial reduction of O_2 (at room temperature, the slope is essential $60/\alpha$). All other steps require transfer coefficients greater than one, and these only increase with coverage.

In order to assign quantitative theoretical values for the Tafel slope on each surface based on adsorbate coverage, we must refer back to the integrated cyclic voltammograms from Figure 5-2(c-d). While there may be some uncertainty in whether the integrated charges are associated with surface oxidation by O or OH (particularly for Pt), we note that for any mechanism in which both O and OH coverages are controlled by quasi-equilibrium, the net influence on the [OH^-] coverage should be independent of the identity of the adsorbate. If we define an adsorption pseudo-capacitance of a surface, here labeled Γ, to be the charge transferred per unit area (A) by a monolayer of adsorbate assuming 1 electron per site, we can infer the relationship between the integrated charge (Q) and adsorbate coverage given in Equation (5.4). Consequently for the proposed mechanism, limited by Step 1, $\alpha=\beta_1 - Q/\Gamma A$.

$$Q = \frac{1}{\Gamma A}\int \frac{i}{(dE/dt)}dE = \theta_{OH} + 2\theta_O + 3\theta_{OOH} \tag{5.4}$$

We do note that as discussed in the previous chapter, it is known that on Pt(111), well-ordered OH-H_2O networks can form and increase site coverage without a corresponding oxidative current. However, the extent of water co-adsorption is poorly characterized on the other low-index facets of Pt. Thus we do not attempt to

quantify the effect to refine the model, but simply call attention to a small source of possible error. We plot the model-predicted Tafel slope assuming limitation by Step 1 in Figure 5-3 for each electrode material. Since the coverage at a chosen potential only varies a small degree with pH, we simply use the average integrated charge across pHs to obtain the values.

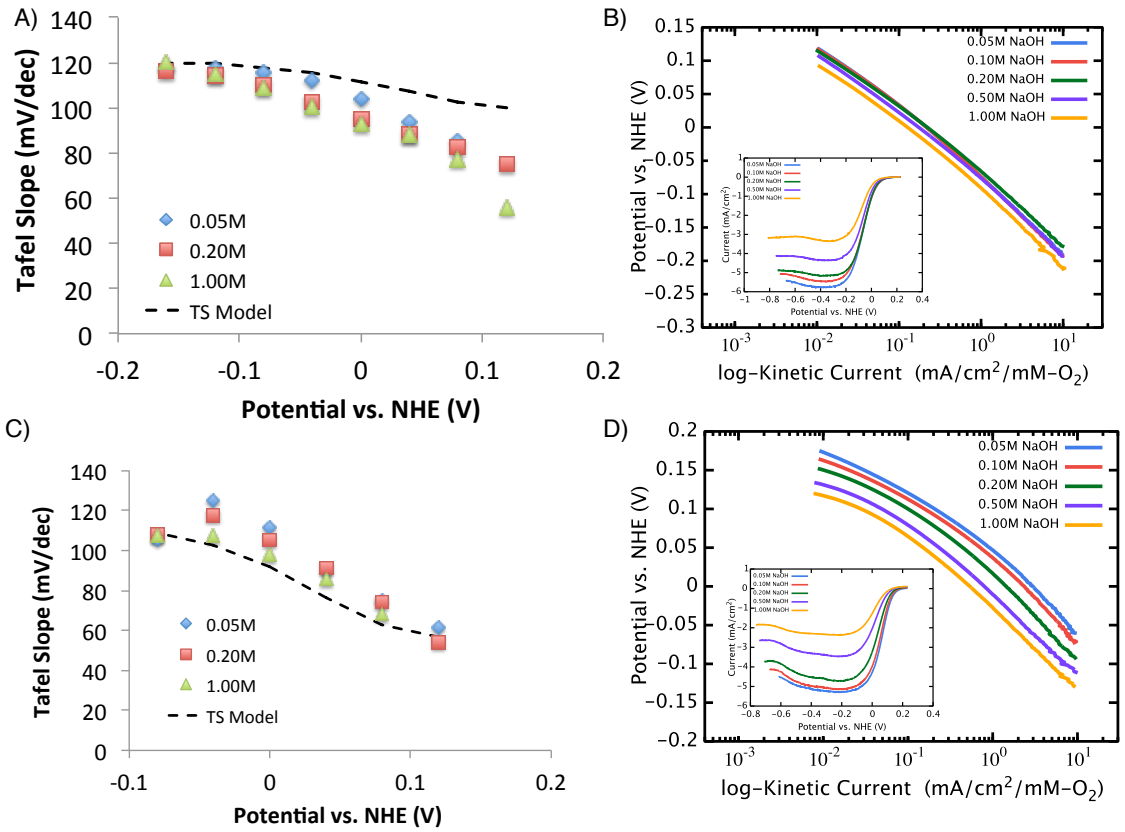

Figure 5-3: Apparent Tafel slope vs. model prediction on Ag and Pt. Slopes for Ag (A) and Pt (C) are taken over 40mV intervals using the Tafel plots obtained in (B) and (D) using the RDE. All data was taken in O_2 saturated NaOH solutions at 10mV/s and 1600rpm.

While the observed Tafel slopes qualitatively establish that the rate of the ORR must be limited by O_2 activation on both Ag and Pt, there exists a significant

deviation between the predicted and measured slope on Ag at high potentials. This is a likely indication that we underestimate the coverage of active sites due to the approximation of normalizing the integrated charge to the adsorption pseudo-capacitance of the electrode, rather than the actual number of active sites. If we appeal to prior work on single crystals, it is known that the Ag(110) surface (a more corrugated facet than the (100) or (111)) exhibits about 3 times the activity of the (111) and (100) facets (in the clean surface regime), which are very close in activity to each other.[16] This is in contrast to Pt, where the (111) terraces are the most active[20] and the model-estimated slopes match experiment well. Using the Ag single crystal activity numbers, a simple back-of-the-envelope estimate would dictate that if Ag(110) represented 10% of the electrode surface, it would contribute about 25% to the measured rate. We measure an oxidative charge of approximately 20$\mu C/cm^2$, or about 10% coverage (assuming a composite pseudo-capacitance of 200$\mu C/cm^2$) by the time the electrode reaches 0.1V_{NHE}. This could easily correspond to complete oxidation of (110) facets (pseudo-capacitance 135$\mu C/cm^2$) with the small additional coverage accumulating on more coordinated facets (likely (100) would follow). Such a scenario would drive the observed Tafel slope from the originally estimated 100mV/dec down to about 90mV/dec. Even this estimate falls short of observation, and in reality it is likely that step and edge sites play a significant role.

5.2.3 Apparent Reaction Orders

In Figure 5-4 we show the apparent ORR reaction orders for the Ag and Pt electrodes with respect to hydroxyl ion concentration in O_2-saturated, NaOH electrolytes. We first point out that on both materials, the [OH^-] reaction orders are fractional, and comparison to the values predicted in Table 4-2 clearly indicates that the only values consistent with this observation are those corresponding to limitation by the initial electron transfer (Step 1), where $\delta_{OH} \approx -\theta_{OH} - 2\theta_O$.

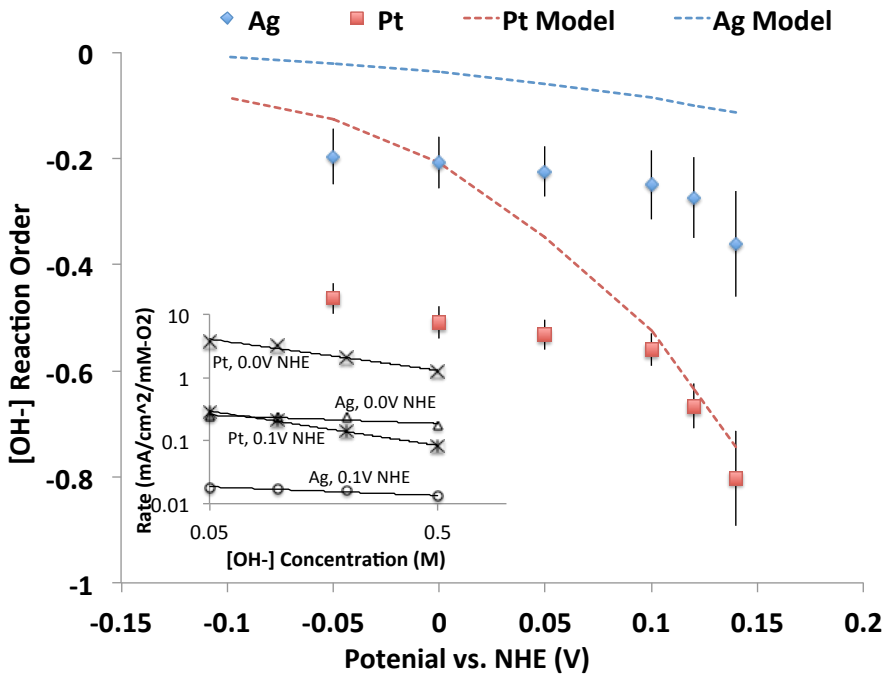

Figure 5-4: Reaction orders with respect to hydroxyl concentration on Ag and Pt. All orders are computed from the same data sets used in the Tafel slope measurements in Figure 5-3. Inset shows rate vs. concentration plots at fixed potentials used to compute the reaction order.

Comparing the reaction orders on the two metal surfaces, the same qualitative behavior is seen, and it is consistent with the changes observed in the

Tafel slopes. At high potentials the active sites begin to be poisoned by a high equilibrium coverage of adsorbates, and the apparent orders grow in magnitude. A marked quantitative difference occurs (as is to be expected) due to differences in the respective surface coverages of each electrode. However, the measured values in both cases do show significant deviations from those predicted by our simple theory. In the case of Ag, the reaction order shows a sharper growth than predicted, moving from -0.2 to -0.4, whereas only a slight shift to -0.1 is predicted. We believe the larger magnitude of the *shift* can be attributed to the role of undercoordinated site coverage, as discussed in the previous section. However, the absolute order of -0.2 on the adsorbate-free Ag surface, as well is the roughly -0.4 order on 'clean' Pt is more difficult to account for.

One possible explanation for the unexpected activity suppression at higher current densities is simply that of contamination. Transition-metal hydroxide impurities exist in most alkali salts, and the purest commercially available NaOH and KOH available (used in this work) still contain about 0.01ppm transition metal cations.[45] While these species should not be redox-active at the potentials of interest, they may exhibit a degree of equilibrium partitioning onto the surface, and such a poisoning effect would be more pronounced at higher electrolyte concentration. One recent report noted that in the case of Pt, CV peaks in alkali lose area over the course of a few dozen cycles and the initial measurable surface area is only stable for extended time under quiescent conditions (no stirring or bubbling in the solution).[45] We have utilized high-purity NaOH, but as ORR measurements require a slow scan rate to establish steady-state, as well as convection to the RDE,

contamination is somewhat inevitable. We note that one prior work exploring pH dependence of ORR in lower concentration regimes (down to pH 7 using supporting electrolytes for conductivity) found an OH reaction order close to zero on Pt at high current density.[27] We suspect that Ag, being a more noble metal, may be less susceptible to the contamination effect but that it may still be present. In the higher potential regime, the order wrt [OH^-] seems to agree well, and it may be possible that oxidation of the surface displaces weakly adsorbed interfering species.

In Figure 5-5, we show the apparent reaction order with respect to oxygen partial pressure (varied by mixing with argon in varying ratios) for the ORR in 0.1M NaOH as a function of potential. The figure shows an apparent order very near to 1 for both Ag and Pt across the whole range of potentials, with a small decrease at very large overpotential (more negative potentials, where the surface is expected to be clean). Comparison to Table 4-2 reveals that while an apparent order of 1 is expected for all rate limiting steps at large overpotential, an opposite trend would be expected in the small overpotential regime (where significant adsorbate coverage is present) if the rate were limited by either OH* removal or reduction of O* to OH* (step 3 or 4). On the other hand, in the case of a rate-limiting initial electron transfer to O_2 or rate-limiting OH^- discharge from OOH*, an order very close to 1 is expected. Taken together with the Tafel slopes and [OH^-] rate dependence, the PO_2 dependence is consistent with Step 1 being rate limiting. The deviation at large overpotential is not a source for major concern, and we suspect that due to the very low mass-transfer limitation on currents at low PO_2, the Koutecky-Levich

deconvolution scheme (see Section5.4) for calculating kinetic current is simply creating a small systematic error.

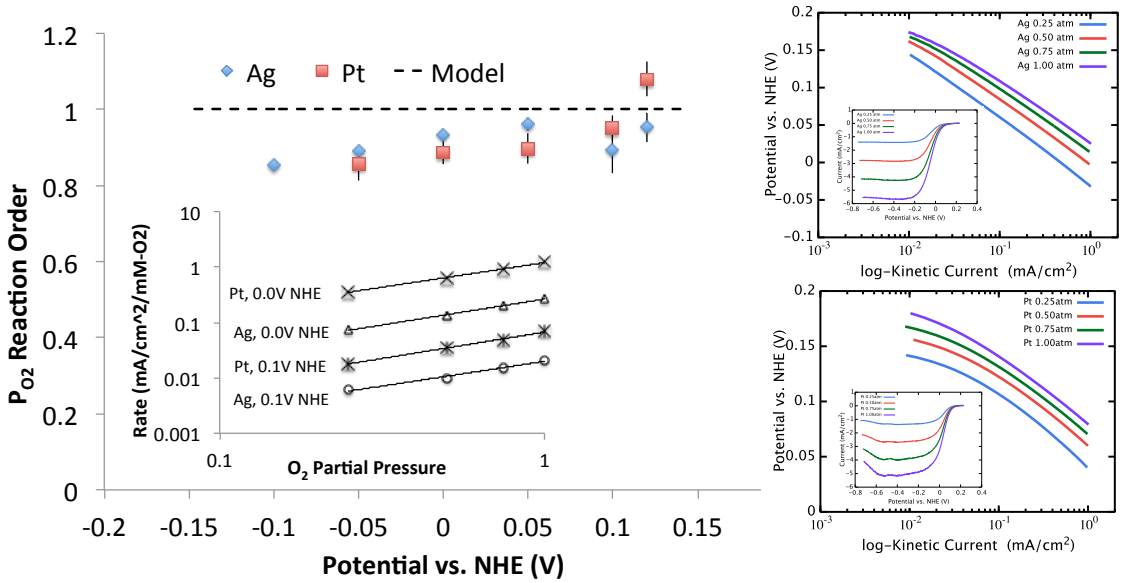

Figure 5-5: Reaction orders with respect to O_2 partial pressure on Ag and Pt. All measurements performed in 0.1M NaOH at 1600rpm bubbling varying ratios of O_2/Ar to the electrochemical cell. Inset shows rate vs. pressure plots at fixed potentials used to compute the reaction orders. Tafel plots at the right show the RDE data used to construct the inset plot.

5.3 Conclusions

The analysis above indicates that the measured reaction orders, Tafel slopes, and relative shifts in these parameters with adsorbate coverage are all consistent with an ORR mechanism limited by the initial activation and reduction of the O_2 molecule on both Ag and Pt surfaces. However the quantitative relation of these parameters to coverages estimated from the pseudocapacitances for each surface reveal that in the case of Ag, the most active sites are most likely undercoordinated sites, while on Pt the active sites are the terraces, which dominate the surface area.

Optimizing catalytic activity is a tradeoff between making a surface active enough to bind the reactant molecules, but not so reactive as to poison the active sites with product. The ORR is a relatively unique reaction in that it cannot be run without a very high concentration of product present (water). Thus, even though the rate-limiting step is activation of the reactant, it is possible to have a high coverage of intermediates blocking active sites. For Ag surfaces, the fact that the terraces are almost entirely unpopulated and under-coordinated sites play a major role means that moving in the direction of stronger binding should lead to higher ORR activity, as the TOF's on the predominant sites will begin to play a larger role—i.e. the under-coordinated sites will become poisoned, but the turnover rates on terraces will become higher. Alternatively, it may be possible to achieve significantly enhanced rates with extremely small Ag particles (on the order of 1nm), which would be terminated with many under-coordinated sites. Pt suffers from poisoning of essentially all sites and can only be made more active by moving to compositions with weaker affinity toward oxygen.

5.4 Experimental Details

Electrochemical measurements were performed at room temperature in an all-Teflon three-electrode cell (made in house) with a Gamry Instruments Reference 3000 potentiostat/galvanostat/FRA. The reference (Hg/HgO in 1M KOH, Radiometer Analytical) and counter electrodes (Pt wire, Alfa Aesar) were both in isolated compartments with long diffusion paths to the working electrode chamber.

Working electrodes were polished with 0.05μm alumina paste and sonicated in ultrapure water prior to use. These electrodes were put into a Teflon RDE housing, attached to a rotator (Pine) and inserted into the cell under potential control using a Pt wire dummy electrode, temporarily connected to the working electrode lead.

Electrolyte solutions of 0.1M NaOH were prepared from ultrapure water (18MΩ, Millipore) and Merck Suprapur NaOH-monohydrate. Uncompensated resistance was measured via the high frequency impedance at the end of each trial and was corrected for in the polarization curves. Cyclic voltammograms were taken in argon-purged solution, and rotating disk polarization curves were taken in O_2-saturated solution. O_2 and Ar were each passed through adsorbent columns to remove residual hydrocarbons, moisture, and oxygen in the case of Ar. For partial pressure measurements, the gases were mixed in varying ratios prior to bubbling into the cell using mass flow controllers. Each series of tests (pH or PO_2 variance) was carried out in a continuous fashion (changing the reactant concentration while cycling the same electrode) in order to remove variations in electrode roughness between tests. Thus for pH studies the cell was loaded with low-concentrations of NaOH and then more concentrated stock solutions were dripped in to raise the $[OH^-]$ concentration to the desired levels while the electrode was continuously cycled.

To determine kinetic current densities from ORR polarization curves, the Koutecky-Levich (KL) equation was used: $1/|i| = 1/|i_k| + 1/|i_L|$,[46] where, i_k is the kinetic current and i_L is the mass transfer limited current at very large overpotential. This relationship is ideally only used when i_k < ~½ i_L as it becomes prone to large error as the current approaches its limiting value. To study effects at

constant potential it was necessary in some cases to extrapolate kinetic currents from measured currents as high as $0.8i_L$ (generally when the O_2 concentration was low due to low PO_2 or low solubility in highly concentrated NaOH). For studies of [OH^-] reaction order, activities were normalized to O_2 solubility as calculated from the following equation, which has been confirmed for KOH solutions:[47] $\log S = \log[1.26\text{x}10^{-3}] - 0.1746C$, where S is the solubility of O_2 and C is the hydroxide concentration, both in mol/L.

5.5 References

1. Gasteiger, H. A., Kocha, S. S., Sompalli, B. & Wagner, F. T. Activity benchmarks and requirements for Pt, Pt-alloy, and non-Pt oxygen reduction catalysts for PEMFCs. *Applied Catalysis B: Environmental* **56,** 9–35 (2005).

2. Varcoe, J. R. & Slade, R. C. T. Prospects for Alkaline Anion-Exchange Membranes in Low Temperature Fuel Cells. *Fuel Cells* **5,** 187–200 (2005).

3. Deavin, O. I. *et al.* Anion-exchange membranes for alkaline polymer electrolyte fuel cells: comparison of pendent benzyltrimethylammonium- and benzylmethylimidazolium-head-groups. *Energy & Environmental Science* **5,** 8584 (2012).

4. Greeley, J. *et al.* Alloys of platinum and early transition metals as oxygen reduction electrocatalysts. *Nature Chemistry* **1,** 552–556 (2009).

5. Tripković, V., Skúlason, E., Siahrostamia, S., Nørskov, J. K. & Rossmeisl, J. The Oxygen Reduction Reaction Mechanism on Pt(111) from Density Functional Theory Calculations. *Electrochimica Acta* **55,** 7975–7981 (2010).

6. Stamenkovic, V. R., Schmidt, T. J., Ross, P. N. & Markovic, N. M. Surface composition effects in electrocatalysis: Kinetics of oxygen reduction on well-defined Pt3Ni and Pt3Co alloy surfaces. *J. Phys. Chem. B* **106,** 11970–11979 (2002).

7. Murthi, V. S., Urian, R. C. & Mukerjee, S. Oxygen reduction kinetics in low and medium temperature acid environment: Correlation of water activation and surface properties in supported Pt and Pt alloy electrocatalysts. *J. Phys. Chem. B* **108,** 11011–11023 (2004).

8. Stamenkovic, V. R. *et al.* Improved oxygen reduction activity on Pt3Ni(111) via increased surface site availability. *Science* **315,** 493–497 (2007).

9. Stamenkovic, V. R. *et al.* Trends in electrocatalysis on extended and nanoscale Pt-bimetallic alloy surfaces. *Nature Materials* **6,** 241–247 (2007).

10. Mukerjee, S., Srinivasan, S., Soriaga, M. P. & Mcbreen, J. Role of structural and electronic-properties of pt and pt alloys on electrocatalysis of oxygen reduction - an in-situ xanes and exafs investigation. *J. Electrochem. Soc.* **142,** 1409–1422 (1995).

11. Lima, F. H. B. *et al.* Catalytic activity-d-band center correlation for the O-2 reduction reaction on platinum in alkaline solutions. *J. Phys. Chem. C* **111,** 404–410 (2007).

12. Viswanathan, V., Hansen, H. A., Rossmeisl, J. & Nørskov, J. K. Universality in Oxygen Reduction Electrocatalysis on Metal Surfaces. *ACS Catalysis* **2,** 1654–1660 (2012).

13. Holewinski, A. & Linic, S. Elementary Mechanisms in Electrocatalysis: Revisiting the ORR Tafel Slope. *J. Electrochem. Soc.* **159,** H864–H870 (2012).

14. Chin, Y.-H. C., Buda, C., Neurock, M. & Iglesia, E. Reactivity of chemisorbed oxygen atoms and their catalytic consequences during CH4-O2 catalysis on supported Pt clusters. *J. Am. Chem. Soc.* **133,** 15958–78 (2011).

15. Wang, J. X., Uribe, F. A., Springer, T. E., Zhang, J. & Adzic, R. R. Intrinsic kinetic equation for oxygen reduction reaction in acidic media: the double Tafel slope and fuel cell applications. *Faraday Discussions* **140,** 347–362 (2009).

16. Blizanac, B. B., Ross, P. N. & Markovic, N. M. Oxygen reduction on silver low-index single-crystal surfaces in alkaline solution: Rotating ring Disk(Ag(hkl)) studies. *J. Phys. Chem. B* **110,** 4735–4741 (2006).

17. Gasteiger, H. A., Markovic, N. M., Ross, P. N. & Cairns, E. J. Temperature-Dependent Methanol Electro-Oxidation on Well-Characterized Pt-RuAlloys. *J. Electrochem. Soc.* **141,** 1795–1803 (1994).

18. Gojkovic´, S. L., Vidakovic´, T. R. & Durovic´, D. R. Kinetic study of methanol oxidation on carbon-supported PtRu electrocatalyst. *Electrochimica Acta* **48,** 2614–3607 (2003).

19. Schmidt, T. J., Stamenkovic, V. R., Ross, P. N. & Markovic, N. M. Temperature dependent surface electrochemistry on Pt single crystals in alkaline electrolyte - Part 3. The oxygen reduction reaction. *Phys. Chem. Chem. Phys.* **5,** 400–406 (2003).

20. Markovic, N. Oxygen reduction on platinum low-index single-crystal surfaces in alkaline solution: rotating ring diskPt (hkl) studies. *J. Phys. Chem. C* **100,** 6715–6721 (1996).

21. Markovic, N. M. *et al.* Effect of temperature on surface processes at the Pt(111)-liquid interface: Hydrogen adsorption, oxide formation, and CO oxidation. *J. Phys. Chem. B* **103,** 8568–8577 (1999).

22. Markovic, N. M., Gasteiger, H. & Ross, P. N. Kinetics of oxygen reduction on Pt(hkl) electrodes: Implications for the crystallite size effect with supported Pt electrocatalysts. *J. Electrochem. Soc.* **144,** 1591 (1997).

23. Grgur, B. N., Markovic, N. M. & Ross, P. N. Temperature-dependent oxygen electrochemistry on platinum low-index single crystal surfaces in acid solutions. *Can. J. Chem* **75,** 1465–1471 (1997).

24. Paulus, U. A., Schmidt, T. J., Gasteiger, H. A. & Behm, R. J. Oxygen reduction on a high-surface area Pt/Vulcan carbon catalyst: a thin-film rotating ring-disk electrode study. *J. Electroanalytical Chem.* **495,** 134–145 (2001).

25. Paulus, U. A. *et al.* Oxygen reduction on high surface area Pt-based alloy catalysts in comparison to well defined smooth bulk alloy electrodes. *Electrochimica Acta* **47,** 3787–3798 (2002).

26. Damjanovic, A. & Brusic, V. Electrode kinetics of oxygen reduction on oxide-free platinum electrodes. *Electrochimica Acta* **12,** 615 (1967).

27. Sepa, D. B., Vojnovic, M. V & Damjanovic, A. Reaction intermediates as a controlling factor in the kinetics and mechanism of oxygen reduction at platinum-electrodes. *Electrochimica Acta* **26,** 781–793 (1981).

28. Sepa, D. B., Vojnovic, M. V, Vracar, L. M. & Damjanovic, A. Different views regarding the kinetics and mechanisms of oxygen reduction at pt and pd electrodes. *Electrochimica Acta* **32,** 129–134 (1987).

29. Sleightholme, A. E. S., Varcoe, J. R. & Kucernak, A. R. Oxygen reduction at the silver/hydroxide-exchange membrane interface. *Electrochem. Comm.* **10,** 151–155 (2008).

30. Guo Junsong, A. H. D. C. & Chen, R. Improving Oxygen Reduction Reaction Activities on Carbon-Supported Ag Nanoparticles in Alkaline Solutions. *J. Phys. Chem. C* **114,** 4324–4330 (2010).

31. Blizanac, B. B., Ross, P. N. & Markovic, N. M. Oxygen electroreduction on Ag(111): The pH effect. *Electrochimica Acta* **52,** 2264–2271 (2007).

32. Sepa, D., Vojnovic, M. & A, D. Oxygen reduction at silver electrodes in alkaline solutions. *Electrochimica Acta* **15,** 1355 (1970).

33. Nørskov, J. K. *et al.* Origin of the overpotential for oxygen reduction at a fuel-cell cathode. *J. Phys. Chem. B* **108,** 17886–17892 (2004).

34. Stamenkovic, V. R. *et al.* Changing the activity of electrocatalysts for oxygen reduction by tuning the surface electronic structure. *Angew. Chem. Int. Ed.* **45,** 2897–2901 (2006).

35. Jinnouchi, R., Kodama, K., Hatanaka, T. & Morimoto, Y. First principles based mean field model for oxygen reduction reaction. *Phys. Chem. Chem. Phys.* **13,** 21070–21083 (2011).

36. Shao, M., Liu, P. & Adzic, R. R. Superoxide Anion is the Intermediate in the Oxygen Reduction Reaction on Platinum Electrodes. *J. Am. Chem. Soc.* **128,** 7408–7409 (2006).

37. Kunimatsu, K., Toda, T., Tryk, D., Uchida, H. & Watanabe, M. In situ ATR-FTIR study of oxygen reduction at the Pt/Nafion interface. *Phys. Chem. Chem. Phys.* **12,** 621–629 (2010).

38. Horswell, S. L. *et al.* A Comparative study of hydroxide adsorption on the (111), (110), and (100) faces of silver with cyclic voltammetry, ex situ electron diffraction, and in situ second harmonic generation. *Langmuir* **20,** 10970–10981 (2004).

39. Koper, M. T. M. & van Santen, R. A. Interaction of H, O and OH with metal surfaces No Title. *J. Electroanalytical Chem.* **472,** 126–136 (1999).

40. Lutzenkirchen-Hecht, D. & Strehblow, H. H. Surface analytical investigations of the electrochemical double layer on silver electrodes in alkaline media. *Electrochimica Acta* **43,** 2957–2968 (1998).

41. Savinova, E. R. *et al.* Structure and dynamics of the interface between a Ag single crystal electrode and an aqueous electrolyte. *Faraday Discussions* **121,** 181–198 (2002).

42. Markovic, N. M., Schmidt, T. J., Stamenkovic, V. R. & Ross, P. N. Oxygen Reduction Reaction on Pt and Pt Bimetallic Surfaces: A Selective Review. *Fuel Cells* **1,** 105–116 (2001).

43. Markovic, N. M. & Ross, P. N. Surface science studies of model fuel cell electrocatalysts. *Surface Science Reports* **45,** 117–229 (2002).

44. Bondarenko, A. S. *et al.* The Pt(111)/Electrolyte Interface under Oxygen Reduction Reaction Conditions: An Electrochemical Impedance Spectroscopy Study. *Langmuir* **27,** 2058–2066 (2011).

45. Subbaraman, R. *et al.* Origin of Anomalous Activities for Electrocatalysts in Alkaline Electrolytes. *J. Phys. Chem. C* **116,** 22231–22237 (2012).

46. Bard, A. J. & Faulkner, L. R. *Electrochemical Methods: Fundamentals and Applications*. (John Wiley & Sons, Inc., 2001).

47. Davis, R. E., Horvath, G. L. & Tobias, C. W. The solubility and diffusion coefficient of oxygen in potassium hydroxide solutions. *Electrochimica Acta* **12,** 287–297 (1967).

Chapter 6: High Performance Ag-Co Alloy Catalysts for Electrochemical Oxygen Reduction

Electrochemical oxygen reduction, $O_2+4H^++4e^-\rightarrow 2H_2O$, is the limiting half-reaction for low-temperature hydrogen fuel cells. Currently, costly Pt-based electro-catalysts are used to facilitate the reaction at adequate rates, making fuel cell devices prohibitively expensive. Herein we demonstrate the design of relatively inexpensive Ag-Co surface alloy nanoparticle electro-catalysts for oxygen reduction, with equivalent area-specific activity to commercial Pt-nanoparticles at 0.8V (reversible hydrogen electrode scale), and more than five-fold improved performance over pure Ag nanoparticles. The Ag-Co materials were identified with quantum chemical calculations and synthesized with a novel technique that generates a surface alloy, despite the bulk immiscibility of the constituent materials. Characterization studies show that the origin of the activity improvement comes from a ligand effect, in which Co perturbs the Ag surface sites and improves their inherent activity. The observed enhancements in the ORR activity of Ag through alloying represent an important step towards making fuel cell technology viable.

6.1 Introduction

Effective catalysis of the oxygen reduction reaction, $O_2+4H^++4e^-\rightarrow 2H_2O$ (ORR), remains a major contemporary technological hurdle. Low-temperature proton-exchange membrane fuel cells (PEMFCs) are a promising technology for efficient power delivery in transportation and mobile devices, but their commercialization is hampered by the slow rate of the ORR, which requires costly electrocatalysts with high Pt content to achieve adequate power densities. Typical Pt nanoparticle catalysts represent about half the cost (projected by the US DOE) of an automotive PEMFC stack required to deliver ~ 80 KW, accounting for economies of scale.[1] Even current state-of-the-art Pt-alloy electrocatalysts, which achieve about twice the ORR activity per gram of Pt-group metal (PGM), still contribute ~35% to equivalent-power stack costs. Furthermore, the long-term stability of current state-of-the-art catalysts still falls short of the DOE 5000h lifetime target (to 10% voltage loss) for most transportation applications.[1,2] With current projections, including balance-of-plant costs, it has been determined that a viable Pt-based catalyst needs to exhibit at least a four-fold enhancement over pure Pt in PGM mass-activity, with similar or better long-term stability.[1–4] Alternatively if a Pt-free material—a so-called "costless catalyst"—can be utilized, activity targets can be decreased about an order of magnitude (on a volumetric basis) before reaching electrode thickness limits for effective mass transport and a break-even point in cost due to use of larger cell components.[2–5]

One of the fundamental reasons for the general lack of success in identifying viable alternatives to Pt-based ORR catalysts is the issue of stability. Since the majority of metals are unstable in the acidic oxidative environment of a PEMFC cathode, very few materials can be considered. On the other hand, in alkaline environments, a number of alternative electrode material candidates are stable. This is illustrated in a Pourbaix diagram in Figure 6-1, where equilibrium potentials for the most thermodynamically favorable oxidation process of a variety of metals are plotted as a function of pH (assuming metal ion activities of either unity or the saturated concentration if less).[6] The Pourbaix diagram shows that Ag stands out as having superior electrochemical stability in base. Another appealing feature of Ag is that at a cost of ~$1/g (roughly 50 times cheaper than Pt),[7] it is comparatively an almost costless catalyst. The main deficiency of Ag is that it exhibits an area-specific activity roughly an order of magnitude lower than Pt—i.e. the surface Ag atoms are up to 10 times less active than Pt atoms.[8–13] We note that in base Pt retains superior ORR activity and show quantitatively similar performance as in acid.[14] Since supported Ag nanoparticles contain a density of active surface sites per volume of catalyst that is essentially identical to that of supported Pt nanoparticle catalysts, the volumetric rates achievable with Ag—the rates per volume of supported catalyst, which strongly influence the size of a fuel cell system—are also about one order of magnitude lower than for Pt. Assuming a similar balance of plant, at current Ag performance levels an Ag-based anion-exchange membrane fuel cell (AEMFC) stack that matches the performance of Pt-based PEM stacks would be a break-even exchange at best—i.e., the savings due to the cheaper catalyst would be offset by the

higher cost of larger cell components. However, any improvement in the activity of Ag-based electro-catalysts, along with recent advances in the design of more stable hydroxide exchange membranes[15–19] and improved anode electro-catalysts for alkaline hydrogen oxidation,[20] have the potential to make AEMFCs competitive with current state-of-the-art PEM fuel cells. By comparison, other proposed low-cost alternatives to Pt, such as metallic single-atom centers grafted into functionalized graphitic frameworks[21–23] or metal oxides supported on modified graphene,[24,25] are hampered by relatively low volumetric densities of active sites and/or poor durability under voltage cycling.

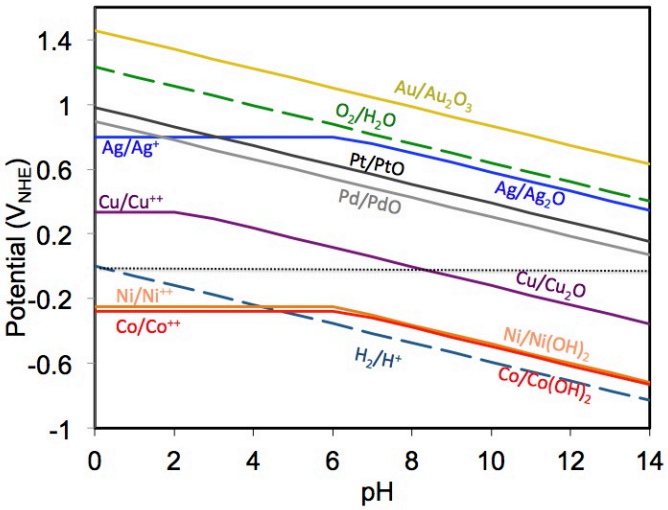

Figure 6-1: Pourbaix diagram for oxidation of various metals. Potential-pH boundaries for the most thermodynamically favorable oxidation process of various metals are shown. All phase boundaries assume relevant metal ion activities of either unity or the saturated equilibrium concentration if less. At high pH, the metallic state is generally preserved at potentials closer to the oxygen reduction equilibrium potential. Metal cation solubilities also generally decrease with pH, and oxidative dissolution gives way to oxidative passivation, making the electrode less prone to dissolving with spikes in voltage.

In this contribution we demonstrate the design of Pt-free Ag-Co alloy electro-catalysts for the ORR. We show that the Ag alloy exhibits more than five-fold improved performance in area-specific alkaline ORR activity compared to pure Ag electro-catalysts at $0.8V_{RHE}$, which is equivalent to the specific activity of Pt nanoparticles at the same potential. After accelerated aging following DOE protocols (30,000 cycles through typical operating potentials), the Ag alloy loses less than 10% of its initial achievable power density (based on electrochemical half-cell reaction performance). The observed enhancements in the ORR activity of Ag through alloying represent an important step towards making alkaline fuel cell technology viable. The discovery of the alloy electro-catalysts was guided by quantum-chemical Density Functional Theory (DFT) calculations. A novel bimetallic-precursor synthesis technique, which yielded a near-surface alloy of Ag and Co, was employed to synthesize the materials. The atomistic structure of the materials was characterized with x-ray diffraction (XRD) and aberration-corrected scanning transmission electron microscopy (STEM), coupled with energy dispersive x-ray spectroscopy (EDS) and electron energy loss spectroscopy (EELS). Cyclic voltammetry (CV) surface characterization and cobalt-selective electrochemical leaching provided additional evidence that Co atoms act through a ligand mechanism to perturb the Ag surface sites and improve their inherent electro-chemical activity.

6.1.1 Mechanism of ORR on Ag

Electrochemical oxygen reduction involves four proton/electron transfers to the O_2 molecule. The elementary step mechanism has been studied extensively, and it has been shown that on the metals of interest (i.e. Pt, Ag), it involves an initial reduction of O_2 to form an OOH intermediate in the rate-limiting step.[26–28] The subsequent dissociation of OOH into O and OH, and the formation and desorption of H_2O, are effectively equilibrated. On Pt electrodes it has been shown that the most abundant reaction intermediate under operating potentials above ~ 0.8 V_{RHE} is adsorbed OH, which limits the reaction by effectively poisoning sites.[28–30] In comparison, Ag is relatively more noble and becomes poisoned only at higher potentials, where a surface oxide is formed.[31–33] This suggests that under conditions of interest (0.8 V_{RHE}), the rate of the reaction on Ag is almost completely governed by the rate of the initial proton/electron transfer to O_2 to form OOH.

The mechanistic details discussed above are consistent with data in Figure 6-2, which shows free-energy diagrams, obtained using density functional theory (DFT) calculations,[34] for relevant reaction intermediates involved in the ORR on pure Pt and Ag, as well as several model Ag-alloy surfaces (full method details are provided in section 6.6). The free energy diagram illustrates that in contrast to Pt, where OH poisoning thermodynamically limits the performance (being the most energetically uphill step), the performance of Ag electro-catalysts is limited by reduction of O_2 to form OOH. More active Ag-based electrocatalysts should bind the OOH intermediate stronger than pure Ag, thereby accelerating the rate-limiting step. The data in Figure 6-2 indicate that this criterion is satisfied on alloys of Ag and the

late 3d transition metals (Co, Fe, Ni, and Cu). These alloy materials also bind other O-containing species, including OH, stronger than pure Ag, but not to a degree where their removal would be limiting. We note that while a multitude of alloy structural configurations are possible, the trend in activity reported in Figure 6-2 (stronger interaction of OOH with alloys compared to pure Ag) was observed for all alloy model systems that we investigated—i.e., irrespective of the alloy composition, any perturbation of Ag surface atoms by a 3d-metal positioned in proximity to the Ag active site resulted in stronger interaction of OOH with the Ag site. ORR free energy diagrams for alloys with differing geometries (location of the 3d metals and degree of lattice contraction) are given in Figure 6-3. In each of these systems we assumed that the outermost layer of the alloy is occupied by Ag atoms due to the low surface energy of Ag and the propensity of surface 3d metals to dissolve into the electrolyte at relevant conditions.[35–37]

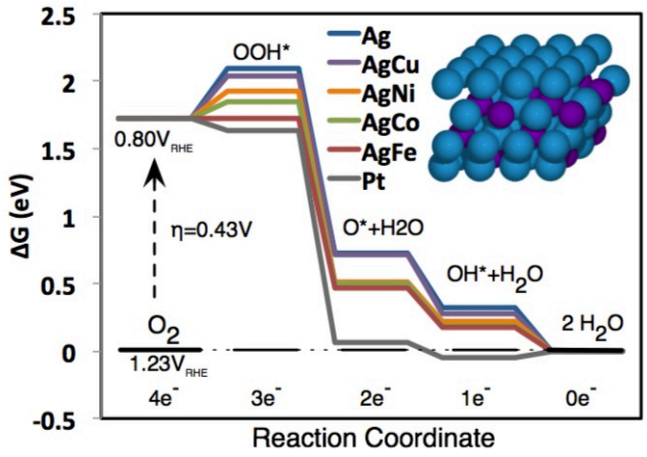

Figure 6-2: DFT-calculated free energy diagram for oxygen reduction reaction (ORR) on catalyst surfaces. Free energies of ORR surface intermediates on (111) surfaces of Ag, various Ag-alloys, and Pt at 0.8V with respect to the reversible hydrogen electrode. The model system for Ag-alloys (inset) is a four atomic-layer periodic slab containing 50% guest metal in the first subsurface layer of Ag, with 25% in the bottom layers. The pure Ag lattice constant was used in all cases (except pure Pt), and all free energies are calculated at ¼ monolayer adsorbate coverage.

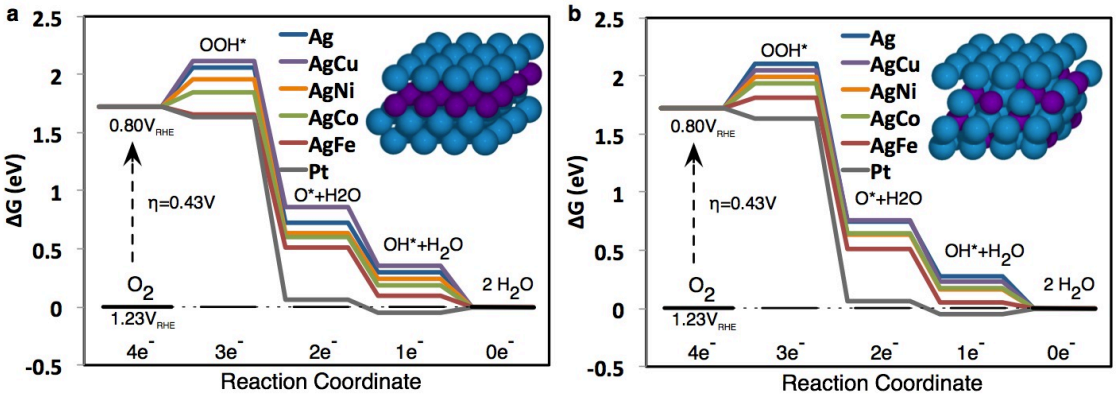

Figure 6-3: DFT-calculated free energy diagram for oxygen reduction reaction (ORR) on different Ag-alloy structures. Potential energies of ORR surface intermediates on various (111) surfaces of Ag-alloy model systems at 0.8V with respect to the reversible hydrogen electrode. (a) Ag-skin skin alloys, characterized by a monolayer of the guest metal in the second atomic layer of an Ag surface. Such simple systems have been demonstrated to provide consistent trends with the reactivity of real bimetallic catalysts.[56] (b) Ag_3X bulk alloys with Ag surface layer, containing guest metal X dispersed 50% in the second atomic layer and 25% in the lower two layers. Ag_3X structures have lattice constant set using Vegard's law for a 3:1 solid solution (a weighted average of the constituent element lattice constants), modeling the surface of a bulk alloy in which the particle core provides a contracted substrate for the surface atomic layers. All free energies are calculated at ¼ monolayer adsorbate coverage.

6.2 Synthesis and electrochemical performance

Noting the near-optimal characteristics for Ag-Co alloys in Figure 6-2, we chose to focus on these materials. We note that Ag and 3d-metals are immiscible in the bulk phase, and a few previous attempts to combine Ag with 3d metals using conventional synthetic routes, such as incipient wetness impregnation or colloidal co-reduction of common precursor salts did not produce alloys or succeed in generating significant activity enhancements in ORR.[38,39] In addition to the instability of the bulk alloy, large differences in the Ag and 3d-metal reduction potentials generally cause Ag to reduce much faster than the 3d-metals, making even a kinetic entrapment of 3d-metal atoms in the Ag matrix challenging. It has been shown that this issue can be addressed by reducing 3d metal and Ag precursors rapidly under very extreme synthesis conditions such as laser ablation deposition or gamma-ray reduction.[40] Utilizing the idea of rapid reduction, we have developed a more scalable synthesis approach based on modified incipient-wetness technique (depicted schematically in Figure 6-4a), adapted from concepts in several works.[41–44] An ordered, bimetallic precursor was precipitated onto a graphitic carbon support to create nanoparticles with atomic-scale mixing of the two metals. Reduction was carried out with very rapid heating and cooling to minimize thermal segregation and lessen differences in the rates of the each metal reduction. More specifically, the water-soluble precursors $K_3[Co(CN)_6]$ and $AgNO_3$ were sequentially added to a Vulcan XC72 carbon support (1:3 Co:Ag molar ratio, 20%wt metals), with drying after each step. These reagents form an insoluble salt, $Ag_3[Co(CN)_6]$, allowing unreacted material to be washed away and leave behind an

almost pure phase of $Ag_3[Co(CN)_6]$ nanoparticles, confirmed by XRD (shown later in Figure 6-8). The bimetallic salt particles were then introduced into a preheated furnace at 500°C under dilute hydrogen and quenched. Subsequent characterization of the material, discussed below in the text, showed that the method cannot produce complete bulk alloying, but can be optimized to isolate enough Co in the near surface region of Ag to modify its activity. The rapid heating was found to be critical to achieving this surface alloying, as slowly heated samples exhibited minimal activity enhancements.

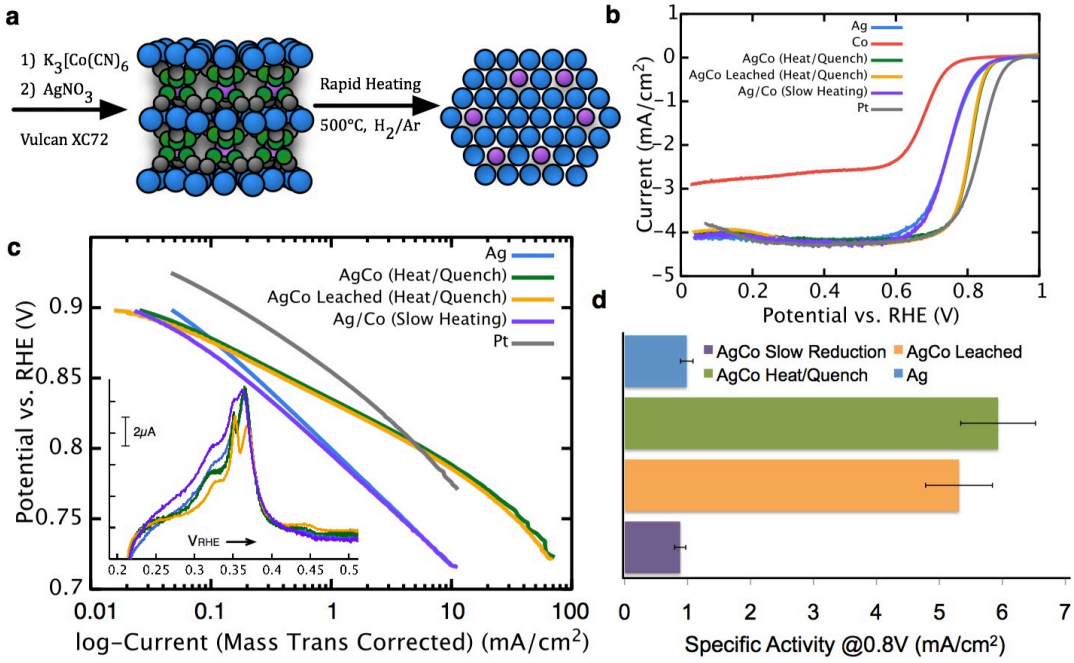

Figure 6-4: Synthesis scheme and electrochemical oxygen reduction performance of Ag-Co surface alloy materials. (a) Schematic of $Ag_3[Co(CN)_6]$ precursor formation and rapid reduction to form Ag-Co surface alloys. The colors correspond to Ag (blue), Co (purple), C (green), and N (black). **(b)** Rotating disk electrode i-V polarization curves (potentials relative to the reversible hydrogen electrode, RHE) taken in O_2-saturated, 0.1M NaOH at 25°C and 900 RPM for the Ag-Co surface alloy, as well as a leached alloy, a segregated Ag/Co sample, and pure Ag and Co.(c) Mass-transport corrected kinetic-current Tafel plots for the samples. The inset shows Pb-stripping voltammograms, used to measure electrochemical surface area, in argon-purged electrolyte with 125μM $Pb(NO_3)_2$ added after the activity measurements.(d) Summary of kinetic current densities for oxygen reduction on each sample, measured at $0.8V_{RHE}$.

Figure 6-4b shows the electrochemical polarization behavior of the Ag-Co catalyst, prepared as discussed above using rapid heating and cooling, and referred to as "as-prepared" alloy. Measurements were performed in O_2-saturated, 0.1M NaOH at room temperature in a thin-film rotating disk electrode (RDE) configuration.[45] We also show the performance for Ag-Co prepared by slow heating, as well as a pre-leached Ag-Co, elemental Ag and Co (prepared under the same conditions), and a commercial Pt-nanoparticle catalyst. The pre-leached alloys were prepared by electrochemically dissolving the Co exposed to the solution from the as-prepared Ag-Co alloy. Leaching naturally occurs over time in alkaline electrolyte due to the solubility of Co-oxides, but acid leaching was done for complete and certain removal. This was carried out by immersing the as-prepared Ag-Co catalyst into an electrochemical cell with 0.001 M H_2SO_4 + 0.1M Na_2SO_4 electrolyte under potential control just below the Co/Co^{2+} redox potential (-0.3V_{NHE}), and then cycling 400mV in the positive direction several times. A large Co stripping peak was observed on the first cycle, followed by no distinguishable voltammetric features thereafter, as shown in Figure 6-5. After leaching, the electrode was transferred to the test cell under the same conditions as the other samples. The active electrochemical surface area of Ag for each sample was measured using Pb-stripping voltammetry[46,47] after purging the electrolyte with argon.

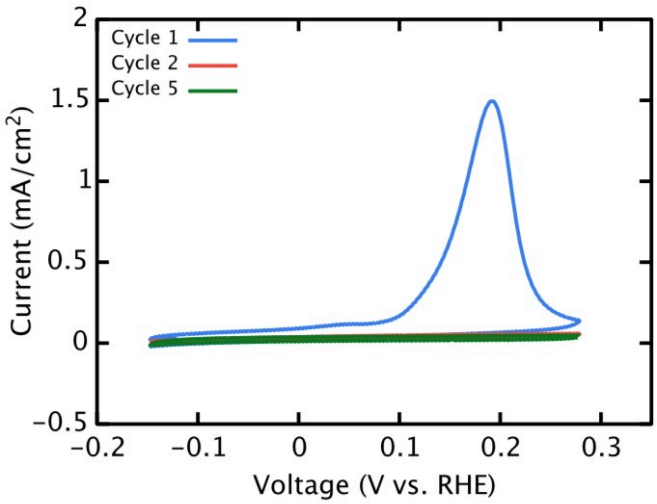

Figure 6-5: Leaching cyclic voltammetry (CV) of the Ag-Co alloy. CV's in argon-purged 0.001M H_2SO_4 + 0.1M Na_2SO_4, showing dissolution of Co on the first cycle, followed by featureless scans afterward. Scans were performed at 20mV/s and 25°C at 900RPM.

The polarization curves in Figure 6-4c show that both as-prepared and leached Ag-Co alloy catalyst particles have substantially better ORR activity than pure Ag or slowly-heated Ag-Co. The figure also shows that the performance of the alloy approaches that of Pt, matching its activity at potentials below ~0.8 V_{RHE}. We also show that pure Co does not exhibit appreciable activity—it is negligibly better than a blank Vulcan carbon film—producing a much lower limiting current than the Ag materials due to high selectivity to two-electron peroxide production. Comparing the polarization behavior of the as-prepared and leached alloys to pure Ag, it can be seen that the materials actually start off with relatively similar activity near the equilibrium potential and then separate at lower potentials—i.e., the performance enhancement is highest at larger overpotential. While the exact activity enhancement of Ag-Co relative to pure Ag is potential dependent, we have chosen to benchmark activity at $0.8V_{RHE}$, where the enhancement in area-specific activity reaches a factor of almost 6. The area-specific activities at $0.8V_{RHE}$ are summarized

in Figure 6-4d. We stress that to increase the confidence in our conclusions, each catalyst film tested contained the same mass of material and very similar dispersions (between 30-60cm^2/mg based on Pb-stripping area for all samples). Consequently, Ag mass-specific activities very closely reflect the differences in area-specific activity. Koutecky-Levich analysis, shown in Figure 6-6, indicates that the number of electrons transferred for all Ag-based materials is close to 4 over the full range of potentials, demonstrating virtually complete selectivity to H_2O. Finally, we also performed standardized long-term performance studies, comparing the ORR activity of Ag and Ag-Co over the course of 30,000 cycles between $0.6V_{RHE}$ and $1.0V_{RHE}$ in O_2-saturated electrolyte. Polarization curves for these samples over time are provided in Figure 6-7. These studies show a loss in the half-wave potential of about 50mV for both Ag and the Ag-Co alloy, meaning a substantial activity enhancement in alloys is retained. Specific activities at the end of cycling, assessed by post-run Pb-stripping measurements, did not change appreciably. Thus, the deactivation is most likely due to loss of surface area through particle growth and physical detachment from the support.

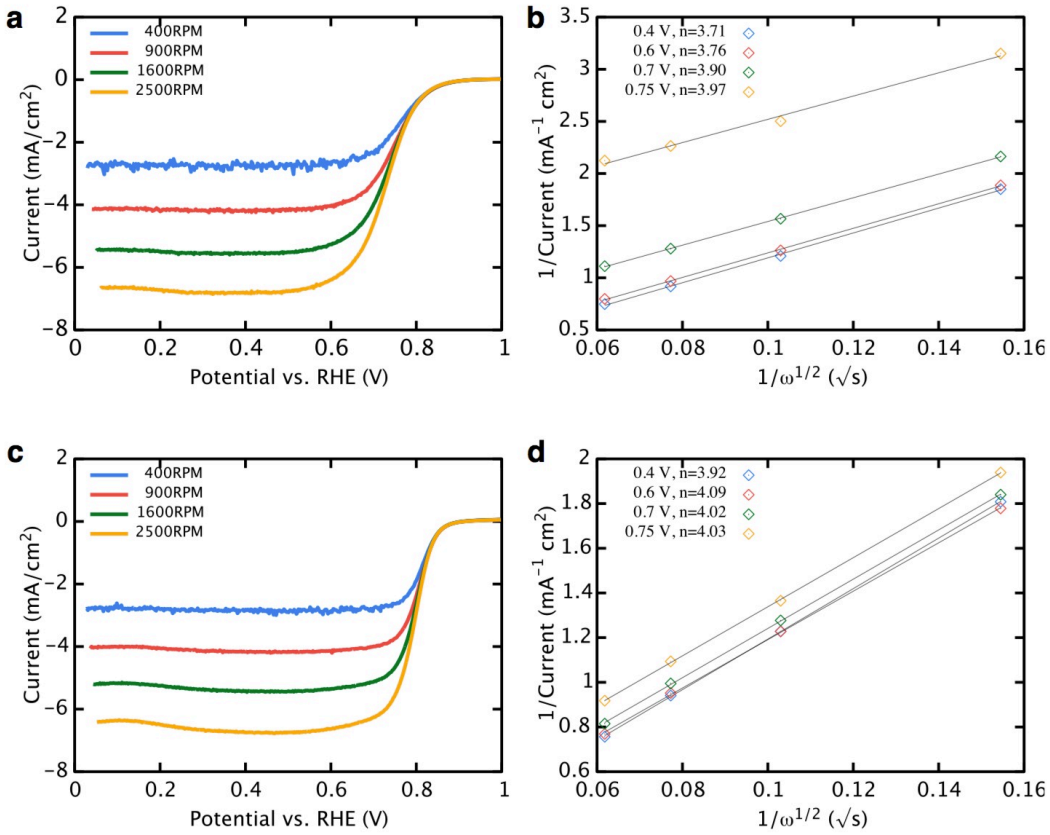

Figure 6-6: Rotating disk polarization curves with Koutecky-Levich plots. Polarization curves at variable rotation rate and Koutecky-Levich plots showing number of transferred electrons (derived from the slope) per O_2 for pure Ag ((a) and (b)), and the Ag-Co alloy ((c) and (d)).

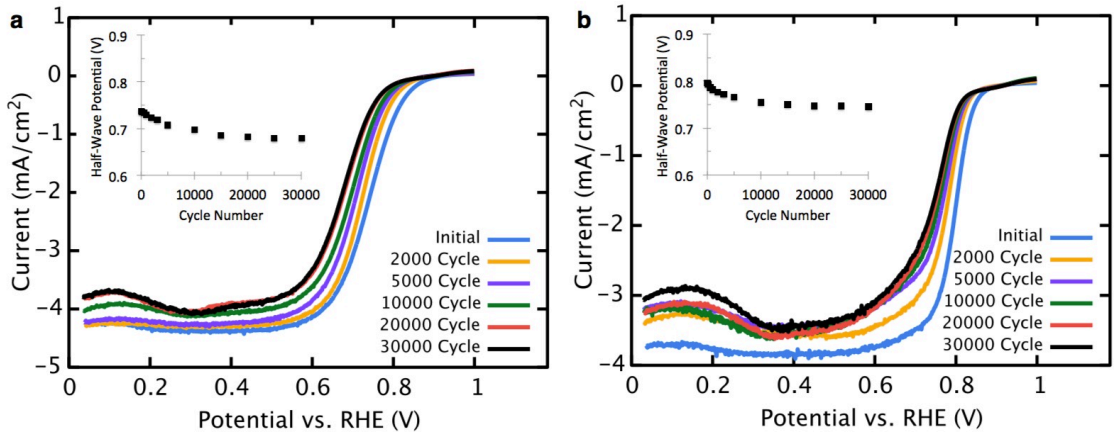

Figure 6-7: Long-term degradation of ORR polarization curves with cycling. Rotating disk electrode i-V polarization curves taken for the Ag (a) and Ag-Co surface alloy (b) nanoparticle/carbon thin-film catalysts in O_2-saturated, 0.1M NaOH at 25°C and 900 RPM for selected intervals over the course of voltage cycling from 0.6-1.0 V_{RHE}. The insets show the half-wave potentials at every interval measured.

6.3 Characterization of alloys

Figure 6-8a shows an STEM image of the as-prepared Ag-Co alloy catalyst particles and the corresponding Ag and Co elemental EDS maps based on their K-α fluorescence signals. The elemental maps indicate that Ag and Co signals overlap in some regions, and that a significant quantity of Co is segregated from Ag. Nanoparticles with majority Ag and Co phases as well as particles containing combinations of Ag and Co phases were identified. Median particle sizes, based on the STEM images, were ~7nm for Ag and ~15nm for Ag-Co. Additional STEM images and size histograms for Ag and Ag-Co samples are provided in Figure 6-9. Figure 6-8b shows XRD scans taken for a representative sample of $Ag_3[Co(CN)_6]$ precursor before and after rapid reduction at 500°C. The diffraction pattern of the product closely resembles that of pure Ag nanoparticles with slightly sharper peaks due to the larger crystallite size for the alloys. Control samples of metallic cobalt particles, also reduced at 500°C, as well as several cobalt oxide standards (not shown), indicate there are no detectable oxides, but a phase of very small, pure fcc-Co nanoparticles exists in the bimetallic product.

Though a uniform bulk alloy was not formed, we sought a more direct characterization of the near surface region of the Ag-Co catalyst particles using electron energy loss spectroscopy (EELS) in an aberration-corrected STEM. Figure 6-8c shows an image of a typical Ag-Co alloy catalyst particle, with energy loss spectra taken with the electron beam scattering through several different points at the edge and center of the particle. The spectra from the edge of the particle (points c and d) give the electronic fingerprint of primarily near-surface atoms and show a distinct Co-$L_{2,3}$ absorption edge at

780eV, as well as the Ag-$M_{4,5}$ edge with onset just below 400eV. The EELS spectra clearly indicate that Co atoms are present close to the surface of the particle. In comparison, the Co atom signal was never detected when irradiating the center of particles. The main reasons for this are the increased particle thickness and much lower ratio of Co to Ag atoms encountered by the electron beam passing through the center of the particle, which lead to plural elastic scattering to high angles and absorption edge signal convolution with Ag plasmon losses, suppressing signals from small concentrations of Co. We also note that we detected Co in the outermost regions (within ~0.5nm from the edge) of many, but not all chosen particles. Due to the intermittent Co detection at particle edges, we suspect that our samples contained particles with ensembles of Ag-Co surface-alloys (i.e., mixing of Ag and Co atoms close to the particle surface), as well as pure Ag and Co. This heterogeneity is consistent with the distribution of each element observed with EDS.

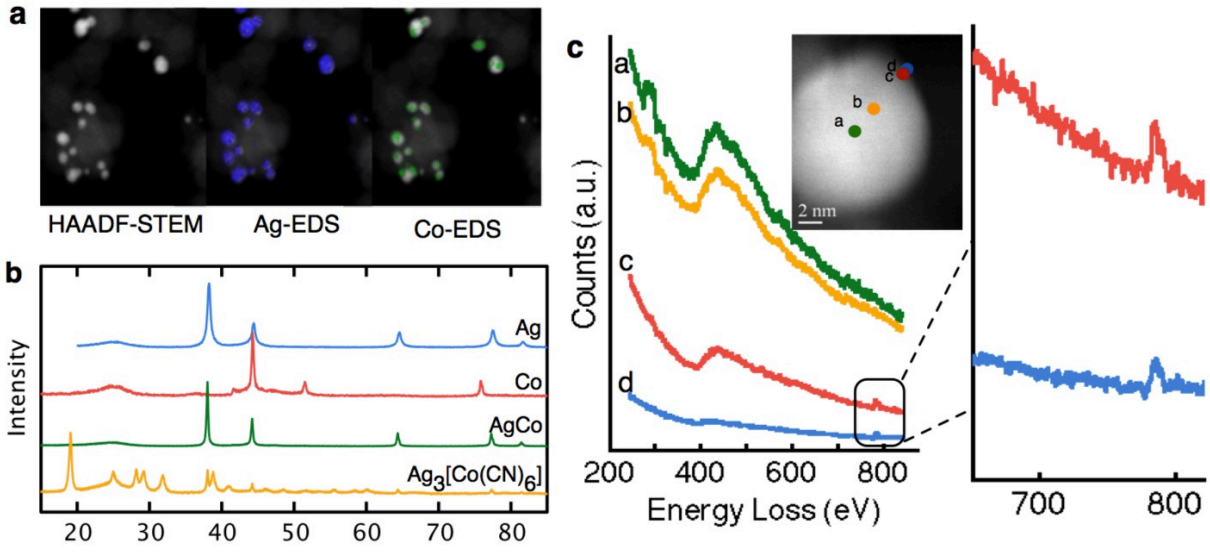

Figure 6-8: Characterization of Ag-Co materials. (a) High-angle annular dark field STEM image of Ag-Co surface alloy particles with corresponding Ag and Co K-α EDS signals. **(b)** XRD patterns for the carbon-supported $Ag_3[Co(CN)_6]$ nanoparticle precursor, Ag-Co alloy product, and pure Ag and Co nanoparticles prepared under the same conditions. **(c)** Electron energy loss spectra acquired for an Ag-Co surface alloy nanoparticle in an aberration-corrected STEM. The Co ionization edge is seen for spectra taken near the particle edge, which is comprised of near-surface atoms.

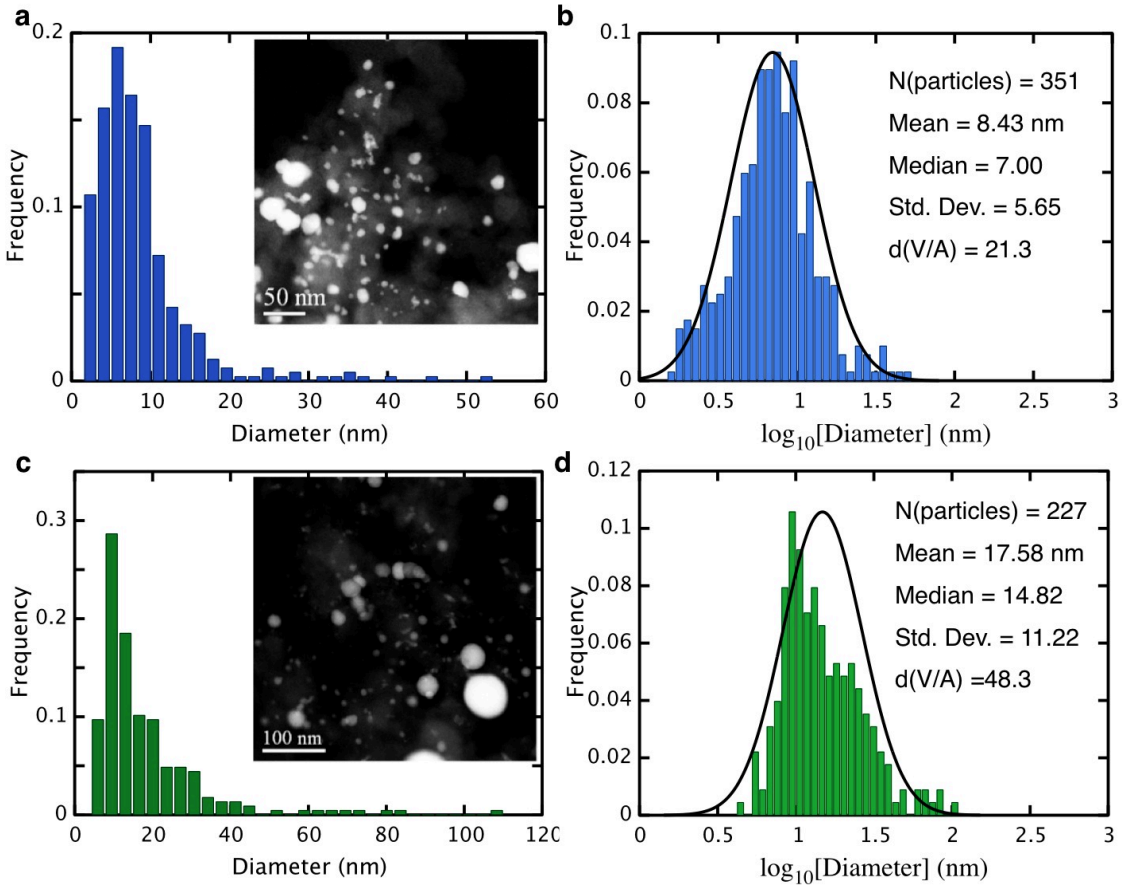

Figure 6-9: Particle-size histograms and representative STEM images. Particle sizes most closely fit a log-normal distribution, as is common with incipient-wetness syntheses. Histograms for particle diameter and log-diameter for Ag ((a) and (b)) and Ag-Co ((c) and (d)), reduced from $AgNO_3$ and $Ag_3[Co(CN)_6]$ respectively on Vulcan carbon (20%wt metals basis) for 10min at 500°C under 4%H_2/Ar. Insets show representative STEM-HAADF images of each material. Volume-area averaged diameters, d(V/A), is calculated as $\Sigma d_i^3/\Sigma d_i^2$.

6.4 Electrochemical surface analysis

In Figure 6-10, we show cyclic voltammograms (CVs) for the as-prepared and leached Ag-Co catalyst particles, as well as pure Ag and Co samples, with upper CV potential limits of 1.00 V_{RHE} and 1.15 V_{RHE}. The CV potential limits were selected to investigate differences between destructive surface oxidation (which for Ag takes place at potentials above ~ 1.1 V_{RHE}) resulting in the exposure of subsurface layers to the

electrolyte, and non-destructive surface oxidation for potentials below 1 V_{RHE}. The CV of pure Ag is relatively featureless below 1V, except for a very faint, broad oxidation around 0.8-0.9 V. Studies on low-index single crystals of Ag have shown that at this voltage the formation of a surface oxide layer is initiated.[31,48] Due to the facet distribution on the nanoparticles, this appears only as a slowly rising oxidative current. Upon cycling to 1.15V, where deeper multi-layer oxidation is believed to set in, the 0.8-0.9 V oxidation feature becomes more pronounced, presumably due to roughening and an increase in the surface area. In contrast, pure Co exhibits several major features corresponding to Co bulk oxidation processes. There are two overlapping peaks at low potentials, which are associated with the formation of $Co(OH)_2$ and CoO, as well as another broad oxidation feature at higher potential, where Co_3O_4, Co_2O_3, and CoOOH become thermodynamically accessible in a narrow potential range.[6,49,50] The as-prepared Ag-Co material shows the characteristic Co-oxidation features at slightly shifted potentials, as well as features that are not seen on either pure metal. It is instructive to compare this as-prepared Ag-Co alloy to the leached Ag-Co in order to delineate the origins of the various features. On the as-prepared Ag-Co, there are two anodic low-voltage peaks which are likely related to $Co(OH)_2$ and CoO formation. This low potential Co-oxidation process is not seen during cycling to 1V on the leached material, which is consistent with the hypothesis that leaching removes any Co atoms that are accessible to the electrolyte. When the surface is roughened by cycling to 1.15 V, the low-potential $Co(OH)_2$ peak returns on the pre-leached samples, further supporting the notion that appreciable Co is retained after leaching, but it is trapped in the subsurface layers of Ag. Cycling to 1.15 V essentially exposes the Co atoms buried in the particles to the electrolyte.

At higher potentials relevant to fuel cell operating conditions, the as-prepared and pre-leached Ag-Co alloys exhibit two peaks appearing at roughly 0.6 V and 0.8 V that are not seen on Co. These occur earlier than the broad oxidation feature of Ag and are also larger, corresponding to a higher degree of surface oxidation. We suspect that these features correspond to oxygen species binding to the alloy surface, which is consistent with the hypothesis that Ag-Co alloys should be more reactive than Ag toward these species. Also consistent with stronger oxygen binding energy is the observation that the sharp current increase near 1.1 V sets in at lower potential on the Ag-Co compared to Ag.

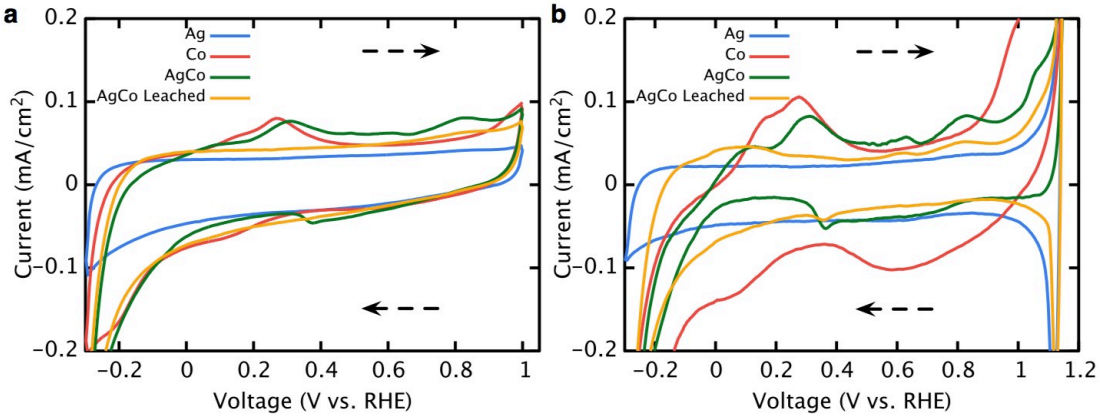

Figure 6-10: Comparative cyclic voltammetry (CV) of the Ag-Co surface alloy. (a) CV's in argon-purged 0.1M NaOH recorded for the as-prepared and leached Ag-Co catalyst particles, as well as pure Ag and pure Co control samples, with upper potential limits of $1.00V_{RHE}$ (a) and $1.15V_{RHE}$ (b). The differing potential limits illustrate changes between destructive and non-destructive surface oxidation, which reveals the presence of Co below the catalyst surface.

6.5 Conclusions

We have demonstrated the design of Ag-Co surface alloy electro-catalysts that exhibit more than five-fold improved performance in alkaline ORR activity compared to pure Ag at $0.8V_{RHE}$, and roughly equivalent specific activity to Pt. This represents a

significant step toward designing economically viable catalysts for low temperature fuel cells. The Ag-Co materials were identified with quantum chemical calculations and synthesized with a novel technique that generates a surface alloy, despite the bulk immiscibility of the constituent materials. We showed that the origin of the activity improvement comes from a ligand effect, in which Co perturbs the Ag surface sites and improves their inherent activity.

6.6 Experimental Details

6.6.1 Catalyst Synthesis

The carbon-supported Ag-Co nanoparticles were synthesized by a multi-stage incipient wetness impregnation. In a typical synthesis 0.25mmol of $K_3[Co(CN)_6]$ and 1.125mmol $AgNO_3$ (both Sigma Aldrich) were dissolved in separate 2mL solutions of deionized water. The solutions were added dropwise, alternating 1mL of each precursor at a time, to 440mg of Vulcan XC72 (Cabot, pretreated 2h in H_2 at 400°C), with drying at 60°C between each mL of water added, for a total of 4 impregnation/drying cycles. This forms $Ag_3[Co(CN)_6]$ particles with excess $AgNO_3$ and KNO_3 that were removed by triply rinsing and centrifuging the powder with deionized water, followed by drying again. The Ag/C and Co/C particles were prepared to comparable molar loadings by single-step incipient wetness impregnation using the same precursors, with the modification of post-reduction rinsing for Co to remove KCN. For reduction, precursor powders were inserted into a preheated tube furnace at 500°C under 4%H_2/Ar, held for 10 minutes, then quenched with flowing air on the tube exterior.

6.6.2 Electrochemical testing

Electrochemical measurements were performed at room temperature in an all-Teflon three-electrode cell (made in house) with a Gamry Instruments Reference 3000 potentiostat/galvanostat/FRA. The reference (Hg/HgO in 1M KOH, Radiometer Analytical) and counter electrodes (Pt wire, Alfa Aesar) were both in isolated compartments with long diffusion paths to the working electrode chamber. Working electrodes were prepared by sonicating the catalyst powders in 99.9% acetone (Fisher) at 0.75mg/mL for >1h and dispersing two 12 μL droplets onto a 5mm glassy carbon electrode insert (Pine Instruments), which had been polished with 0.05μm alumina paste and sonicated in ultrapure water prior to use. These electrodes were put into a Teflon RDE housing, attached to a rotator (Pine) and inserted into the cell under potential control using a Pt wire dummy electrode, temporarily connected to the working electrode lead.

Electrolyte solutions of 0.1M NaOH were prepared from ultrapure water (18MΩ, Millipore) and 99.99% sodium hydroxide (Sigma Aldrich). An uncompensated resistance was measured via the high frequency impedance (generally ~40Ω), and was corrected for in the polarization curves. All potentials are reported relative to the Reversible Hydrogen Electrode ($V_{RHE} = V_{NHE} + 0.0591pH$), for which the potential was calibrated by voltammetry to find the potential of zero current in H_2 saturated electrolyte with a Pt electrode (Pine). Cyclic voltammograms were taken in argon-purged solution, and rotating disk polarization curves were taken in O_2-saturated solution. Pb-stripping voltammetry was performed immediately after polarization measurements by purging the solution and adding 125μM $Pb(NO_3)_2$, then repeatedly holding the potential at $0.22V_{RHE}$,

causing Pb underpotential deposition, and sweeping to $0.6V_{RHE}$ at 20mV/s. The stable voltammograms were integrated assuming $280\mu C/cm^2$, which was established based on prior single-crystal measurements of the low-index Ag facets.[46,47] Pt nanoparticle samples were commercially available 4nm Pt on Vulcan XC72 carbon, obtained from Sigma Aldrich. Activity was normalized to surface area measured with underpotential deposition of hydrogen between $0.05V_{RHE}$ and $0.4V_{RHE}$, and measured activites were consistent with numerous other studies in both acid and basic environment.[14,51,52]

To estimate the ORR selectivity to H_2O vs. H_2O_2 ($4e^-$ vs. $2e^-$ reduction), plots of inverse current density ($1/j$) vs. inverse square-root rotation rate ($\omega^{-1/2}$) were analyzed with the Koutecky-Levich (KL) equation: $1/|j|=1/|j_k|+1/(0.62nFD^{2/3}\upsilon^{-1/6}C\omega^{1/2})$,[53] where n is the number of electrons transferred per molecule reacted, F is the Faraday constant, D is the diffusivity of the reactant, υ is the kinematic viscosity of the electrolyte solution, and C is the concentration of reactant. For oxygen saturated in 0.1M NaOH, we used the values $D=1.93\text{x}10^{-5}$ cm^2/s, $\upsilon=1.09\text{x}10^{-2}$ cm^2/s, and $C=1.26\text{x}10^{-3}$ mol/L.[54] The slope of the KL plot was then used to determine n, which is assumed to be a weighted average between the 2 and 4 electron products.

Long-term stability of the ORR catalysts was assessed using a DOE protocol for accelerated aging of fuel cell membrane-electrode assemblies,[1] which was applied to the catalyst films in the same rotating-disk three-electrode cell configuration as all other tests. After saturating the 0.1M NaOH electrolyte with O_2 and measuring initial performance, the electrode was repeatedly cycled between $0.6\text{-}1.0V_{RHE}$. Polarization curves were taken after 100, 500, 1000, 2000, 3000, and 5000 cycles, and every 5000 cycles thereafter until 30,000 cycles. Pb-stripping measurements could not be performed

at each interval due to the contamination they inherently cause, but the initial electrochemical surface areas of each material were known to within 10% from prior replicate tests, and the final areas were measured after 30,000 cycles.

For leached samples, the leaching of exposed cobalt was performed under potential control rather than exposing the catalyst to acid. This method was implemented to avoid redox-mediated Ostwald ripening of Ag in acidic solution.[55] Prior to ORR activity measurements, the as-prepared Ag-Co catalyst thin-film electrode was immersed into a separate 3-electrode electrochemical cell with 0.001 M H_2SO_4 + 0.1M Na_2SO_4 electrolyte under potential control (using a glassy carbon dummy electrode) just below the Co/Co^{2+} redox potential ($-0.3V_{NHE}/0.123V_{RHE}$). An Hg/Hg_2SO_4 reference electrode and Pt wire counter electrode were used. The Ag-Co/carbon film was cycled 400mV in the positive direction for 5 cycles. Upon finishing, the electrode was held at the upper potential limit (again with the dummy electrode), withdrawn from the cell, and rinsed with ultrapure water followed by 0.1M NaOH electrolyte so that it could be detached without appreciable corrosion and moved to the alkaline three-electrode cell.

6.6.3 Characterization

Scanning transmission electron microscopy (STEM) with energy dispersive x-ray spectroscopy (EDS) was carried out in JEOL 2010F 200keV field-emission electron microscope with EDAX X-ray detector and Genesis software package. Electron energy loss spectroscopy (EELS) was carried out in a JEOL 2100F electron microscope (also 200keV) with CEOS spherical-aberration corrector on the probe forming side of the column. A Gatan Tridiem imaging filter was used to collect the EELS spectra. Energy

dispersion for the spectrometer was 0.3 eV per pixel (FWHM resolution ~1.5eV) and the collection angle was ~125mrad. Signals were identified assuming a standard power-law background model. XRD measurements were conducted in a Rigaku rotating anode diffractometer with a monochromated CuKα x-ray source at a scan rate of 1°/min.

6.6.4 Theoretical calculations

All DFT calculations were carried out with the Dacapo pseudopotential plane wave code (http://www.camd.dtu.dk), using the generalized gradient approximation (GGA) and RPBE exchange correlation functional. All surfaces calculations used a four-layer 2x2 fcc-[111] periodic unit cell separated by 12Å of vacuum space in the [111]-direction and a dipole layer to electrostatically decouple the slabs. The bottom two layers were fixed while the top two layers and all adsorbates were relaxed until the sum of forces was below 0.05 eV/Å. Ultrasoft pseudopotentials were used to represent the ionic cores, while the valence electron density was determined through iterative diagonalization of the Kohn-Sham Hamiltonian using Pulay mixing. Unit cells were sampled with a 4x4x1 Monkhorst-Pack k-point grid, and the plane wave basis-set energy cutoff was 350eV. An electronic temperature of 0.1 k_BT was used, with final energies extrapolated to 0 K. Potential-dependent free energy diagrams were calculated by using the relation $\Delta E_{adsorption}=E_{system}-E_{slab}-E_{adsorbates}$, then converting to Gibbs free energy with the relationship: $\Delta G = \Delta E - T\Delta S + \Delta ZPE + ne(U-U_0)$. Entropy changes ($\Delta S$) were obtained from tabulated values (http://webbook.nist.gov/chemistry/). Zero point energies (ZPE) were taken from prior DFT work.[34] The contribution of potential was computed assuming equilibrium between H_2 and H^+/e^- at $0.0V_{NHE}$ and shifting energies by the number of

electrons times the potential change, $ne(U-U_0)$. Additional corrections for stabilization effects by the aqueous interface were also made in accordance with prior studies.[56,57]

6.7 References

1. The US Department of Energy (DOE). Energy Efficiency and Renewable Energy. at <http://www1.eere.energy.gov/hydrogenandfuelcells/mypp/>

2. Debe, M. K. Electrocatalyst approaches and challenges for automotive fuel cells. *Nature* **486,** 43–51 (2012).

3. Borup, R. *et al.* Scientific aspects of polymer electrolyte fuel cell durability and degradation. *Chemical Reviews* **107,** 3904–3951 (2007).

4. Gasteiger, H. A., Kocha, S. S., Sompalli, B. & Wagner, F. T. Activity benchmarks and requirements for Pt, Pt-alloy, and non-Pt oxygen reduction catalysts for PEMFCs. *Applied Catalysis B: Environmental* **56,** 9–35 (2005).

5. Wagner, F. T., Lakshmanan, B. & Mathias, M. F. Electrochemistry and the Future of the Automobile. *The Journal of Physical Chemistry Letters* **1,** 2204–2219 (2010).

6. Pourbaix, M. *Atlas of Electrochemical Equilibria in Aqueous Solutions*. (National Association of Corrosion Engineers, 1974).

7. *Mineral Commodity Summaries 2010*. (2010). at <http://minerals.usgs.gov/minerals/pubs/mcs/>

8. Spendelow, J. S. & Wieckowski, A. Electrocatalysis of oxygen reduction and small alcohol oxidation in alkaline media. *Phys. Chem. Chem. Phys.* **9,** 2654–75 (2007).

9. Guo, J., Hsu, A., Chu, D. & Chen, R. Improving Oxygen Reduction Reaction Activities on Carbon-Supported Ag Nanoparticles in Alkaline Solutions. *J. Phys. Chem. C* **114,** 4324–4330 (2010).

10. Coutanceau, C., Demarconnay, L., Lamy, C. & Leger, J. M. Development of electrocatalysts for solid alkaline fuel cell (SAFC). *Journal of Power Sources* **156,** 14–19 (2006).

11. Wiberg, G. K. H., Mayrhofer, K. J. J. & Arenz, M. Investigation of the Oxygen Reduction Activity on Silver - A Rotating Disc Electrode Study. *Fuel Cells* **10,** 575–581 (2010).

12. Alia, S. M., Duong, K., Liu, T., Jensen, K. & Yan, Y. Supportless Silver Nanowires as Oxygen Reduction Reaction Catalysts for Hydroxide-Exchange Membrane Fuel Cells. *ChemSusChem* **5,** 1619–1624 (2012).

13. Singh, P. & Buttry, D. a. Comparison of Oxygen Reduction Reaction at Silver Nanoparticles and Polycrystalline Silver Electrodes in Alkaline Solution. *The Journal of Physical Chemistry C* **116,** 10656–10663 (2012).

14. Oezaslan, M., Hasché, F. & Strasser, P. Oxygen Electroreduction on PtCo3, PtCo and Pt3Co Alloy Nanoparticles for Alkaline and Acidic PEM Fuel Cells. *Journal of The Electrochemical Society* **159,** B394 (2012).

15. Varcoe, J. R. & Slade, R. C. T. Prospects for Alkaline Anion-Exchange Membranes in Low Temperature Fuel Cells. *Fuel Cells* **5,** 187–200 (2005).

16. Varcoe, J. R., Slade, R. C. T., Wright, G. L. & Chen, Y. L. Steady-state dc and impedance investigations of H-2/O-2 alkaline membrane fuel cells with commercial Pt/C, Ag/C, and Au/C cathodes. *J. Phys. Chem. B* **110,** 21041–21049 (2006).

17. Danks, T. N., Slade, R. C. T. & Varcoe, J. R. Alkaline anion-exchange radiation-grafted membranes for possible electrochemical application in fuel cells. *J. Mater. Chem.* **13,** 712–721 (2003).

18. Adams, L., Poynton, S. & Tamain, C. A Carbon Dioxide Tolerant Aqueous-Electrolyte-Free Anion-Exchange Membrane Alkaline Fuel Cell. *ChemSusChem* **1,** 79–81 (2008).

19. Deavin, O. I. *et al.* Anion-exchange membranes for alkaline polymer electrolyte fuel cells: comparison of pendent benzyltrimethylammonium- and benzylmethylimidazolium-head-groups. *Energy & Environmental Science* **5,** 8584 (2012).

20. Strmcnik, D. *et al.* Improving the hydrogen oxidation reaction rate by promotion of hydroxyl adsorption. *Nature Chemistry* **5,** 300–306 (2013).

21. Lefèvre, M. Iron-Based Catalysts with Improved Oxygen Reduction Activity in Polymer Electrolyte Fuel Cells. *Science* **324,** 71–74 (2009).

22. Proietti, E. *et al.* Iron-based cathode catalyst with enhanced power density in polymer electrolyte membrane fuel cells. *Nature communications* **2,** 416 (2011).

23. Wu, G., More, K. L., Johnston, C. M. & Zelenay, P. High-performance electrocatalysts for oxygen reduction derived from polyaniline, iron, and cobalt. *Science* **332,** 443–7 (2011).

24. Liang, Y., Li, Y., Wang, H., Zhou, J. & Wang, J. Co3O4 nanocrystals on graphene as a synergistic catalyst for oxygen reduction reaction. *Nature Materials* **10,** 780–786 (2011).

25. Ishihara, A., Ohgi, Y., Matsuzawa, K., Mitsushima, S. & Ota, K. Progress in non-precious metal oxide-based cathode for polymer electrolyte fuel cells. *Electrochimica Acta* **55,** 8005–8012 (2010).

26. Stamenkovic, V. R. *et al.* Improved oxygen reduction activity on Pt3Ni(111) via increased surface site availability. *Science* **315,** 493–497 (2007).

27. Stephens, I. E. L., Bondarenko, A. S., Grønbjerg, U., Rossmeisl, J. & Chorkendorff, I. Understanding the electrocatalysis of oxygen reduction on platinum and its alloys. *Energy & Environmental Science* **5,** 6744–6762 (2012).

28. Holewinski, A. & Linic, S. Elementary Mechanisms in Electrocatalysis: Revisiting the ORR Tafel Slope. *Journal of the Electrochemical Society* **159,** H864–H870 (2012).

29. Markovic, N. M. & Ross, P. N. Surface science studies of model fuel cell electrocatalysts. *Surface Science Reports* **45,** 117–229 (2002).

30. Tripković, V., Skúlason, E., Siahrostamia, S., Nørskov, J. K. & Rossmeisl, J. The Oxygen Reduction Reaction Mechanism on Pt(111) from Density Functional Theory Calculations. *Electrochimica Acta* **55,** 7975–7981 (2010).

31. Savinova, E. R. *et al.* Structure and dynamics of the interface between a Ag single crystal electrode and an aqueous electrolyte. *Faraday Discussions* **121,** 181–198 (2002).

32. Horswell, S. L. *et al.* A Comparative study of hydroxide adsorption on the (111), (110), and (100) faces of silver with cyclic voltammetry, ex situ electron diffraction, and in situ second harmonic generation. *Langmuir* **20,** 10970–10981 (2004).

33. Hansen, H. A., Rossmeisl, J. & Norskov, J. K. Surface Pourbaix diagrams and oxygen reduction activity of Pt, Ag and Ni(111) surfaces studied by DFT. *Phys. Chem. Chem. Phys.* **10,** 3722–3730 (2008).

34. Nørskov, J. K. *et al.* Origin of the overpotential for oxygen reduction at a fuel-cell cathode. *The Journal of Physical Chemistry B* **108,** 17886–17892 (2004).

35. Vitos, L., Ruban, A. V, Skriver, H. L. & Kollar, J. The surface energy of metals. *Surface Science* **411,** 186–202 (1998).

36. Christensen, A. *et al.* Phase diagrams for surface alloys. *Physical Review B* **56,** 5822–5834 (1997).

37. Stamenkovic, V. R., Mun, B. S., Mayrhofer, K. J. J., Ross, P. N. & Markovic, N. M. Effect of surface composition on electronic structure, stability, and electrocatalytic properties of Pt-transition metal alloys: Pt-skin versus Pt-skeleton surfaces. *Journal of the American Chemical Society* **128,** 8813–9 (2006).

38. Fernandez, J., Walsh, D. & Bard, A. Thermodynamic guidelines for the design of bimetallic catalysts for oxygen electroreduction and rapid screening by scanning electrochemical microscopy. M-Co (M: Pd, Ag, Au). *Journal of the American Chemical Society* 357–365 (2005).

39. Lima, F. H. B., De Castro, J. F. R. & Ticianelli, E. A. Silver-cobalt bimetallic particles for oxygen reduction in alkaline media. *Journal of Power Sources* **161,** 806–812 (2006).

40. Zhang, Z. Y., Nenoff, T. M., Huang, J. Y., Berry, D. T. & Provencio, P. P. Room Temperature Synthesis of Thermally Immiscible Ag-Ni Nanoalloys. *J. Phys. Chem. C* **113,** 1155–1159 (2009).

41. Wang, D. & Li, Y. Bimetallic nanocrystals: liquid-phase synthesis and catalytic applications. *Advanced Materials* **23,** 1044–60 (2011).

42. Gong, K., Su, D. & Adzic, R. R. Platinum-monolayer shell on AuNi(0.5)Fe nanoparticle core electrocatalyst with high activity and stability for the oxygen reduction reaction. *Journal of the American Chemical Society* **132,** 14364–6 (2010).

43. Goodwin, A. L. *et al.* Colossal positive and negative thermal expansion in the framework material Ag3[Co(CN)6]. *Science* **319,** 794–7 (2008).

44. Ludi, A., Gudel, H. U. & Dvorak, V. The structure of H3Co(CN)6 and Ag3Co(CN)6. *Helvetic Chimica Acta* **7,** 2035–2039 (1967).

45. Schmidt, T. J. *et al.* Characterization of high-surface area electrocatalysts using a rotating disk electrode configuration. *JOURNAL OF THE ELECTROCHEMICAL SOCIETY* **145,** 2354–2358 (1998).

46. Kirowa-Eisner, E., Bonfil, Y., Tzur, D. & Gileadi, E. Thermodynamics and kinetics of upd of lead on polycrystalline silver and gold. *Journal of Electroanalytical Chemistry* **552,** 171–183 (2003).

47. Herrero, E., Buller, L. J. & Abruna, H. D. Underpotential deposition at single crystal surfaces of Au, Pt, Ag and other materials. *Chemical Reviews* **101,** (2001).

48. Horswell, S. L. *et al.* A Comparative study of hydroxide adsorption on the (111), (110), and (100) faces of silver with cyclic voltammetry, ex situ electron diffraction, and in situ second harmonic generation. *Langmuir* **20,** 10970–10981 (2004).

49. Bratsch, S. Standard electrode potentials and temperature coefficients in water at 298.15K. *J. Phys. Chem. Ref. Data* **18,** 1–21 (1989).

50. Gerken, J. B. *et al.* Electrochemical water oxidation with cobalt-based electrocatalysts from pH 0-14: the thermodynamic basis for catalyst structure, stability, and activity. *Journal of the American Chemical Society* **133,** 14431–42 (2011).

51. Sheng, W., Chen, S., Vescovo, E. & Shao-Horn, Y. Size Influence on the Oxygen Reduction Reaction Activity and Instability of Supported Pt Nanoparticles. *Journal of The Electrochemical Society* **159,** B96 (2012).

52. Sheng, W., Gasteiger, H. a. & Shao-Horn, Y. Hydrogen Oxidation and Evolution Reaction Kinetics on Platinum: Acid vs Alkaline Electrolytes. *Journal of The Electrochemical Society* **157,** B1529–36 (2010).

53. Bard, A. J. & Faulkner, L. R. *Electrochemical Methods: Fundamentals and Applications*. (John Wiley & Sons, Inc., 2001).

54. Blizanac, B. B., Ross, P. N. & Markovic, N. M. Oxygen reduction on silver low-index single-crystal surfaces in alkaline solution: Rotating ring Disk(Ag(hkl)) studies. *J. Phys. Chem. B* **110,** 4735–4741 (2006).

55. Redmond, P. L., Hallock, a J. & Brus, L. E. Electrochemical ostwald ripening of colloidal ag particles on conductive substrates. *Nano letters* **5,** 131–5 (2005).

56. Greeley, J. *et al.* Alloys of platinum and early transition metals as oxygen reduction electrocatalysts. *Nature Chemistry* **1,** 552–556 (2009).

57. Viswanathan, V., Hansen, H. A., Rossmeisl, J. & Nørskov, J. K. Universality in Oxygen Reduction Electrocatalysis on Metal Surfaces. *ACS Catalysis* **2,** 1654–1660 (2012).

Chapter 7: Oxygen reduction activity of Ag-M (M=Fe, Ni, Co) materials produced by decomposition of bimetallic precursors

Silver is an effective catalyst for the electrochemical oxygen reduction reaction (ORR) in alkaline environments ($O_2 + 2H_2O + 4e^- \rightarrow 4OH^-$), but it is known that the rate is limited by activation of O_2. We have recently computationally identified a series of Ag-3d metal (Ni, Co, Fe) alloys that will bind oxygenated species more strongly than pure Ag and may be improved ORR catalysts. However, Ag and these metals are thermodynamically immiscible. Herein we have explored the use of rapid reduction of bimetallic $Ag_x[M(CN)_y]$ precursors (M=Fe, Ni, Co) as a possible means to induce some degree of alloying between the metals and enhance the ORR activity relative to pure Ag. The materials were characterized with x-ray diffraction (XRD) at each stage of synthesis as well as cyclic voltammetry (CV) to assess their surface reactivity. Oxygen reduction activity measurements were performed with the thin-film rotating disk electrode (RDE) method and show significantly improved activity for Ag-Co. However, Ag-Ni and Ag-Fe exhibit similar activity to monometallic Ag, and this is attributed to a failure to produce alloying. For Ag-Ni, the stoichiometry (2:1) of the precursor may be too low to provide an Ag matrix capable of trapping Ni, while for Ag-Fe the issue is likely related to low stability of the precursor and/or possible voltage-induced segregation during testing.

7.1 Introduction

Silver is known to exhibit appreciable catalytic activity toward the electrochemical oxygen reduction reaction (ORR) in alkaline environments (O_2 + $2H_2O$ +$4e^- \rightarrow 4OH^-$), although more costly Pt-based materials are superior catalysts. The reaction is of critical importance for the development of economically viable hydrogen fuel cells, and US DOE estimates show that for an Ag-based alkaline fuel cell system to be cost-competitive with Pt-based systems, an Ag catalyst must demonstrate about $1/10^{th}$ the turnover rate of Pt (for similar loading and dispersion) at relevant operating conditions.[1,2]

Recently, we have demonstrated with quantum chemical calculations that modification of Ag by incorporation of subsurface 3d-transition metal ligands will substantially increase the reactivity of the surface toward oxygen-containing species.[3] This is expected to more effectively catalyze the ORR, which is limited by activation of the O_2 molecule on Ag.[4] We have experimentally demonstrated the synthesis of an Ag-Co surface alloy that exhibits enhanced electro-catalytic activity, rivaling that of Pt at fuel cell operating conditions. Although Ag and Co are immiscible in the bulk phase,[5] the enhanced Ag-Co structures were generated by decomposition of an ordered bimetallic $Ag_3Co(CN)_6$ nanoparticles, which were rapidly reduced and quenched such that residual Co became trapped in the near-surface region of the Ag lattice. The structure of the material was confirmed by high-resolution electron energy loss spectroscopy and by cyclic voltammetry, which

showed that a small amount of Co was retained (as was the high activity) after a rigorous leaching treatment.

The present study attempts to extend the synthetic technique developed for Ag-Co to generate Ag-Fe and Ag-Ni alloys or surface alloys for use as ORR catalysts. We have utilized the analogous water-soluble compounds $K_3Co(CN)_6$, $K_4Fe(CN)_6$, and $K_2Ni(CN)_4$, which all undergo precipitation in the presence of Ag, to form $Ag_xM(CN)_y$ nanoparticles as catalyst precursors. These were then subjected to an identical rapid heating and quenching reduction protocol to generate the bimetallic catalysts. The materials were characterized with x-ray diffraction (XRD) at each stage of the process as well as cyclic voltammetry (CV) to assess their surface reactivity. Oxygen reduction activity measurements performed with the rotating disk electrode (RDE) method confirm the high activity of Ag-Co, but Ag-Ni and Ag-Fe exhibit similar activity to monometallic Ag. This is attributed to a failure to produce any degree of surface alloying. The failure with Ag-Ni may be related to the low Ag/Ni stoichiometry in the chosen precursor, while for Ag-Fe the issues are likely related more to low stability of the precursor and possible voltage-induced segregation during testing.

7.2 Experimental

7.2.1 Catalyst Synthesis

Carbon-supported Ag-M nanoparticles were synthesized by a multi-stage incipient wetness impregnation procedure. In a typical synthesis, quantities of $AgNO_3$ and $K_x[M(CN)_y]$ (i.e. $K_3Co(CN)_6$, $K_4Fe(CN)_6$, or $K_2Ni(CN)_4$, all Sigma Aldrich)

were chosen such that Ag was in a 10% stoichiometric excess to the M precursor and the total metals loading would be 20% on carbon (400mg Vulcan XC72 (Cabot) was the typical scale). The $AgNO_3$ and $K_x[M(CN)_y]$ were dissolved in separate 2mL solutions of deionized water. The solutions were then added dropwise, alternating 1mL of each precursor at a time, to 400mg of carbon (pretreated 2h in H_2 at 400°C), with drying at 60°C between each mL of water added, for a total of 4 impregnation/drying cycles. This forms $Ag_x[M(CN)_y]$ particles with excess $AgNO_3$ and KNO_3 that were removed by triply rinsing and centrifuging the powder with deionized water, followed by drying again. Pure Ag/C reference catalyst was prepared by single-step incipient wetness impregnation using $AgNO_3$. To decompose the precursors, the powders were inserted into a preheated tube furnace at 500°C under 4%H_2/Ar and held for 10 minutes. Samples were found to reach the furnace temperature in 1-2 minutes. The tube was then removed and quenched with flowing air on the exterior.

7.2.2 Characterization

Electrochemical measurements were performed at room temperature in an all-Teflon three-electrode cell (made in house) with a Gamry Instruments Reference 3000 potentiostat/galvanostat/FRA. The reference (Hg/HgO in 1M KOH, Radiometer Analytical) and counter electrodes (Pt wire, Alfa Aesar) were both in isolated compartments with long diffusion paths to the working electrode chamber. Electrolyte solutions of 0.1M NaOH were prepared from ultrapure water (18MΩ, Millipore) and 99.99% sodium hydroxide (Sigma Aldrich). An uncompensated resistance

was measured via the high frequency impedance (generally ~40Ω), and was corrected for in the polarization curves. All potentials are reported relative to the Reversible Hydrogen Electrode ($V_{RHE} = V_{NHE} + 0.0591pH$), for which the potential was calibrated by voltammetry to find the potential of zero current in H_2 saturated electrolyte. Cyclic voltammograms were taken in argon-purged solution, and rotating disk polarization curves were taken in O_2-saturated solution.

Working electrodes were prepared by sonicating the catalyst powders in 99.9% acetone (Fisher) at 0.75mg/mL for >1h and dispersing two 12 μL droplets onto a 5mm glassy carbon electrode insert (Pine Instruments), which had been polished with 0.05μm alumina paste and sonicated in ultrapure water prior to use. These electrodes were put into a Teflon RDE housing, attached to a rotator (Pine) and inserted into the cell under potential control at $0.05V_{RHE}$ using a Pt wire dummy electrode, temporarily connected to the working electrode lead. To determine kinetic current densities from ORR polarization curves, the Koutecky-Levich (KL) equation was used: $1/|i| = 1/|i_k| + 1/|i_L|$,[6] where, i_k is the kinetic current and i_L is the mass transfer limited current at very large overpotential. Surface areas were measured with Pb-stripping voltammetry, which was performed immediately after polarization curve measurements. For stripping voltammetry, the solution was purged with argon while holding the sample at $0.4V_{RHE}$ and adding $Pb(NO_3)_2$ stock solution for a final concentration of 125μM Pb^{++}. The potential was then moved to $0.22V_{RHE}$ for 1 min., causing Pb underpotential deposition, and the swept to $0.6V_{RHE}$ at 20mV/s. The procedure was perfomed repeatedly and the stable voltammograms

were integrated assuming 280μC/cm^2, which was established based on prior single-crystal measurements of the low-index Ag facets.[7,8]

XRD measurements were conducted in a Rigaku rotating anode diffractometer with a monochromated CuKα x-ray source at a scan rate of 1°/min. Pure $K_x[M(CN)_y]$ precursors were diluted 1:1 by mass with carbon before scanning.

7.3 Results and Discussion

In Figure 7-1 we show XRD patterns taken for each step in the synthetic route to the Ag-M bimetallic particles. The intermediate precipitates formed from $AgNO_3$ and the cyanometallates show no peaks from the original potassium cyanometallates, and no peaks corresponding to KNO_3 are present, indicating that rinsing after precipitation is adequate to remove the soluble leftover components. For the Ag-Ni species, we have not located a standard diffraction pattern for comparison and thus label the precipitate as $Ag_xK_y[Ni(CN)_4]$ because we cannot confirm the full displacement chemistry. $Ag_3[Co(CN)_6]$ x-ray diffraction is well characterized (it exhibits unique negative thermal expansion properties)[9] and we confirm this product is formed in a relatively pure state, with a small amount of fcc-Ag impurity, likely formed during the drying steps of the synthesis prior to rinsing. Finally, in contrast to the other two materials, the precipitate from $AgNO_3$ and $K_4[Fe(CN)_6]$ shows relatively poor diffraction. We can confirm that the material is not rinsed away as it can still be reduced to give a crystalline product and the product exhibits ORR activity (discussed in the next section). Thus it is either (i)

amorphous or (ii) formed with extremely small crystallite domains. Further analysis of this material, including imaging and elemental analysis, would be necessary to increase confidence in these conclusions.

The bottom row of XRD patterns in Figure 7-1 shows the bimetallic products after reducing at 500°C for 10 min in 4% H_2. All products show patterns dominated by fcc-Ag, which we also found to be the case for the Ag-Co surface alloy in our prior work. Pure 3d-metal particles in the bimetallic samples were generally found in that work to exhibit very weak reflections due to small particle sizes and are thus not seen in the product spectra.[3]

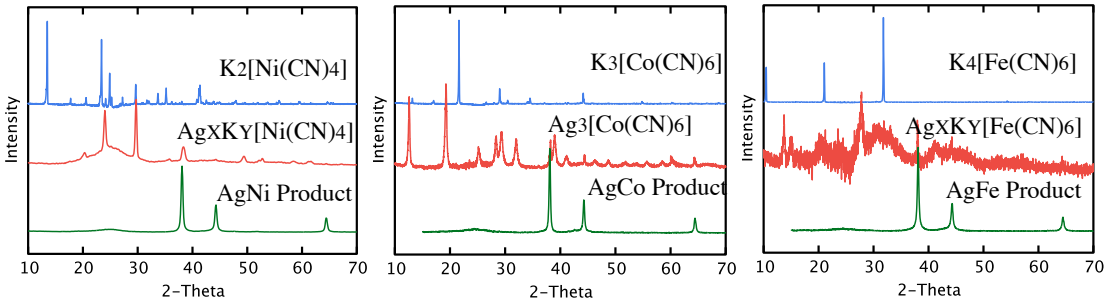

Figure 7-1: X-ray diffraction patterns for each stage in Ag-M bimetallic nanoparticle synthesis. $K_x[M(CN)_y]$ commercial precursors were precipitated with $AgNO_3$ on carbon support to make $Ag_x[M(CN)_y]$ intermediate precipitates, followed by rapid reduction at 500°C to form the metallic particles.

Figure 7-2 shows rotating disk electrode ORR polarization curves and corresponding Tafel plots taken in O_2 saturated 0.1M NaOH electrolyte for the catalyst powders prepared as described above. We see that the Ag-Ni and Ag-Fe materials have ORR activities that are fairly similar to pure Ag, while the Ag-Co material gives substantially higher reduction currents—over a factor of 5 at $0.8V_{RHE}$.

We attribute the lack of enhancement in the Ag-Ni and Ag-Fe bimetallics to essentially complete segregation of the materials, which is consistent with cyclic voltammetry, shown in Figure 7-3. We suspect that a failure to create a surface alloy with Ag-Ni may be related to the low Ag/Ni stoichiometry in the chosen precursor making it difficult to trap Ni in the Ag lattice during reduction. For Ag-Fe the issue is more likely related to low stability of the precursor and possible voltage-induced segregation during testing.

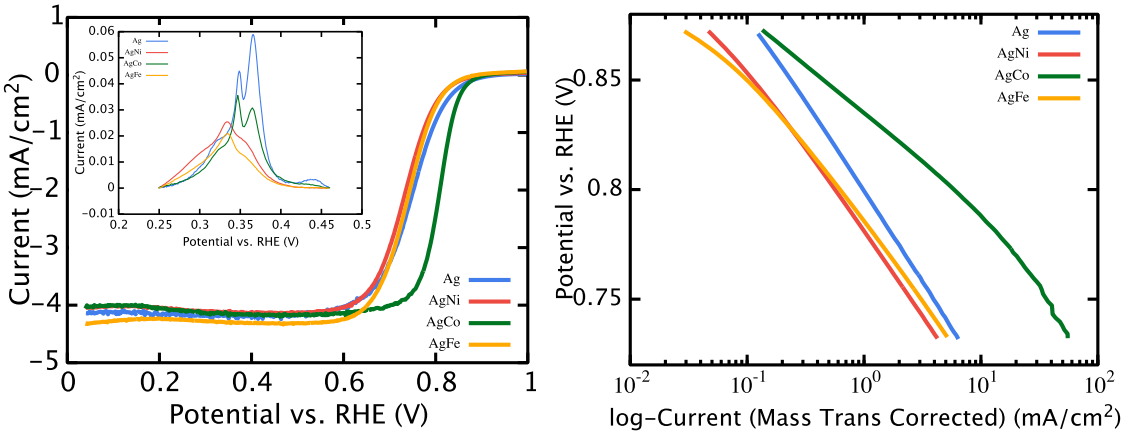

Figure 7-2: Rotating disk ORR polarization curves and Tafel plots for Ag-M materials. All data recorded in O_2 saturated 0.1M NaOH at 10mV/s and 900rpm. Inset shows Pb-stripping voltammetry used for surface area measurement.

In Figure 7-3 we show cyclic voltammograms for Ag and each bimetallic material. We show the evolution of the initial cycles (1st, 2nd, 5th, and 10th) in order to illustrate a number of transient features, which are due largely to irreversible oxidation of the 3d metals. Due to a high degree of segregation in all cases, much of

the electrochemical behavior appears as a superposition of the behavior of pure Ag and the pure additional metal present.

We have discussed the voltammetry of Ag-Co in detail in the previous chapter, but briefly we note that the low potential feature around $0.3V_{RHE}$ corresponds to transition of exposed metallic Co to $Co(OH)_2$,[10,11] while the features at 0.6 V and 0.8V are unique to the bimetallic material (not seen on Ag or a pure Co control sample). We have hypothesized that this is related to the stronger oxygen affinity of the surface and may correlate to its enhanced activity. The Ag-Fe material shows two features that are attributable to pure Fe redox processes. At roughly $0.0V_{RHE}$ we see a small decaying feature related to transformation between metallic Fe and $Fe(OH)_2$, while at 0.3V we see a growing feature that may the $Fe(OH)_2/Fe_2O_3$ redox pair or direct Fe/Fe_2O_3 oxidation.[10,11] The growth of this feature may simply be due to roughening of Fe particles, or may also be related to segregation of Fe that is initially beneath the Ag surface, whether as domains of pure Fe or Fe incorporated into the Ag lattice. This may be an indication that Ag-Fe surface alloys will not be stable for extended use in ORR. For Ag-Ni, the voltammogram does not show very marked redox features. The slight peak around $0.3V_{RHE}$ should correspond to $Ni/Ni(OH)_2$ oxidation,[10,11] but the feature is much smaller than would be expected by analogy to the other samples. It may be the case that the sample is simply pre-oxidized by contact with the atmosphere and it does not re-reduce substantially at the negative potential limit of the scan. The higher potential peak may be formation of some Ni_3O_4. For completeness, we also point out that the sharp cathodic currents on the Ag-Co and Ag-Ni CV's are due to hydrogen evolution on the transition metals.

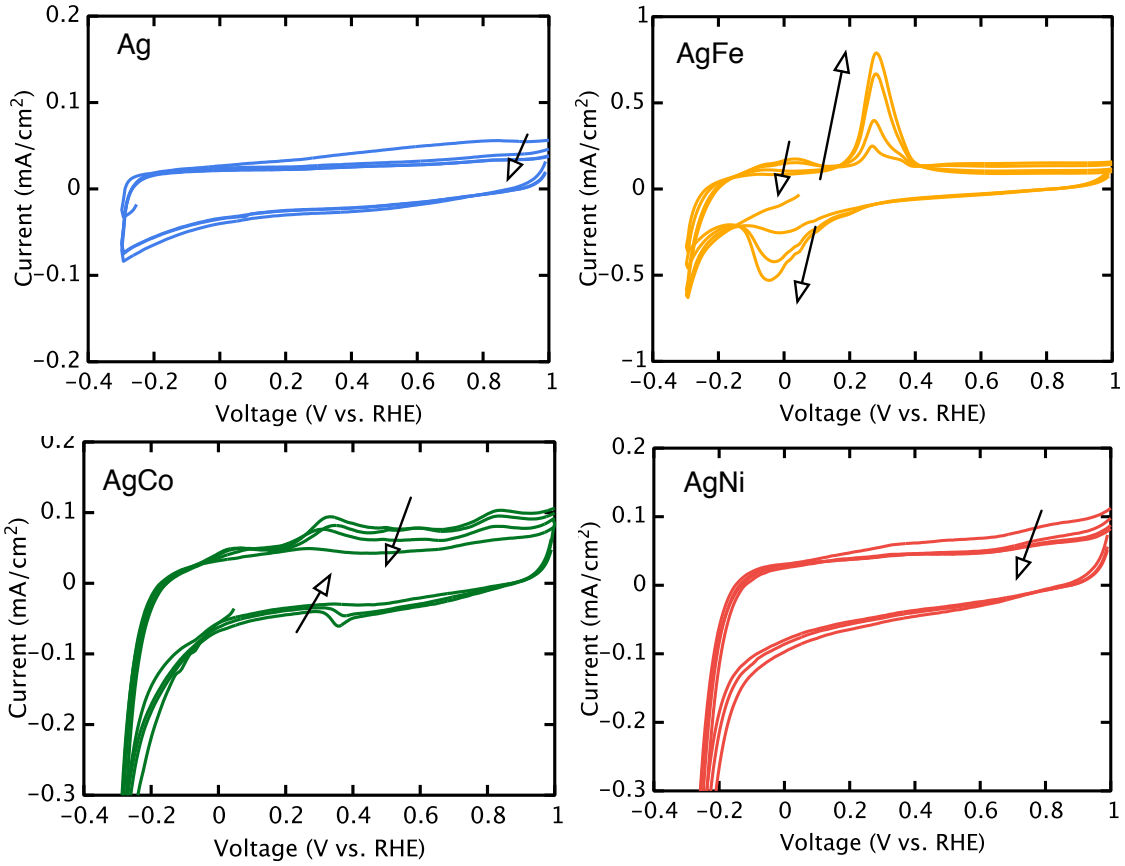

Figure 7-3: Cyclic voltammetry evolution of Ag-M materials. CV's are recorded in Ar-purged 0.1M NaOH at 50mV/s. We show the 1st, 2nd, 5th, and 10th scans, and arrows are provided to show the direction the peaks evolve (decaying or growing) with time.

7.4 Conclusions

We have explored the possibility of using rapid reduction of bimetallic precursors as a means to create surface alloys of the immiscible metal pairs, Ag-Ni, Ag-Co, and Ag-Fe for use as ORR electro-catalysts. Bimetallic salt nanoparticles were generated on carbon support using precipitation reactions of Ag^{+} and appropriate metallocyanate ions. Rapidly-reduced Ag-Co showed significantly enhanced

electrochemical oxygen reduction activity compared to pure Ag, while the Ag-Ni and Ag-Fe showed activity similar to pure Ag, indicating the metals are largely segregated. We hypothesize that the $Ag_2Ni(CN)_4$ precursor is too rich in Ni (only 2:1 Ag:Ni ratio) to provide a matrix of Ag that can trap Ni during decomposition. The Ag-Fe precursor, which should initially be $Ag_4Fe(CN)_6$, may not be stable toward pre-reduction treatments such as drying at elevated temperature, and/or may exhibit voltage-induced segregation of any incorporated Fe upon introduction to the electrochemical environment. While the chosen approach did not generate improved catalytic properties for Ag-Ni and Ag-Fe bimetallics, we emphasize that a number of further characterization studies must be done to determine the nature of the bimetallic precursors, and that other potential starting materials or changes in treatments, such as vacuum drying or changing the time and temperature of reduction, may substantially change the outcome.

7.5 References

1. The US Department of Energy (DOE). Energy Efficiency and Renewable Energy. at <http://www1.eere.energy.gov/hydrogenandfuelcells/mypp/>

2. Gasteiger, H. A., Kocha, S. S., Sompalli, B. & Wagner, F. T. Activity benchmarks and requirements for Pt, Pt-alloy, and non-Pt oxygen reduction catalysts for PEMFCs. *Applied Catalysis B: Environmental* **56,** 9–35 (2005).

3. Holewinski, A. & Linic, S. High Performance Ag-Co alloy Catalysts for Electrochemical Oxygen Reduction. *Submitted Manuscript*

4. Holewinski, A. & Linic, S. Comparative Kinetic Analysis of Electrochemical Oxygen Reduction on Silver and Platinum Electrodes. *Manuscript in Preparation*

5. Karakaya, I. and Thompson, W. T. The Ag-Co (Silver-Cobalt) System. *Bulletin of Alloy Phase Diagrams* **7,** 259–263 (1986).

6. Bard, A. J. & Faulkner, L. R. *Electrochemical Methods: Fundamentals and Applications*. (John Wiley & Sons, Inc., 2001).

7. Kirowa-Eisner, E., Bonfil, Y., Tzur, D. & Gileadi, E. Thermodynamics and kinetics of upd of lead on polycrystalline silver and gold. *J. Electroanalytical Chem.* **552,** 171–183 (2003).

8. Herrero, E., Buller, L. J. & Abruna, H. D. Underpotential deposition at single crystal surfaces of Au, Pt, Ag and other materials. *Chemical Reviews* **101,** (2001).

9. Goodwin, A. L. *et al.* Colossal positive and negative thermal expansion in the framework material Ag3[Co(CN)6]. *Science* **319,** 794–7 (2008).

10. Bratsch, S. Standard electrode potentials and temperature coefficients in water at 298.15K. *J. Phys. Chem. Ref. Data* **18,** 1–21 (1989).

11. Pourbaix, M. *Atlas of Electrochemical Equilibria in Aqueous Solutions*. (National Association of Corrosion Engineers, 1974).

Chapter 8: Conclusions and Future Outlook

This dissertation has shown the application of theoretical techniques to garner insights about reaction mechanisms and used these insights to design improved catalytic materials. Specifically we have explored the mechanism of electrochemical oxygen reduction on the surfaces of Pt (a near-optimal catalyst) and Ag electrodes through microkinetic modeling and density functional theory calculations, and we have identified cost-effective Ag-based alloy materials with near-optimal oxygen binding characteristics for effective catalysis of the reaction. We have designed a synthetic technique that is capable of producing one of the alloy compositions of interest, and we have demonstrated its superior catalytic performance. Other compositions were explored but did not show the same enhancements, and we leave improved syntheses of these materials as an area for continued work. In this chapter we summarize the main conclusions of each component of this work and then discuss remaining open questions and future research directions.

8.1 General Conclusions

The overarching goal of this dissertation has been to apply insights from a fundamental understanding of molecular-level interactions and heterogeneous reaction kinetics to interpret macroscopic reactivity trends in electrochemical systems and to design optimal electro-catalysts. The electrochemical oxygen reduction reaction (ORR) was chosen as a focal point due to its great potential impacts in energy production. We have herein demonstrated that the experimentally observed kinetic behavior of the ORR is readily interpretable in terms of elementary steps and is a distinguishing fingerprint of the elementary mechanism. This mechanistic understanding provided clear design criteria for improved catalytic materials and was discussed for current-standard Pt-based catalyst materials, as well as Ag, which is a potential basis for economical next-generation ORR catalysts. We then discussed the experimental development of Ag-based bimetallic materials with 3d-transition metals and demonstrated their synthesis and performance, which was found to be vastly improved for Ag-Co. The major conclusions from each component of this dissertation are:

- Using microkinetic modeling we showed that deviations from ideal Tafel kinetics are inherent to the ORR and any multi-step heterogeneous electro-catalytic reaction. We showed that the deviations can be attributed to a simultaneous increase in the rate of the rate-limiting elementary step and a change in the number of available active sites on the electrode as overpotential is induced. Our analysis showed that for the ORR on Pt electrodes the concentration of OH and H_2O surface intermediates primarily

cause the non-ideal kinetics. Based on comparison between model and experiment, as well as DFT calculations, we dispelled alternative interpretations of Tafel behavior such as changes in rate-limiting step or adsorbate repulsion effects

- We further provided a comparative study of the ORR kinetic parameters on both Ag and Pt electrodes alkaline environment, using cyclic voltammetry (CV) and rotating disk electrode (RDE) kinetic measurements to compare the rates on each material and how these rates vary as a function of potential and adsorbate coverage. The apparent transfer coefficient and reaction orders with respect to hydroxyl ion and oxygen partial pressure were found to be consistent with the first electron transfer to molecular oxygen as the rate limiting step. In contrast to Pt, where changes in the rate parameters correlate well to adsorbate coverage on the surface, a very weak relation was found between adsorbate coverage and changes in the kinetics on Ag. This points to a strong role of under-coordinated sites, which can become poisoned at low potentials. Thus for Ag, we proposed moving in the direction of stronger binding should lead to higher ORR activity by increasing TOF's on the more predominant surface facets,
- We next illustrated the design of relatively inexpensive Ag-Co surface alloy nanoparticle electro-catalysts for oxygen reduction, with equivalent area-specific activity to commercial Pt-nanoparticles at realistic fuel cell operating conditions. The Ag-Co materials were identified with quantum chemical calculations and synthesized with a novel technique that generates

a surface alloy, despite the bulk immiscibility of the constituent materials. Characterization studies showed that the origin of the activity improvement comes from a ligand effect, in which Co perturbs the Ag surface sites and improves their inherent activity.

- Finally, we explored the use of rapid reduction of bimetallic $Ag_x[M(CN)_y]$ precursors (M=Fe, Ni, Co) as a possible means to induce alloying between Ag and 3d metals and enhance the ORR activity relative to pure Ag. The materials were characterized with x-ray diffraction at each stage of synthesis as well as cyclic voltammetry to assess their surface reactivity. Oxygen reduction activity measurements showed significantly improved activity for Ag-Co. However, Ag-Ni and Ag-Fe exhibited similar activity to monometallic Ag, and this was attributed to a failure to produce alloying, which we related to low Ag/Ni precursor stoichiometry in the former case, and instability for either the precursor or the final product in the latter.

8.2 Outlook on Future Research

Taken as a whole, this work provides a clear platform for analysis of electrochemical reaction mechanisms and the design of improved (electro)catalytic materials. We believe we have opened a new door for the development of cost effective and highly active ORR catalysts for use in fuel cells. However, a great number of outstanding questions and obvious extensions to this work exist.

In Chapters 4 and 5 we discuss simplified microkinetic models of the ORR rate on common electrode materials. While we are able to obtain reasonable qualitative agreements between experiment and theory by treating electrodes as single crystal facets or making a mean field approximation, it is obvious that real catalytic particles possess a great heterogeneity of active sites with varying reactivity. Greater accuracy and confirmation of speculated hypotheses such as the role of under-coordinated sites could be obtained by (i) quantitatively treating the differences in adsorbate binding energies across different types of sites with DFT calculations and (ii) applying techniques such as Monte Carlo simulations to simulate large ensembles of sites and reacting molecules as well as to better describe the aqueous background. Coupled with controlled synthesis of well-defined catalyst morphologies, much more certainty could be obtained regarding the reaction mechanisms. A few studies have already laid some groundwork for such modeling.[1,2] We believe theory is most valuable in two limits: either very simple approximations that can be mentally evaluated and generate intuitive solutions (e.g. our present model) and fully comprehensive models that capture all known effects and reproduce real system behavior as accurately as possible.

In Chapter 6 and 7 we discussed the design of Ag-based bimetallic materials for use as ORR catalysts. We believe that the foremost challenge in moving forward with this work is the inherent thermodynamic immiscibility of the identified alloy compositions and difficulty in synthesizing structures with more than just surface-mixing. Further optimization of synthesis conditions or precursor choice may result in better degrees of alloying (particularly if more rapid heating can be achieved, for

example through induction), and may ultimately result in generating surface alloys of the Ag-Ni and Ag-Fe structures targeted. However, we gather from the low degree of alloying achieved even for the Ag-Co compounds, that the general approach to synthesis may not be ideal—particularly because a fuel cell catalyst must work for very extended periods and on a long enough time scale the surface region will invariably segregate. Totally new approaches, likely based on colloidal chemistry, will be needed to generate bulk alloys of the desired compositions, which should remain alloyed for longer time scales. A few contributions have recently successfully formed ordered alloys of Au with the 3d elements,[3] which are also not thermodynamically favorable. While these procedures are not directly transferrable to Ag due to different native redox states of Au and Ag, the fact that the Au-3d alloys can be formed is a promising finding. It also possible that the proposed Ag alloys will never become a surrogate for Pt, and that the next technological breakthrough in ORR catalysts will come from a completely different class of materials (e.g. oxides, sulfides, nitrides, or organic compounds) or that fuel cells will become obsolete in the face of ground breaking solar conversion and battery technologies. Until that day we will continue working.

8.3 References

1. Greeley, J., Rossmeisl, J., Hellmann, A. & Norskov, J. K. Theoretical Trends in Particle Size Effects for the Oxygen Reduction Reaction. *Z. Phys. Chem.* **221,** 1209–1220 (2007).

2. Rai, V., Aryanpour, M. & Pitsch, H. First-Principles Analysis of Oxygen-Containing Adsorbates Formed from the Electrochemical Discharge of Water on Pt(111). *J. Phys. Chem. C* **112,** 9760–9768 (2008).

3. Vasquez, Y., Luo, Z. & Schaak, R. E. Low-temperature solution synthesis of the non-equilibrium ordered intermetallic compounds Au3Fe, Au3Co, and Au3Ni as nanocrystals. *J. Am. Chem. Soc.* **130,** 11866–7 (2008).

4. Tao, F. *et al.* Reaction-Driven Restructuring of Rh-Pd and Pt-Pd Core-Shell Nanoparticles. *Science* **322,** 932–934 (2008).

5. Greeley, J. & Norskov, J. K. Combinatorial Density Functional Theory-Based Screening of Surface Alloys for the Oxygen Reduction Reaction. *J. Phys. Chem. C* **113,** 4932–4939 (2009).